uOttawa

L'Université canadienne
Canada's university

FACULTÉ DES ÉTUDES SUPÉRIEURES ET POSTOCTORALES

uOttawa

L'Université canadienne
Canada's university

FACULTY OF GRADUATE AND POSDOCTORAL STUDIES

George Choueiri

AUTEUR DE LA THÈSE / AUTHOR OF THESIS

M.A.Sc. (Mechanical Engineering)

GRADE / DEGREE

Faculty of Engineering, Mechanical Engineering

FACULTÉ, ÉCOLE, DÉPARTEMENT / FACULTY, SCHOOL, DEPARTMENT

An Experimental Study of Natural Convection in Vertical Open-Ended Concentric and Eccentric Annuli

TITRE DE LA THÈSE / TITLE OF THESIS

S. Tavoularis

DIRECTEUR (DIRECTRICE) DE LA THÈSE / THESIS SUPERVISOR

CO-DIRECTEUR (CO-DIRECTRICE) DE LA THÈSE / THESIS CO-SUPERVISOR

EXAMINATEURS (EXAMINATRICES) DE LA THÈSE / THESIS EXAMINERS

D. Feszty

M. Radulescu

Gary W. Slater

Le Doyen de la Faculté des études supérieures et postdoctorales / Dean of the Faculty of Graduate and Postdoctoral Studies

An Experimental Study of Natural Convection in Vertical Open-Ended Concentric and Eccentric Annuli

George H. Choueiri

Thesis submitted to the Faculty of Graduate and Postdoctoral Studies
in partial fulfillment of the requirements for the degree of

MASTER OF APPLIED SCIENCE

in Mechanical Engineering

Ottawa-Carleton Institute for Mechanical and Aerospace Engineering
University of Ottawa
Ottawa, Canada

June 2009

Your file Votre référence
ISBN: 978-0-494-61344-3
Our file Notre référence
ISBN: 978-0-494-61344-3

Abstract

The effects of eccentricity on the natural convection heat transfer from a vertical open-ended cylindrical annulus with diameter ratio of 1.63 and aspect ratio of 18:1 have been investigated experimentally. Measurements of transient and steady state wall temperature distributions for different eccentricities were collected to help understand the heat transfer processes and also to serve as benchmarks for the validation of future CFD studies. Particle image velocimetry was used to validate the calculated mass flow rate in the annulus. It was found that, whereas at very low eccentricities there was insensitivity to eccentricity on the overall heat transfer, a diminishing of the heat transfer occurred for higher eccentricities. Plots of the local azimuthal variation of the Nusselt number showed that at low eccentricities heat transfer improved on one side of the annulus but decreased on the other side. The Nusselt number was found to decrease with eccentricity, while the Rayleigh and Grashof numbers had an increasing trend. It was also found that the mass flow rate did not appear to be strongly influenced by varying eccentricity within the experimental range. The Reynolds number was calculated and the flow within the annulus was found to be transitional nearing laminar with increased distance from the inlet.

Acknowledgements

I have been blessed with the guidance, support, hard work and dedication of my supervisor, Dr. Stavros Tavoularis, who I would like to acknowledge and thank immensely. The gratitude I wish to convey cannot be written on paper or phrased in words but the essence of which will live in me eternally. I would like to thank Leo Denner without whom many aspects of this work would not have been possible. I'd like to acknowledge the help of John Perrins, James MacDermid, Stanley Weedmark and Michael Burns at the machine shop for their help. As well, I would like to thank my fellow colleagues who have made this a memorable experience. In particular, I would like to thank my colleague Christina Vanderwel who has always been happy to lend a hand or share her knowledge. I am also very grateful to my family for their encouragement and support. Finally I'd like to give a special thank you to my wife Anne-Lise for her invaluable help and patience and for continuing to smile even in the most difficult days.

Table of Contents

List of Figures

List of Tables

Nomenclature

A	area, m^2
c	specific heat, J/kg·K
E	electric potential, V
e	eccentricity
F	force, N; view factor
g	gravitational acceleration, m/s^2
Gr	Grashof number
Gr*	modified Grashof number
h	distance, m; convection heat transfer coefficient, $W/m^2 \cdot K$
H	height, m
I	current, A
k	thermal conductivity, W/m·K
l	length, m
m	mass, kg
$\dot{m}$	mass flow rate, kg/s
Nu	Nusselt number
p	pressure, N/m^2
P_R	percentage of deviation, %
Pr	Prandtl number
Q	total heat power, W

q	heat transfer rate, W; power, W
q''	heat flux, W/m^2
R	electric resistance, Ω
r	radius, m
Ra	Rayleigh number
Ra*	modified Rayleigh number
Re	Reynolds number
T	temperature, K
T^*	temperature non-dimensionalized by inlet and mid-height temperatures
$T^{\dagger}$	temperature non-dimensionalized by minimum and maximum temperatures
$T^{\dagger\dagger}$	temperature less minimum temperature
$T^{\ddagger}$	temperature less reference temperature
t	thickness, m; time, s
U	uncertainty
V	velocity, m/s
~~V~~	volume, m^3
w	width, m
x, y, z	rectangular coordinates, m
z^*	dimensionless height
$z^{\dagger}$	aspect ratio

Greek Letters

α	thermal diffusivity, m^2/s; temperature coefficient of resistance, K^{-1}
β	volumetric thermal expansion coefficient, K^{-1}
ε	emissivity

θ	zenith angle, °
λ	wavelength, μm
μ	viscosity, kg/s·m
v	kinematic viscosity, m^2/s
ρ	density, kg/m^3; electrical resistivity, Ω·m
σ	Stefan-Boltzmann constant, standard deviation
Φ_e	emitted radiation, W
0	reference, initial

Subscripts

a	annulus
B	buoyancy
cv	control volume
D	diameter
F	fluid
g	gravitational
h	hydraulic diameter
i	inner cylinder
in	inlet
L	linear
m	mean fluid property
max	maximum
mid	property at mid height of annulus
min	minimum
net	total

O	object
o	outer cylinder
p	constant pressure
r	radial
s	surface
w	wall
θ	azimuthal
λ	spectral
∞	free stream condition

Superscripts

*	dimensionless quantity

Overbar

$\bar{}$	average

Chapter 1 Introduction

1.1 Natural convection

When the surface temperature of a body immersed in a fluid is different from that of the surrounding fluid, the fluid "particles" in contact with the surface assume its temperature (Martynenko and Khramtsov, 2005). This occurs through the transfer of energy from more energetic particles (particles at higher temperature) to less energetic ones (particles at lower temperature) through interactions at the atomic and molecular level (Incropera and DeWitt, 2005). This method of heat transfer is called conduction and it ideally takes place in solids and fluids in which there is a temperature gradient but no bulk fluid motion (Incropera and DeWitt, 2005). As will be discussed in more detail in section 4.1, temperature variation in fluids leads to a non-uniform field of mass forces (Martynenko and Khramtsov, 2005) primarily due to the effect of temperature on the density of the fluid. These forces, found within the fluid, generally lead to a bulk fluid motion which is driven entirely from within the fluid.

The heat transfer method described previously was observed by the American born Benjamin Thompson, Count Rumford of the Holy Roman Empire, in the 1790s while pondering over why persons often burnt their mouth while eating a piece of hot apple pie (Brush, 1973). In 1834, William Prout, as part of his writing of the eighth Bridgewater

Treatise[1], first used the term "convection", meaning "a carrying or conveying" (Prout, 1835), to describe this form of heat transfer giving the example of air transporting heat from the fire and up the chimney. It was not until the early 1900s that convection was significantly studied experimentally. One of the most notable and significant experimental works was carried out by Henri Bénard of France (Narasimhan, 1999). Later on, the English physicist John William Strutt, Baron Rayleigh, attempted to explain the theory behind the results from this experimental work.

In most literature, for example Bejan (2004) and Incropera and DeWitt (2005), the terms "natural convection" and "free convection" are used interchangeably to describe convection in which the driving mechanism comes from the fluid itself, as opposed to forced convection in which the driving mechanism is an external force. However, some texts make a distinction between the two terms; a set of definitions found to be most appealing was that free convection describes motion and heat exchange that occur in an infinite space, while natural convection takes place in a bounded volume (Martynenko and Khramtsov, 2005). For the purposes of this study, we will not consider any differences between these two terms, but will generally use them interchangeably.

Natural convection can be induced by not only gravitational forces due to density nonuniformity, but also by other forces such as centrifugal and electromagnetic forces

---

[1] Chemistry, Meteorology, and the Function of Digestion: Considered with Reference to Natural Theology, was the eighth Bridgewater Treatise which was commissioned by The Earl of Bridgewater to explore "The power, wisdom, and goodness of God, as manifested in the creation."

(Martynenko and Khramtsov, 2005). Convection is not limited to heat transfer, but can also refer to mass transfer in a fluid with non-uniform composition.

Heat transfer by natural convection plays a very important role in many engineering applications. Though not as effective a heat transfer mechanism as forced convection, natural convection is encountered widely in biological systems, in our environment and in technology. In this thesis, we will focus on natural convection heat transfer within an annulus formed between a vertical heated cylindrical core and a surrounding cylindrical cavity.

1.2 Natural convection in annuli

A heat exchanger is an essential part of many engineering applications and these applications range from HVAC (heating, ventilating, and air conditioning) systems to nuclear reactors. These heat exchangers come in many shapes and configurations, one of the simplest of which consists of hot and cold fluids flowing through concentric tubes, otherwise known as a double-pipe construction (Incropera and DeWitt, 2005). The fluids could be flowing in the same or opposite directions, which are known as parallel flow or counter flow, respectively. In industrial heat exchangers, forced convection is the usual form of heat transfer, nevertheless, in some applications, such as solar water heating systems, natural convection is employed to eliminate the need of pumps (Davidson and Liu, 1999). Some advanced nuclear reactor concepts have also suggested the use of natural convection as the main driving force for coolant circulation in the reactors (Dimmick et al., 2002). This not

only removes the need for the pumps to drive the flow, which cuts down on costs, but also serves as an emergency cooling system in the event of power failure.

Most common designs of the simple double-pipe heat exchangers consist of a concentric annular duct, in which eccentricity may be introduced by manufacturing tolerances, imperfections in construction or thermal stresses. In such cases, one would like to be able to estimate the effect of eccentricity on the overall heat transfer. In studies by Guellouz and Tavoularis (2000a,b), Gosset and Tavoularis (2006) and Chang and Tavoularis (2006), for forced convection in an axial channel containing a cylinder, flow pulsations enhancing transport across narrow gaps were observed. These pulsations were strengthened by increasing eccentricity. It is not yet known whether such pulsations would exist in natural convection through an eccentric open-ended annulus and whether heat transfer might be maximized globally or locally for an optimal eccentricity.

1.3 Motivation and objectives

The heat transfer literature contains many studies of the effect of eccentricity on the natural convection heat transfer in concentric and eccentric annuli. A lot of this work focused on natural convection in concentric and eccentric horizontal annuli and the majority of these studies were done numerically, although a few were experimental. However, only little experimental work has been found in the literature concerning the problem of natural convection in a vertical open-ended eccentric annulus. To address this problem, we decided to investigate experimentally the effect of eccentricity on the heat transfer in a specific annular geometry. Besides helping us understand an important system of natural convection,

the results of our work could serve as a benchmark for validation of future CFD studies of natural convection in similar geometries.

The primary objective of this thesis is to study the sensitivity of natural convection heat transfer to eccentricity in an open-ended vertical annulus formed between a cylindrical core and a surrounding cylindrical cavity. We will be using an apparatus with fixed dimensions for the cylindrical core and surrounding cylindrical cavity and change the geometry of the annulus by moving the cylindrical core, hence changing the eccentricity. Additionally, we will use different wall heat fluxes for a series of eccentricities and try to isolate the effect of eccentricity on the overall heat transfer. We will also be investigating whether or not there is any local improvement or decrement in the heat transfer due to some flow phenomena which may occur across the narrow gap between the core and the cavity, as in the case of forced convection.

1.4 Thesis organization

This thesis is organized into nine chapters. The second chapter provides a literature review of previous research related to our study. This chapter starts with natural convection from simple geometries and continues to discuss studies done on natural convection in more complicated geometries similar to our own. The third chapter describes the apparatus used for the experiments, as well as the instrumentation used and the software which monitor and control some of these instruments. Analytical background is discussed in the fourth chapter with a focus on buoyancy driven flows, especially natural convection. This chapter also has a section on electrical resistance and heat flux, which gives the basic equations needed to

perform many of the calculations in later chapters. Measurement procedures are discussed is the fifth chapter; here we describe the experiments we have performed for this study and how we obtained our results. In the sixth chapter, we examine the measurement uncertainty in our results and analyze their significance. The experimental results are presented in the seventh chapter, whereas, in the eighth chapter, we examine in depth the heat transfer problem we are studying and discuss the different forms of heat transfer which take place in this experiment. We also analyze our results and quantify the dimensionless heat transfer parameters based on them. In the last chapter, we summarize the conclusions of this study and provide some recommendations for future research.

Chapter 2 Literature Review

2.1 Introduction

Our experimental geometry consists of two vertical cylindrical surfaces, one surrounded by the other, such as to form an annulus. In order to understand the natural convection heat transfer in our system, we looked at many previous experimental and numerical studies in geometries similar to ours. Perhaps the simplest relevant case is free convection heat transfer from a vertical plate. In our case, however, the flow is bounded between two cylindrical surfaces. Therefore, it is even more relevant to consider studies of natural convection heat transfer between two vertical parallel plates, and to see how the distance between the plates affected the overall heat transfer.

As we are concerned with cylindrical surfaces, we also looked at studies of natural convection from the exteriors of vertical cylinders as well as the interiors of vertical tubes. We also found many experimental and numerical papers which discuss the natural and forced convection between concentric and eccentric, vertical and horizontal, open-ended and close-ended annuli. Though there is a lot of published work on many different geometries, only a selected few will de discussed in this review.

2.2 Free convection from vertical plates

Single vertical flat plate

Sparrow and Gregg (1956a) performed a numerical study on the laminar free convection heat transfer from a vertical plate with uniform surface heat flux. This study compared its results with those from the experimental work of Dotson (1954) and found good agreement. From this work we get an expression for the Nusselt number as a function of a modified Grashof number for a flat plate geometry with uniform heat flux. An important work by Churchill and Chu (1975) also considers the problem of a vertical flat plate and gives correlations for the Nusselt number as a function of the Rayleigh number.

Two vertical parallel plates

Natural convection heat transfer between two vertical flat plates was studied by Elenbaas (1942a), who expressed the Nusselt number through semi-empirical means as a function of the Rayleigh number, the plate spacing, and the plate length. Wirtz and Stutzman (1982) conducted experiments on free convection between two parallel vertical plates with constant wall heat flux and presented a relationship between the dimensionless wall temperature along the height and the dimensionless distance from the inlet of the two plates; this relationship includes an exponent which was experimentally derived and varies with the Rayleigh number. They also derived a relationship between the Rayleigh number and the Nusselt number. Bar-Cohen and Rohsenow (1984) also developed a relationship between the Nusselt number and the Rayleigh number for natural convection between parallel plates with symmetric heating, which takes into account the plate spacing and the plate length. This

paper also discusses an optimum spacing which would maximize the product of the heat transfer coefficient and the total surface area of the plates. The possible existence of an optimum eccentricity is something we plan to explore in our experiments.

2.3 Vertical cylinders and tubes

Vertical cylinders

The vertical cylinder is important for us as it resembles the cylindrical core of our annulus which we refer to as the inner cylinder throughout this study. Sparrow and Gregg (1956b) derived numerically relationships for the Nusselt number and compared them to similar relationships for a flat plate. They presented conditions under which the Nusselt number for a vertical cylinder could be approximated by expressions applying to a vertical flat plate. In an experimental study, Jarall and Campo (2005) presented an empirical relationship between the Nusselt number and a modified Rayleigh number for vertical cylinders.

Vertical tubes

Elenbaas (1942b) discusses free convection from the inner surface of vertical tubes of different shapes and cross-sections. This paper continues on previous work by the author concerned mainly with parallel plates and expands the scope of the study to variously shaped tubes including a circular one, which is our main interest. This paper also gives a general equation which relates the Nusselt number with the Grashoff and Prandtl numbers for several tubular cross-sections with errors of up to 10% for the various shapes. As with the

parallel plates for which an optimum spacing was found, an optimum hydraulic radius was derived for each cross-section, which gives the highest energy dissipation per unit of cross-section. Numerous numerical studies have been done on natural convection in vertical cylinders with uniform wall heat flux. We shall mention the work of Dyer (1975), who presented a relationship between the Nusselt number and the Rayleigh number in a manner that allows us to obtain the mean wall temperature from a known heat flux or vice versa.

2.4 Annuli

Forced convection in annular and similar geometries

In a numerical study, Cheng and Hwang (1968) produced solutions for laminar forced convection in eccentric cylindrical annuli under constant wall heat flux conditions. The Nusselt number was plotted for different eccentricity ratios and different heat source variables. Experiments performed by Gosset and Tavoularis (2006) in laminar flow in a rectangular channel containing a cylindrical core documented flow instability in the form of flow pulsations across the gap between the core and the adjacent wall. These pulsations occurred at a critical Reynolds number and became stronger as the gap width decreased.

Natural convection in horizontal annuli

Natural convection in horizontal concentric and eccentric annuli has been studied extensively over the years. Though this is a very different heat transfer problem from the one we are concerned with, due to the similarity in geometry we will briefly mention one paper which was found to be interesting on the subject. Kuehn and Goldstein (1978) studied

experimentally the effect of eccentricity on natural convection heat transfer through a fluid bounded by two horizontal isothermal cylinders. In this case, as in the case of many similar experiments, the annulus was closed at the ends. This study concluded that the overall heat transfer coefficient for an eccentric geometry with eccentricity less than 0.66 was within 10% of that for the concentric case for the same Rayleigh number. However, the local heat transfer coefficient was affected significantly, especially for higher eccentricities.

Natural convection in vertical annuli

Several experimental works have been conducted in natural convection in an enclosure between eccentric and concentric vertical cylinders, for example that of Sparrow and Charmchi (1983). Heat transfer coefficients for various geometries were obtained and the results of these experiments were compared with results obtained from numerical solutions; in many cases there was good agreement. Our work differs from the majority of these experiments in that we have an open ended annulus as opposed to an enclosure which significantly changes the heat transfer problem.

Al-Arabi et al. (1987) studied numerically the case of a vertical open-ended concentric annulus with one wall uniformly heated and the other adiabatic. This study was performed for different radius ratios and different parameters, including the velocity and temperature, were determined. The numerical work was found to be in good agreement with experimental studies.

Hosseini et al. (2005) performed experiments in an open-ended, insulated, vertical annulus with uniform wall heat flux from the outer pipe. They noted that they had found no previous experimental work in similar systems. This study concluded that the optimal

eccentricity for maximum heat transfer rate in this geometry was 0.5 and that the lowest heat transfer rate was for an eccentricity of 1.

In a preliminary study whose objectives were similar to the present ones, Bhandari (2006) explored the effects of eccentricity on natural convection heat transfer in a cylindrical annulus with only the inner cylinder being heated. The outer cylinder was constructed of a cast transparent acrylic material, while the inner cylinder was constructed of pieces of cylindrical aluminum sections fastened together and surrounding a tubular element heater. Two annular channels with diameter ratios of 0.4 and 0.6 were studied and different input electrical powers were experimented with. This study had some limitations which led us to reconsider the apparatus design. The presence of large radiation losses was one of these limitations, as it was difficult to estimate the radiation effects on the overall heat transfer. In our setup, we decided to minimize the radiation effects by heating both surfaces of the annulus such that they had comparable temperature distributions. Another limitation of Bhandari's work was the fact that the core cylinder was constructed of thick aluminum, which resulted in considerable axial and circumferential conduction, which interfered with the effects of eccentricity on convective heat transfer. In our setup, we used a poor thermal conductor for our core and covered it with a very thin stainless steel foil, so that conduction through it is minimal. Furthermore, in Bhandari's setup, temperature measurements in the preliminary study were done by inserting a probe into slots made in the outer cylinder and placing it in contact with the surface of the core. This introduced a wide range of undesirable effects, for example, air entrainment through the hole where the probe is placed. In our setup, we embedded a large number of thermocouples at different points of interest, and recorded the temperatures simultaneously without affecting the flow. Despite the limitations

of his setup, Bhandari (2006) was able to determine that natural convection heat transfer in eccentric vertical annuli was sensitive to eccentricity.

Chapter 3 Experimental Facility and Instrumentation

The main component of our setup is the test section seen in Figure 1, which consists of a cylindrical core supported at both ends by traversing assemblies and surrounded by a fixed cylindrical cavity such as to form an annulus with an adjustable eccentricity.

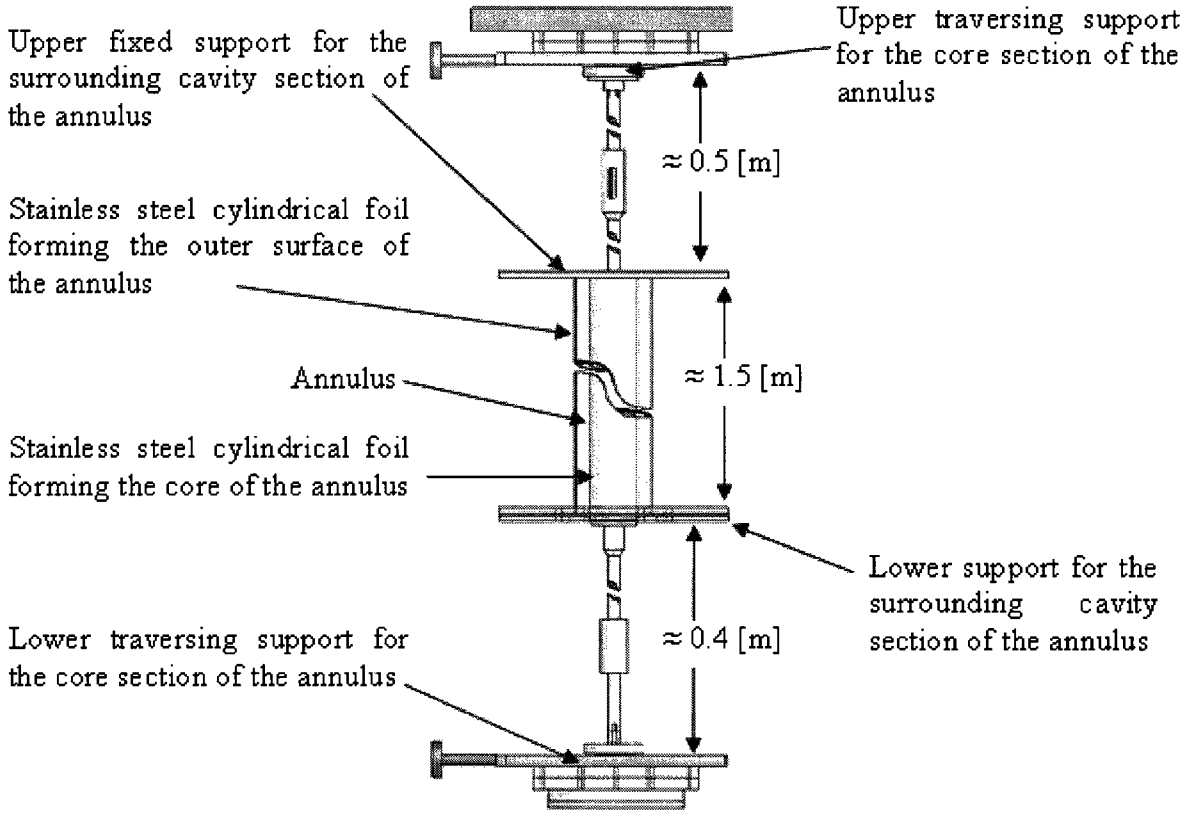

Figure 1 – Annulus test section with supports

Other components of our setup include a rigid metal frame to which the test section is mounted, a thermocouple data acquisition system and a power supply with additional data acquisition components. The setup also includes two desktop computers; one monitors and controls the power supply while the other monitors and records the temperature readings from the annulus. These components as well as other instruments used in our experiment will be discussed in detail in this chapter. A general overview of our experimental setup can be seen in Figure 2.

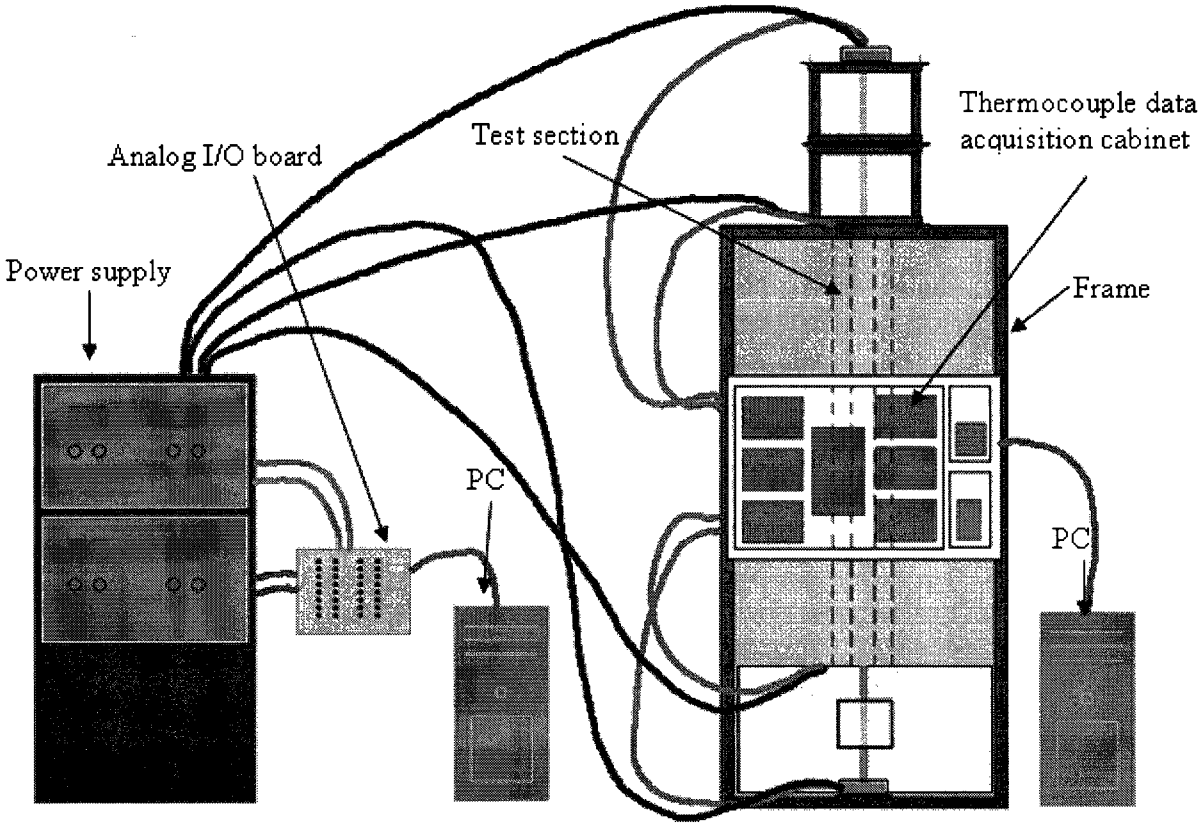

Figure 2 – General overview of experimental setup

3.1 Experimental apparatus

The test section is an annulus formed between a vertical cylindrical core and a surrounding vertical cylindrical cavity. The cylindrical core is wrapped with thin stainless steel foil which can be heated by passing a current through it. We will refer to this cylindrical core as the *inner cylinder.* The surrounding cavity also consists of a stainless steel foil having the shape of a cylinder that is surrounded by support and insulation material which allows it to maintain its shape. The inner surface of the cavity will be referred to as the *outer cylinder.* Our interest lies in the heat transfer which takes place in the annulus formed between these two cylindrical surfaces.

3.1.1 Cylindrical core

The core of the annulus is formed by a vertical cylindrical surface covered with a thin stainless steel foil 50.8 μm (0.002″) thick. The shape of the inner cylinder was created from a tube of a woven glass phenolic resin material known as G-11 (P&A Plastics Inc., Hamilton, Ontario, Canada). This material was chosen after an extensive search due to its high temperature rating[2], (up to 180 °C, according to the supplier), high rigidity and dielectric strength. G-11 has a dielectric breakdown voltage of 40 KV (ASTM test method: Condition D 48/50)[3] and a thermal conductivity of 0.288 W/m·K. As well, this tube is given

---

[2] By comparison to other electrically non-conductive materials which are manufactured in large tubular shapes.

[3] According to the *Department of Defence Index of Specifications and Standards* (DODISS); Document number: MIL-I-24768/3 type GEB, 25 February 1992.

its shape by being rolled over a mandrel which generally produces straighter cylinders than extrusion does. A detailed breakdown of the cylindrical core section is shown in Figure 3.

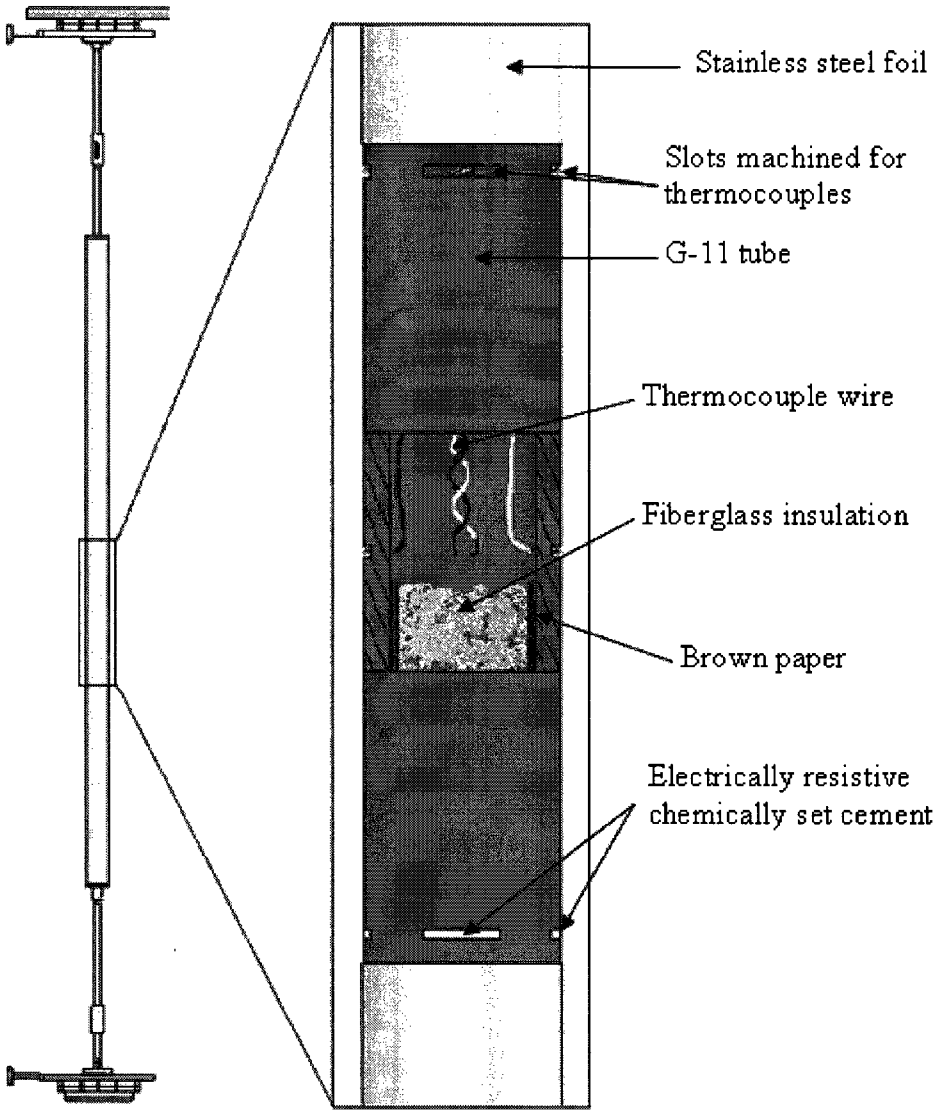

Figure 3 – Inner cylinder and supports with a dissected view of the inside of the core

The outside diameter of the inner cylinder was chosen to be 50.8 mm (2.0″ ± 0.011″, according to the manufacturer), primarily because of the availability of G-11 tubes with the length that we needed in this diameter. The thickness of the inner cylinder had to be

sufficient to house a large number of thermocouples without blocking too much the inner space through which all wires were passed. We chose an inner diameter of 38.1 mm (1.5″ ± 0.008″, according to the manufacturer) as this was available and provided us with a wall thickness of 12.7 mm (0.5″) which was sufficient to ensure the rigidity of the core section.

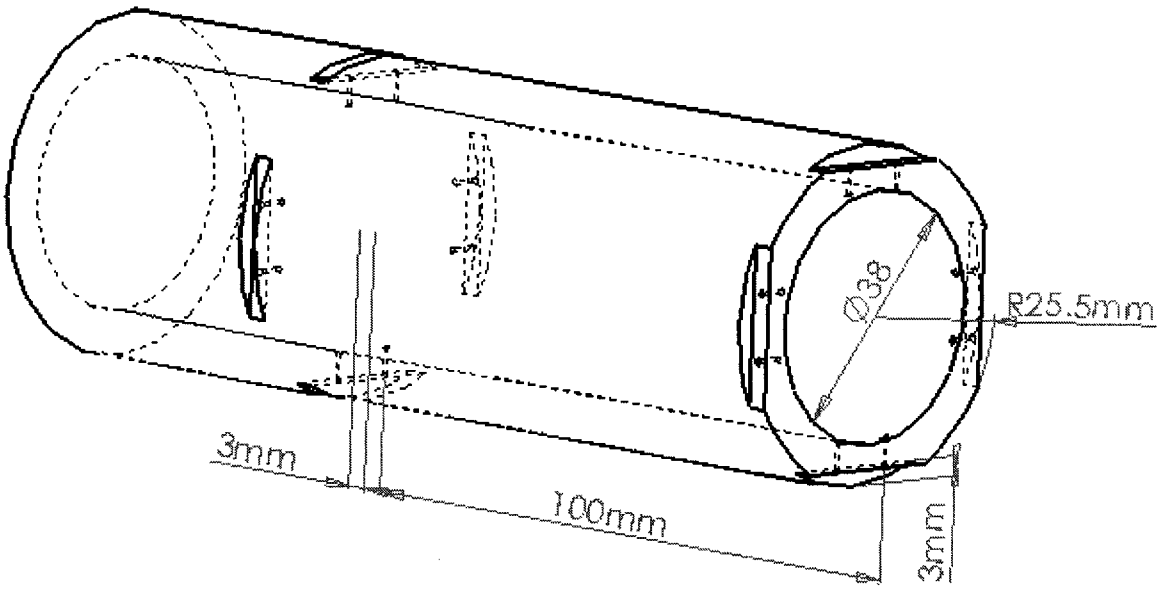

Figure 4 – Sketch of section of inner cylinder core showing slots cut out for thermocouple placement

Four 3 mm deep and 3 mm wide slots were made every 10 cm along the entire 1.5 m length of the inner cylinder core as seen in Figure 4. The slots were made at 90° intervals of each other and two 1 mm diameter holes were placed 10 mm apart in the centre of each slot in order to accommodate the strands of the thermocouple wires. A total of 64 thermocouples were placed inside the drilled holes, however, only 48 thermocouples were intended to be used and the remaining 16 would be extras. The reason we did not intend to use all the thermocouples was because we assumed that thermal symmetry existed with respect to the *y* axis, as seen in Figure 5.

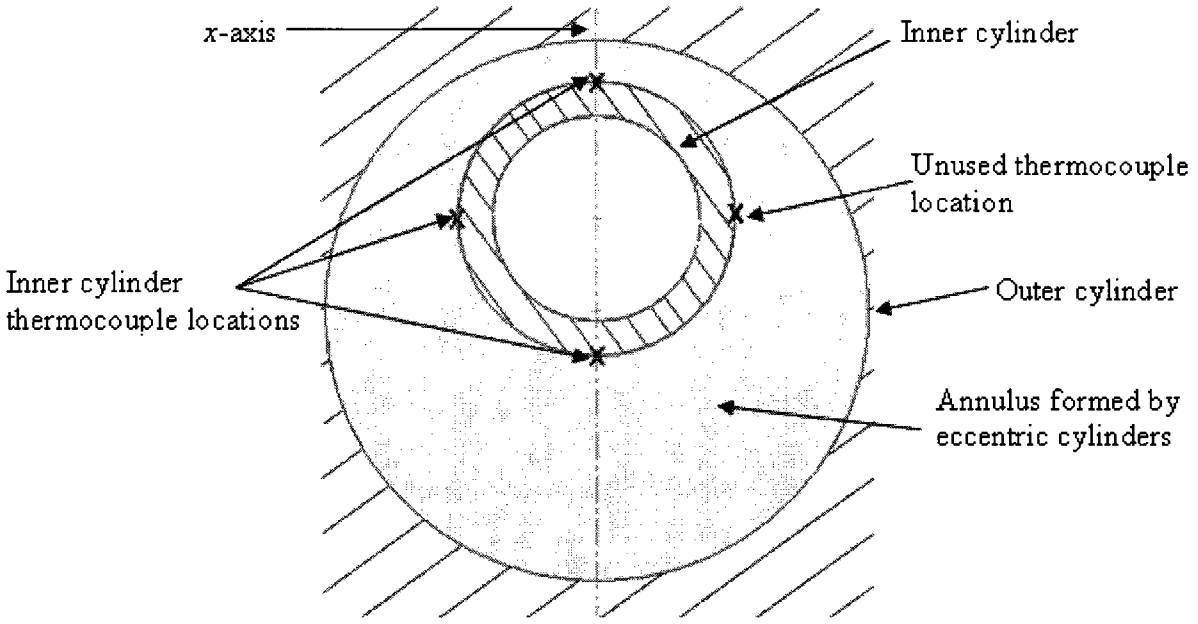

Figure 5 – Sketch of cross-section of the annulus formed by a cylindrical core and an eccentric cylindrical cavity showing the inner cylinder thermocouple locations

The thermocouples were placed such that the wiring would pass through the interior of the inner cylinder. Each thermocouple junction was securely positioned as closely to the outer surface of this cylinder as possible. To ensure that the thermocouples would not move after they were properly positioned, their stems were glued to the G-11 tube. A razor was placed at the surface of the cylinder and used as a measuring tool. Each thermocouple was placed as close to the razor as possible until only a slim margin of light could be seen between the blade edge and the thermocouple tip. This was done to make sure that all the thermocouples were as close to the surface as possible without perturbing from it. Each thermocouple was delicately positioned and, with the help of a vernier calliper, slight adjustments were made to ensure that all 64 thermocouples were properly aligned in the

centres of the slots machined for them. Figure 6 shows how the thermocouples were placed in a cross section of the inner cylinder.

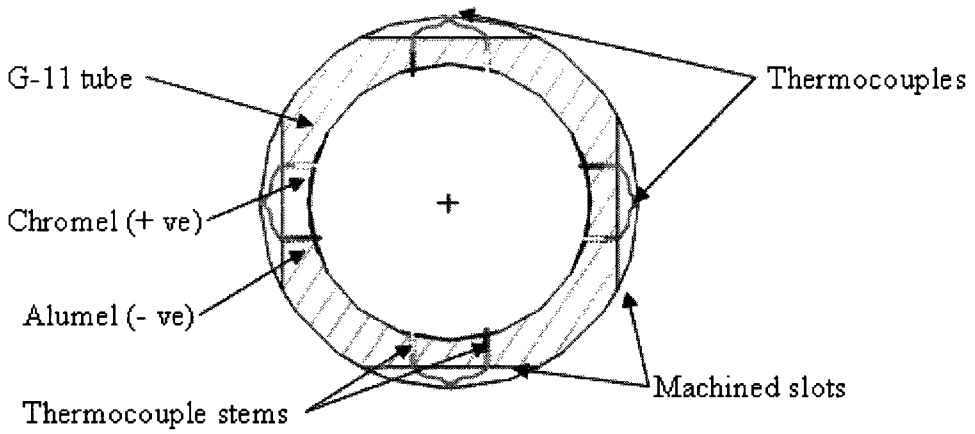

Figure 6 – Sketch of cross-section of inner cylinder showing details of thermocouple positioning

Teflon insulated, 0.015″ single strand Chromel and Alumel thermocouple wires (Omega Engineering Inc., Laval, Quebec, Canada), were chosen and individually welded using a thermocouple welder (Unitek Equipment, Model TCW Stock No. 1-196-02, Monrovia, California, USA) to form k-type thermocouples. The k-type was chosen because it is the most common general purpose type thermocouple and it was suitable for our temperature range. In retrospect, however, a t-type thermocouple would have been a better choice, because it has lower tolerances (±1°C, as opposed to ±2.2°C for the k-type), according to the manufacturer) for the temperature range we encountered.

To seal the thermocouple slots machined into the G-11 tube and electrically insulate the thermocouples while still providing good heat transfer to the junction, a special, high temperature, chemically set cement was used (OMEGABOND 600, Omega Engineering

Inc., Laval, Quebec, Canada). This cement provides good heat conductivity (1.44 to 1.73 W/m·K) and good electrical insulation (its dielectric strength at 21°C was 2.99 to 4.0 kV/mm), and adheres to most clean surfaces. The cement was filled into the machined slots (Figure 6) after the positioning of the thermocouples and special care was taken to ensure that no large air bubbles or spaces were left in the slots. After the cement cured, a file was used to remove any excess material which bulged out and the cylinder surface was sanded smooth. The inner cylinder was then placed on three V-blocks on a precision ground flat aluminum table. With the help of a height gauge, measurements were taken along the length of the cylinder to help identify any bending in the tube; no significant bending was found.

A 50.8 μm (0.002″) thick type 304 stainless steel foil tape with a 50.8 μm (0.002″) thick adhesive layer was then used to cover the inner cylinder and only a small seam of approximately a third of a millimetre was left to account for any thermal expansion of the foil. The foil was marked and cut to the proper dimensions using scissors. This cutting technique was used as we lacked more precise equipment capable of cutting a straight edge along such a thin foil. Although great care was taken to ensure a straight cut, the accuracy is limited by the means. The seam was positioned such that it lies adjacent to the unused row of thermocouples mentioned previously, so that it was as far as possible from the remaining three thermocouples at each height, which were used for the main measurements. The stainless steel foil was chosen based on the relatively high electrical resistivity of stainless steel, its relatively low thermal conductivity and its rigidity as compared to other readily available metallic foils.

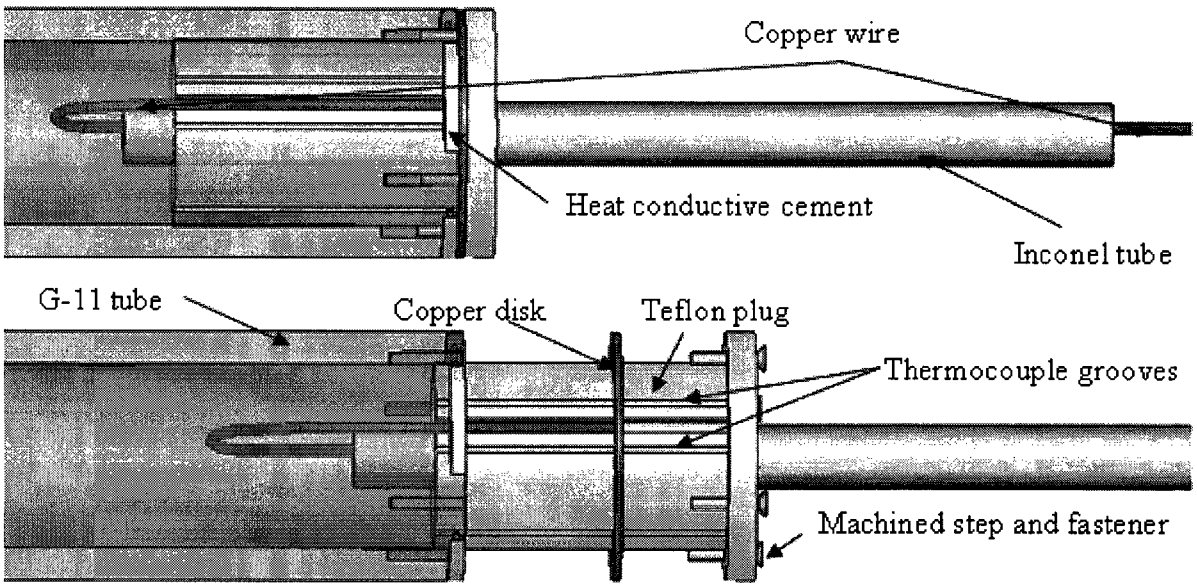

Figure 7 – Exploded view of end section of inner cylinder without the stainless steel foil

A Teflon plug was constructed so that it has a tight fit with the inner part of the inner cylinder and has a step so that it can be fastened using four screws to the end of the inner cylinder as seen in Figure 7. Eight grooves were made to accommodate end thermocouples that would pass between the Teflon plug and the inner wall of the inner cylinder. Also, grooves were made for two copper wires that would be used as electrical conductors to supply current to a copper disk which would eventually spread the current evenly to the stainless steel foil as seen in Figure 8

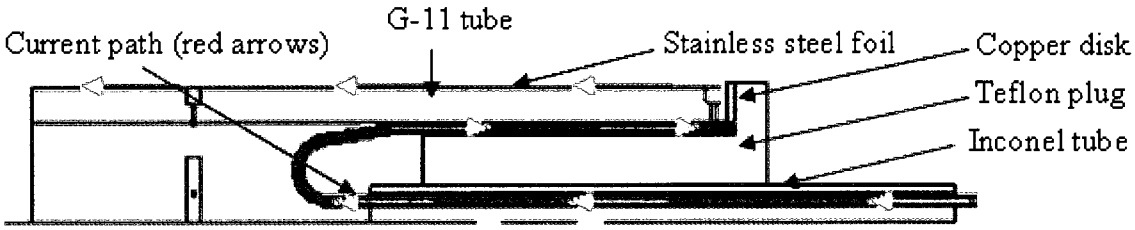

Figure 8 – Sectioned schematic of end of inner cylinder showing current path (red arrows) from the copper wire to the copper disk and then to the stainless steel foil

An Inconel hollow tube with an outer diameter of 13.0 mm and an inner diameter of 10.7 mm was inserted with a sliding fit in the centre of the Teflon plug. This tube acts as a housing through which all the thermocouple wires would eventually be passed out of the inner cylinder. As well, it acts as the main support which holds the inner cylinder at both ends. The Inconel tube also acts as an added vessel through which current moves, thus further minimizing losses in this section. Inconel was chosen primarily because of its availability in the lab but also because of its rigidity and its resistance to oxidation and corrosion.

After the thermocouple wires were fixed to the inner cylinder, half of them were drawn out of either end of the inner cylinder. All thermocouple wires were subsequently twisted in pairs and labelled. A cylindrical roll of brown paper was then inserted into the inner cylinder such that it pushed the thermocouple wires against the wall to protect them and keep them in place while the space in the middle of the cylinder was being packed with fibreglass insulation. The stainless steel foil was folded at the ends of the cylinder such that it would come in between the copper disk and the G-11 tube as seen in Figure 8. The

Forty-eight thermocouples were welded and their tips were hammered flat, as seen in Figure 9, so that they would not pierce through the stainless steel foil once installed. The layers of tape, brown paper, and adhesive protector were sliced off at marked locations where these thermocouples would be placed. Strips of Teflon tape were then glued directly onto the exposed stainless steel foil in these locations. The flattened thermocouples were then glued on top of the Teflon tape in their marked locations. They were then individually taped to the brown paper with some slack left in order to protect against the thermocouple being tugged out of its position. Similar to their placement in the inner cylinder, three thermocouples were placed 90° apart every 10 cm along the height. Only three thermocouples were used under the assumption of thermal symmetry. A galvanized steel tube with three holes drilled every 10 cm at the locations where the thermocouples would be placed was then wrapped around the outer cylinder. The galvanized steel was fastened by duct clamps and construction wire as well as being taped with stainless steel foil strips which proved to be extremely powerful and handy. A schematic of the layers used to form the wall of the outer cylinder can be seen in Figure 10.

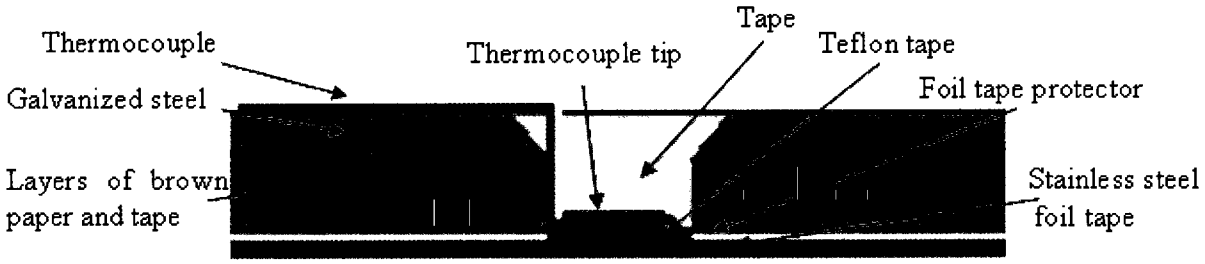

Figure 10 – Cross- section of the outer cylinder showing placement of thermocouples as well as the layers which make up the walls of the outer cylinder

Two Lexan plates with dimensions 250 mm × 250 mm and 6.35 mm (1/4″) thick, were machined to fit at either end of the outer cylinder to give it support; their placement can be seen in Figure 11. The stainless steel foil was then cut into strips at the ends and bent over and taped to the Lexan brackets using the adhesive side of the foil. Aluminum plates of equal length and width to the Lexan plates and 2 mm thick were placed over the support brackets and tightly fastened to it such that the stainless steel was sandwiched in between. This ensured that the foil would not slide off, and also provided a mean of evenly distributing the current to the stainless steel foil, as aluminum is an excellent electrical conductor.

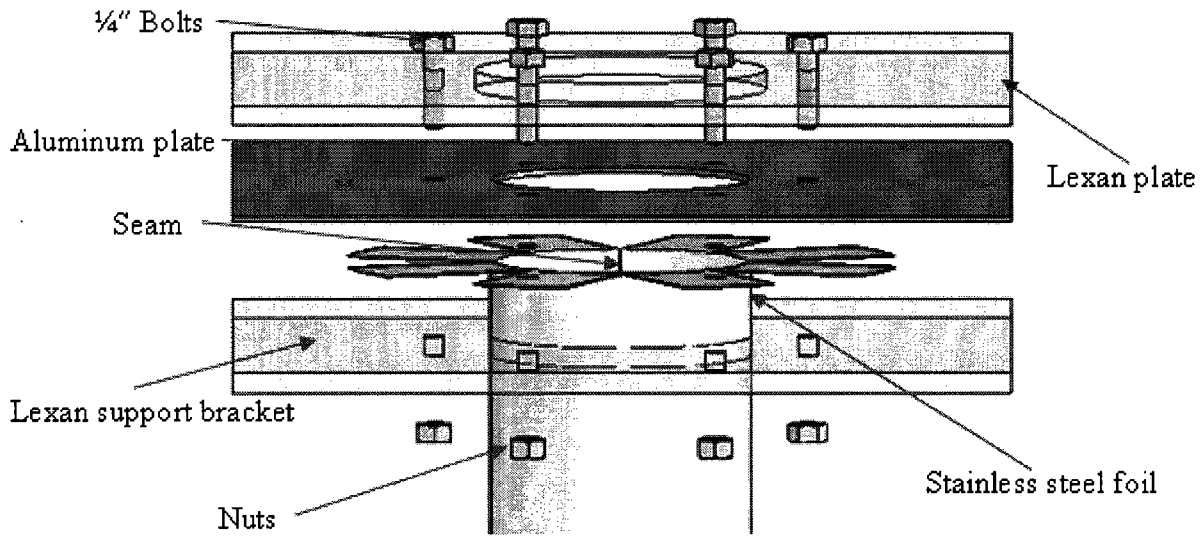

Figure 11 – Exploded view of one end of the outer cylinder; including the Lexan supports, a conductive aluminum plate, and stainless steel foil with seam

The aluminum plate and the Lexan support bracket both had a hole bored out of the centre with the same diameter as that of the cylindrical stainless steel foil, but with tolerances taken into consideration to account for the thickness of the foil itself. At the bottom of the outer cylinder, an additional Lexan plate with the same dimensions as the

Lexan support bracket was machined and bolted onto the end. This was done in order to keep the construction of the top and bottom of the outer cylinder as similar to each other as possible as the top of the cylinder was bolted to a Lexan plate attached to the frame, as will be discussed in the following section. To avoid any interference to the flow from the unheated Lexan section at the extremities of the outer cylinder, the top and bottom Lexan plates had their openings bored slightly larger than that of the stainless steel foil cylinder. This opening was 94 mm in diameter whereas the inner diameter of the outer cylinder was 83 mm. Two heavy gauge copper wires were then bolted onto the aluminum plates, one at each end of the outer cylinder, in order to pass current through to the stainless steel foil.

The forty-eight thermocouples were split into two groups, properly marked, and collected together to form two thick bundles which were connected to the data-acquisition system. The outer cylinder was wrapped in 150 mm thick fibreglass insulation and then covered with PET aluminum bubble insulation. One thermocouple was placed midway inside the fibreglass insulation and another between the fibreglass insulation and the aluminum bubble insulation in order to serve for estimating heat losses through the outer wall of the outer cylinder.

3.1.3 The frame

The frame is what holds the outer cylinder in place, among other functions; it has mounts for the supports of the inner cylinder, the temperature data acquisition panel and an enclosed chamber at the bottom. This enclosure will be used for flow velocity measurements and will be discussed in more details later on. The frame itself is mainly constructed using 38.1 mm × 38.1 mm × 47.6 mm (1.5″ × 1.5″ × 3/16″) angle iron pieces welded together. The top section of the frame is constructed using 25.4 mm × 25.4 mm × 31.8 mm (1.0″ × 1.0″ ×

1/8″) angle iron. The dimensions of the frame are presented in Figure 12. This frame was available from a previous experiment and minor modifications were made in order to accommodate the present needs. The frame has four bolts at each of its bottom corners which can be used to finely adjust the frame's vertical orientation. Locking nuts have also been placed in order to fix the alignment bolts in position once the frame has been leveled properly.

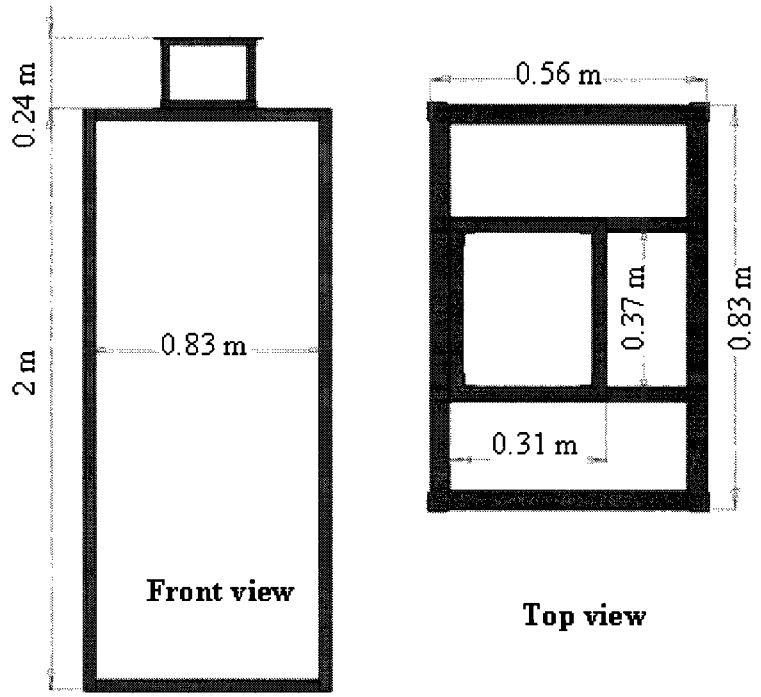

Figure 12 – Main frame construction showing the front and top views

The bottom section of the frame was reinforced using angle iron and a small section of steel plate was welded to the frame where we expected the weight of the inner cylinder to apply. A 63.5 mm (¼″) thick plate of Lexan was then used as the floor of the frame, and this was secured in place. Two sub-frames with dimensions 825 mm × 574 mm × 25.4 mm were

constructed out of 25.4 mm angle iron welded together and a piece of 6.35 mm thick Lexan was fastened to them as seen in Figure 13. These sub-frames acted as the supports at each end of the outer cylinder. A square section was cut out of the Lexan plate attached to the bottom outer cylinder support frame. Moreover, a 94 mm in diameter opening along with a bolt circle was made in the Lexan plate attached to the top outer cylinder support frame. These can all be seen in Figure 13.

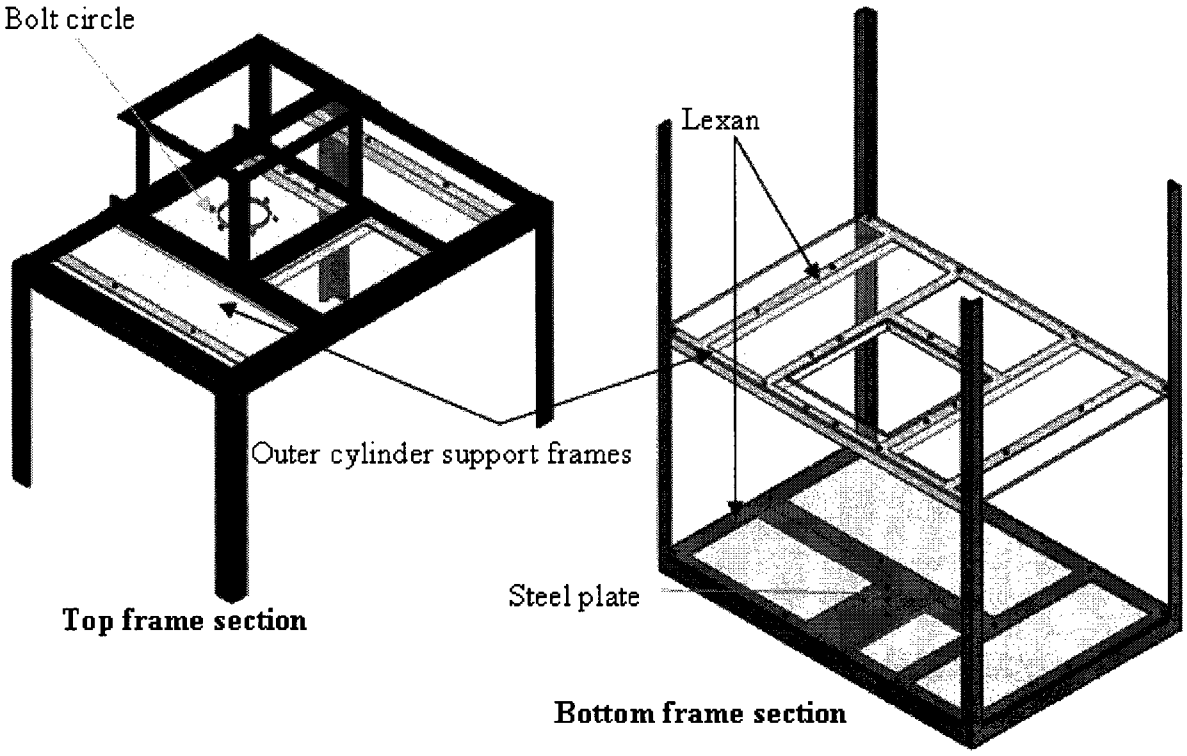

Figure 13 – Isometric views of top and bottom sections of the frame showing the two support sub-frames for the outer cylinder

While the bottom support frame is labelled as a supporting element, in reality, it functions more as an alignment entity as it does not apply any upwards force on the outer

cylinder. The outer cylinder is supported entirely by the top support frame to which it is bolted by means of the six-hole bolt circle seen in Figure 13. The bottom part of the outer cylinder hangs freely in order to avoid restricting the outer cylinder stainless steel foil as it expands while being heated. In testing prototypes of the outer cylinder, it was found that restricting the expansion of the foil as it is being heated would cause it to deform and wrinkle. Two aluminum alignment brackets, seen in Figure 14, were used to keep the outer cylinder vertical whereas small pieces of flexible rubber tubing were used to push the support brackets onto the alignment brackets.

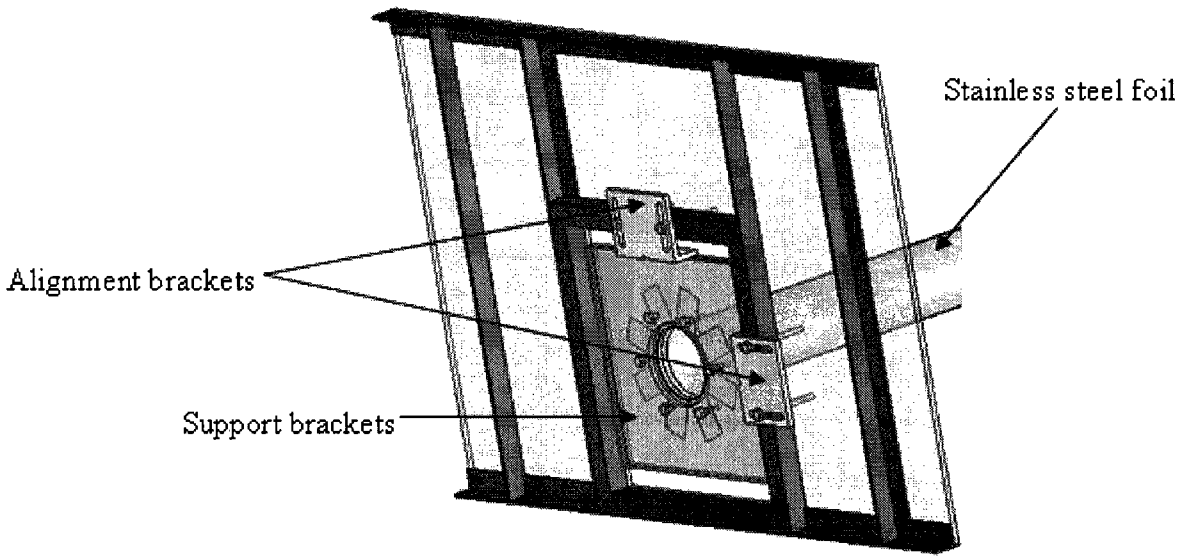

Figure 14 – View of the underside of the bottom support frame, showing the alignment brackets and a stripped version of the outer cylinder with only the stainless steel foil and support brackets showing

Two Lexan windows were made with aluminum frames to fit at the bottom section of the frame enclosing the front and back sections below the bottom support frame as seen in

Figure 15. The window frame in the back is constructed of two pieces which are hinged together, and form a tight seal when closed, while the front window frame is fixed. A square section in the Lexan of the front window was cut out to accommodate an inlet made out of 6 mm thick glass plates affixed together to form a 103 mm × 103 mm short square duct. After the frame is sealed, this passage will be the only air inlet into the annulus and the top of the outer cylinder will be the only air outlet for the annulus. A sheet metal support bracket was made in order to hold the glass inlet in place on the Lexan window.

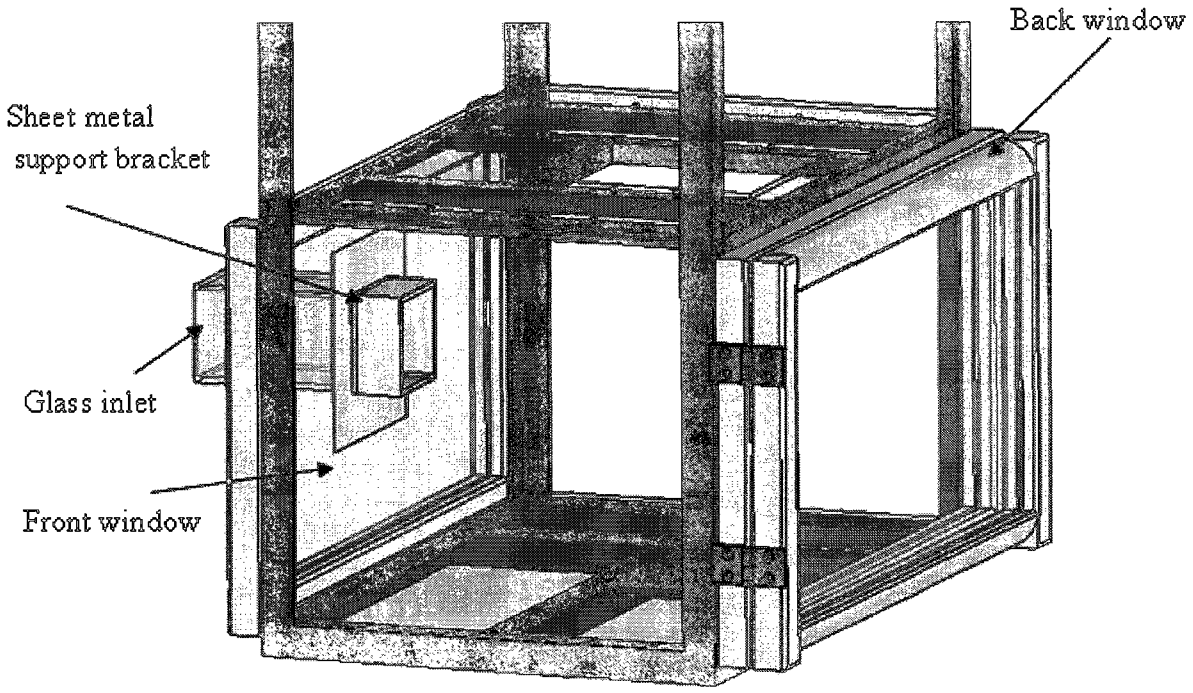

Figure 15 – Bottom section of frame showing front and back enclosures

The sides of the frame along with the front and back above the two windows were covered with 1 mm thick mild steel sheet metal. The sheet metal was riveted in place except

for the back panel which was only screwed in place to allow for easy access in case maintenance is required. Silicon was used to seal all the open gaps inside the frame to ensure that the only air inlet was the designated glass passage when experiments were performed. The glass passage was sized by trial and error by fabricating numerous paper square inlets of different sizes and running our testing using the highest power setting with the highest flow rate configuration (which was assumed to be the concentric one). It was found that the smallest square inlet cross-sectional area for this specific configuration of this enclosure which would not cause a noticeable change to the temperature in the annulus was roughly 103 mm × 103 mm. The different sizes used for determining this were 82 mm × 82 mm, 90 mm × 90 mm, 103 mm × 103 mm and 150 mm × 150 mm. After observing the effects that the different sizes had on the temperature of the annulus when the back window of the bottom enclosure was fully open or when only the glass passage was open, it was determined that a 103 mm × 103 mm cross sectional area satisfied the selection criterion.

3.1.4 Inner cylinder supports

The inner cylinder supports consist of two main parts: the bottom support, which carries all the weight of the inner cylinder, and the top support, which ensures that the inner cylinder remains vertical. A bottom support disk, seen in Figure 16, is fastened to the steel plate at the bottom of our main frame and rests above the Lexan plate which forms the floor of the frame. This support disk has an elevated cylindrical core that is 12.7 mm (0.5″) high and has a diameter of 60 mm around which a support clamp is placed. The support clamp is 12.7 mm (0.5″) high and 148.4 mm in diameter; it rests flat on the face of the support disk and is free to rotate about its z-axis. This support clamp has two holes upon which a Plexiglas buffer is mounted and an additional two holes which line up with similar machined

openings in the bottom disk through which an alignment pin can be placed. The alignment pin is used to fix the bottom clamp at four azimuthal positions 90° apart.

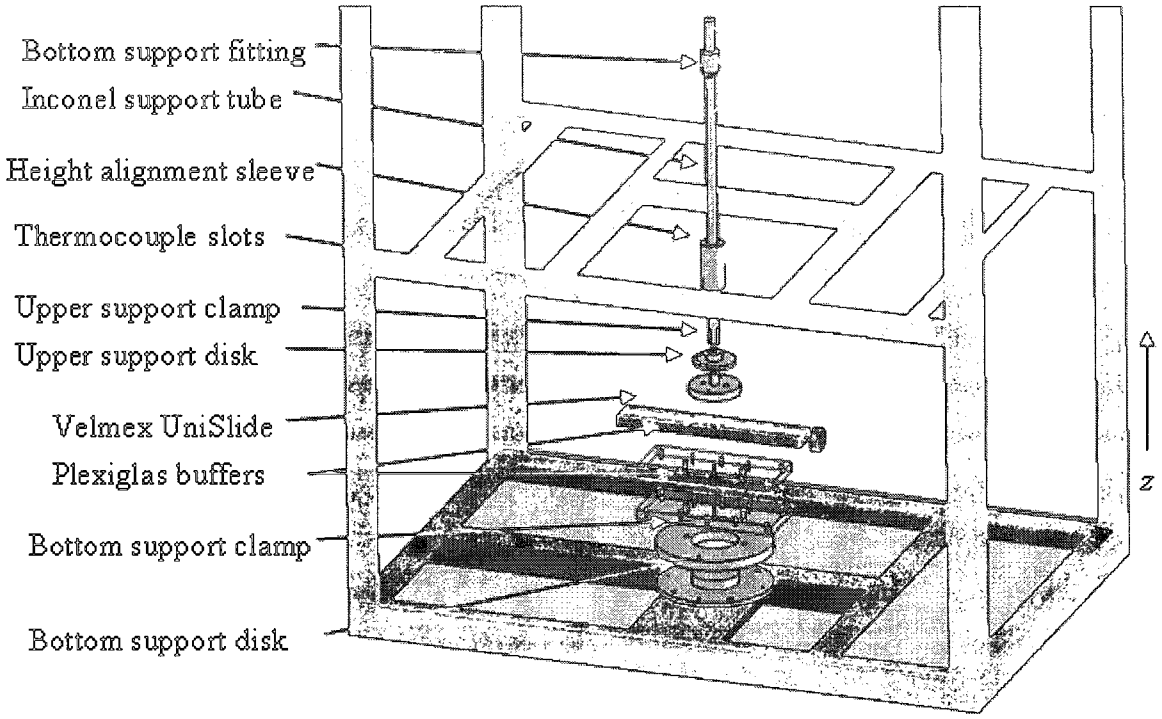

Figure 16 – Exploded view of bottom support for inner cylinder

The Plexiglas buffers consist of two 12.7 mm (0.5″) thick Plexiglas plates, with dimensions 77 mm × 180 mm. One of the Plexiglas buffers is fastened to the bottom support clamp whereas the other one is fastened to a Velmex UniSlide traversing mechanism. These buffers ensure that the inner cylinder is electrically insulated from the main frame at the bottom end. The two Plexiglas plates are fastened together using six screws which are threaded into the Plexiglas.

The traversing assembly (UniSlide, Velmex series A1500, Bloomfield, New York, USA) consists of a linear dovetail bearing which traverses inside an aluminum block with

the help of a lead screw fixed to one end of the assembly. Turning the lead screw will traverse the dovetail bearing forward or backward depending on the turn direction. Two threaded mounting holes are found in the dovetail bearing to which the upper support disk was fastened. The upper support disk is identical to the bottom support disk except for its dimensions. The elevated cylinder in this support disk has a diameter equal to the inner diameter of the Inconel support tube which fits into it. An upper support clamp with 19 positioning holes 10° apart and an inner diameter equal to the outer diameter of the Inconel support tube was placed flat upon the upper support disk surface.

The upper support clamp is fixed to the Inconel support tube with the help of a set screw and the Inconel support tube rotates freely about the z-axis of the upper support disk. Using the positioning holes in the upper support clamp, the inner cylinder could be fixed horizontally at azimuthal positions spanning 360° at 10° intervals. This would permit the measurement of azimuthal temperature variations at different heights around the inner cylinder using only one thermocouple at each height. Having three thermocouples at each height permits comparisons between readings of different thermocouples at the same position, thus reducing the uncertainty of these measurements.

The Inconel support tube has three grooves at the bottom through which the thermocouples and the conductive copper wires can be drawn out. An added benefit of the upper support clamp is that it adds rigidity to this weakened section of the tube by wrapping around it with a tight fit at the bottom while still allowing the thermocouples and conductive wire to come out. A stainless steel sleeve is welded to the Inconel support tube and is used to prevent the inner cylinder from sliding down the tube. In order to adjust the height of the

Inconel support tube, it was cut a short distance towards the bottom and then rejoined using an aluminum sleeve with two set screws, one for each of the top and bottom sections.

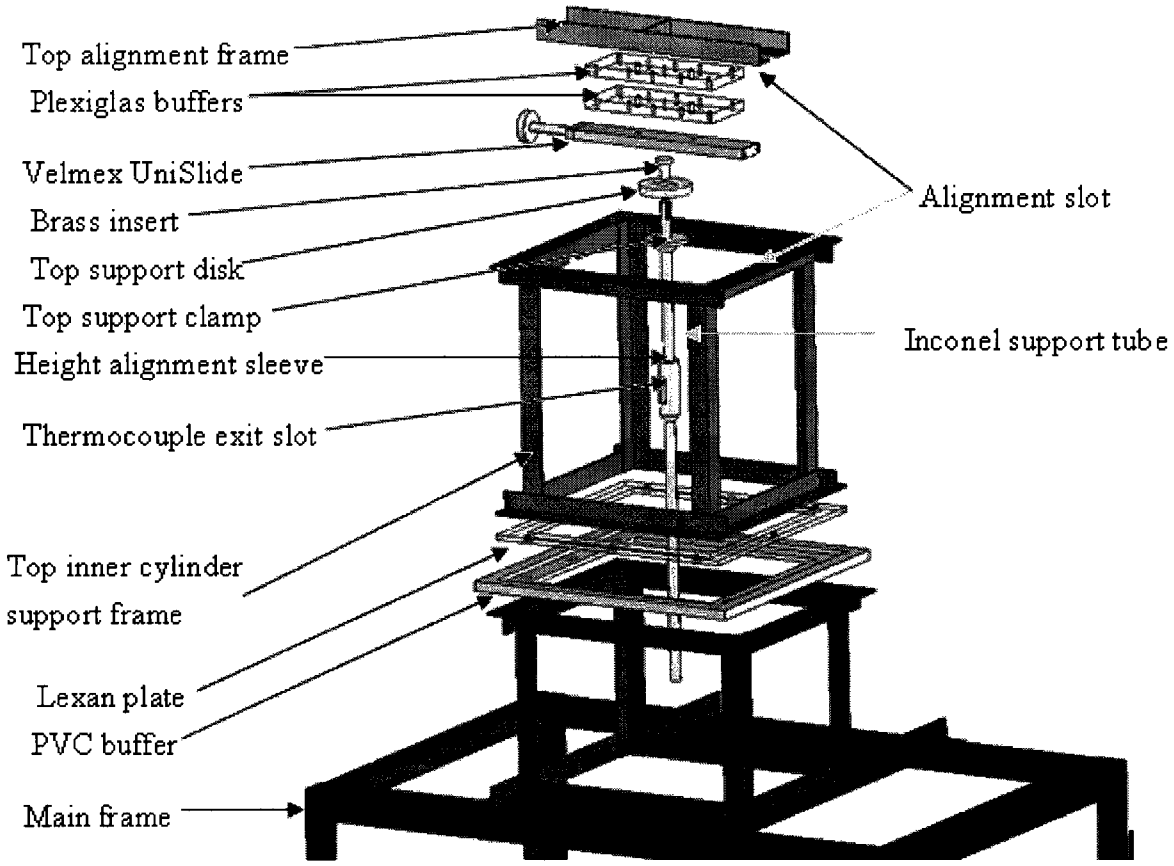

Figure 17 – Exploded view of top support for inner cylinder

The top support for the inner cylinder, seen in Figure 17, rests upon a machined square PVC buffer which is fastened to the main frame on top of the smaller top section. The PVC buffer has a machined groove into which a Lexan square plate of dimensions 315 mm × 315 mm and a thickness of 63.5 mm (1/4") can be inserted. The Lexan plate and the PVC buffer both have machined square openings in their centres with dimensions 260 mm × 260 mm. A frame constructed from welded 25.4 mm × 25.4 mm × 31.8 mm

(1.0″ × 1.0″ × 1/8″) angle iron, which is 310 mm high and has inner dimensions equal to those of the machined opening mentioned previously, is fastened to the Lexan plate. This setup allows one to remove the top inner cylinder support frame, rotate it if needed and place it back on top of the main frame without the need of any fasteners or realignment. Furthermore, the PVC buffer ensures that the top inner cylinder support frame is electrically insulated from the main frame.

Two pieces of 25.4 mm × 25.4 mm × 31.8 mm (1.0″ × 1.0″ × 1/8″) angle iron were used to make up the top alignment frame which is 315 mm long and 75 mm wide. Three pieces of 31.8 mm (1/8″) steel were used to weld and reinforce this frame and provide the proper spacing between the angle iron shafts used. The top alignment frame has four holes through which bolts were inserted to fasten it to the top inner cylinder support frame. These bolts went through slots made on each side of the top inner cylinder support frame and fine adjustments could be made before the bolts were tightened in order to fasten the two frames together. Plexiglas buffers similar to those used in the bottom inner cylinder support setup were subsequently fastened to the top alignment frame.

A UniSlide assembly identical to the one used for the bottom inner cylinder support is fastened to the bottom side of the Plexiglas buffers and a top support disk with a brass insert is fastened to that using socket head cap screws. The brass insert acts in a similar manner to the elevated cylindrical core of the upper support disk in the bottom inner cylinder support structure. The insert was chosen in order to allow the top part of the inner cylinder to rotate freely with minimal resistance. The insert was then placed into the top end of an Inconel support tube similar to that used in the bottom support structure and a clamp similar to that used in the bottom support structure was fitted over that and fixed in place by a

setscrew. The Inconel support tube was cut and rejoined by an aluminum height alignment sleeve which was fastened to both ends of the tube using setscrews. The alignment sleeve has a slot made in its centre through which the thermocouples and the conductive copper wire entering the bottom end of the Inconel tube from the inner cylinder were drawn out.

Two dial indicators with a resolution of 0.001″ were used for the top and bottom inner cylinder supports to measure the distance traversed by each. The dial indicator used for the top inner cylinder support (Mitutoyo, Model No. 3428-10) was fixed to the top inner cylinder support frame and its sensor comes into contact with the side of the top support disk. The dial indicator used for the bottom inner cylinder support (Mitutoyo, Model No. 2416-10) was fixed to the Lexan flooring of the main frame and its sensor comes into contact with the side of the bottom support disk.

3.2 Instrumentation

3.2.1 Power supply

Two identical 10 kW power supplies (Sorensen, DCR-T series, San Diego California, USA), one for each cylinder, were used to power the stainless steel foils of the inner and outer cylinders. The maximum output of each power supply is 180 A at 55 V DC. The voltage and power output of the power supply could be controlled either by knobs on the front panel, or through remote control by resistive programming. There is also an LCD display on the front panel, which indicates the voltage and the current being drawn from the power supply at any given time. Alternatively, remote sensing can be used to monitor these parameters and their values could be recorded using a data acquisition board.

The controls on the front panel of the power supply were used to get preliminary results and estimate the power input into the annulus. However, for better results, more accurate sensing was needed, and also better voltage and current control. The power supply was placed about 8 m away from our setup in order to ensure that the fan used to cool the power supplies did not affect the experimental setup. As a result, there were some power losses in the long cables used to transport the power from the power supply to the test section. To minimize these losses, heavy gauge cables were used. It was also possible to measure the voltage drop across the test section using the built-in remote sensing option of the power supplies. In effect the voltage regulation and readout was done at the load rather than at the power supply output terminals, hence correcting for the voltage drop in the load leads. Installing the remote sensing leads was as simple as connecting the load to a terminal bar using copper wiring.

A custom-designed circuit board was built which used 50-turn potentiometers that would be adjusted manually to limit either the voltage or the current output of the power supply. This remote control mechanism was used to finely adjust the limiting output factors of the power supply as opposed to using the built-in 10 turn potentiometers which were found to be too coarse. The external resistance programming method was easily implemented by connecting the potentiometers to a terminal bar found on the back of the power supply as directed in the user's manual.

As the stainless steel foil of the test section heats up, its resistance would increase; thus, if one were to limit the current, the voltage would vary because of the change in resistance. Similarly, limiting the voltage would cause the current to change with the resistance. In order to monitor this change, which would allow us to also monitor the heat

flux from the annulus walls; we decided to record the voltage and current values throughout the experimentation runs using a data acquisition board and LabVIEW 8.5 for monitoring and recorded the inputs.

The data acquisition board (NI PCI-6024E) used was a National Instruments PCI board with 12-bit resolution, 16 analog inputs with selectable ranges of ±10 V, ±5 V, ±500 mV and ±50 mV, 2 analog outputs of ±10 V with an output rate of 10 kHz and a maximum sampling rate of 200,000 samples per second. The current from each power supply was monitored by connecting a pair of leads from an internal shunt built into the power supplies to the data acquisition board. The voltage drop across the test section was measured by connecting a pair of leads from each cylinder in the annulus to the data acquisition board. With the use of a hand-held voltmeter and a hand-held ohmmeter, we validated the results displayed by the monitoring software of the data acquisition board. Figure 18 shows a snapshot of the LabVIEW graphical user interface created for monitoring and controlling the power supplies. The LabVIEW block diagram can be found in Appendix A.

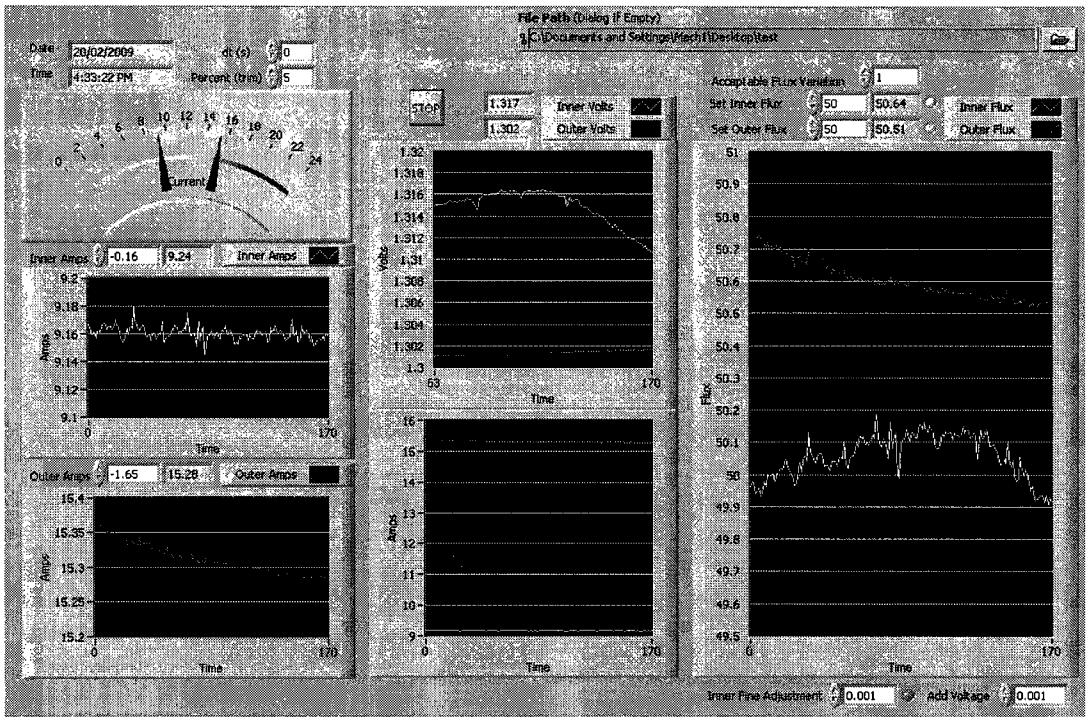

Figure 18 – Snapshot of power supply monitoring and control GUI built in LabVIEW

The signal coming from the power supply was very noisy and contained random spikes which we could not account for. In an effort to reduce the noise, we took a large number of samples (50,000) and computed their arithmetic mean after removing potential outliers identified as the 5% most extreme values in the sample. This helped reduce the noise as well as eliminate the spikes. The cause for the noise was not directly apparent, however, it is possible that some was generated by the connection board that was used to connect the leads from the power supply to the data acquisition board. Another source could have been the internal circuitry of the power supply itself. Several attempts were made to generate a cleaner signal, and considerations were made to use a higher resolution analog to digital conversion, however, ultimately as the readings generated were acceptable for our needs, we decided to focus on other aspects of the experiment.

The LabVIEW program recorded, along with a time stamp, the voltage and the current every 10 s for the two power supplies which were used. While running the LabVIEW program with the power supplies turned off, it was noticed that we needed to correct the results for a zero offset that was attributed to the operational amplifiers in the connection board. The amount of this correction was taken to be the arithmetic average of all readings recorded over a 24-hour period. This offset was integrated into the LabVIEW program and, after turning the power supplies on, we found that the current values measured by the data acquisition system and the hand-held ohm-meter were in good agreement. The effect of the operational amplifiers on the voltage was not an issue as the voltage was relatively high by comparison to the required offset.

We should note that after the majority of our experiments were completed, some modification was done to the acquisition setup, in which the single-ended inputs were replaced with differential ones. As well, after noticing that the range of the data acquisition signal input could be decreased from ±500 mV to ± 50 mV, which was sufficient for our measurement of the current, we managed to eliminate the previously mentioned spikes without resorting to trimming the input data. This was done after the majority of the experiments had already been performed, but we did not find it necessary to repeat all the experiments as we did not anticipate any significant change in our results.

3.2.2 Temperature data acquisition system

The temperature data acquisition system consisted of a system hub (Sensoray 2601, Tigard, Oregon, USA), also referred to as the main module, to which is connected, through Cat-5 Ethernet cables, six Sensoray 2608 I/O modules. The Sensoray 2608 module has 16 analog inputs and an ADC resolution of 16-bits and is capable of taking 500 samples per

second for each channel. For thermocouple readings, the 2608 module accepts ±100 mV inputs and has built-in cold-junction compensation as well as open-circuit detection. In addition, these modules have onboard temperature sensors which are mounted near the analog input terminals to provide reference junction compensation.

A sheet metal cabinet was constructed to house all the I/O modules along with the power supply for the main module and a wireless router through which we could communicate with the main module. The cabinet separates the power supply and the wireless router from the rest of the setup to avoid any interference of the heat generated by these devices. After consulting with the Faculty of Engineering Computing and Communication Services, we were advised not to use the wireless router. Instead, we were forced to communicate with the main module using an Ethernet cable. The cabinet with all its components can be seen in Figure 19.

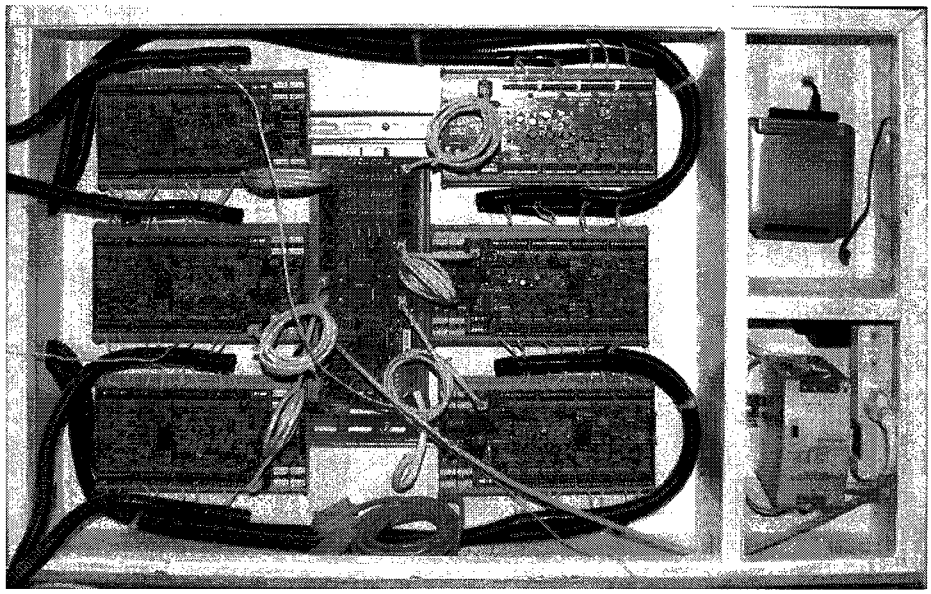

Figure 19 – Data acquisition system and cabinet

A Visual Basic program was developed to monitor and record the temperature inputs from the 96 thermocouples into the data acquisition system. The program was written in Visual Basic 6.0 and, in addition to recording the inputs, it had a wide set of functionality which made handling a large number of readings much simpler. The program interacts with a middleware DLL file provided by Sensoray, which in turn communicates with the main module.

Figure 20 shows the welcome page in the program. Starting from this page, the user could start recording a new set of data, or alternatively load a previous set, add new acquired data to it or just view and analyze a previous data set.

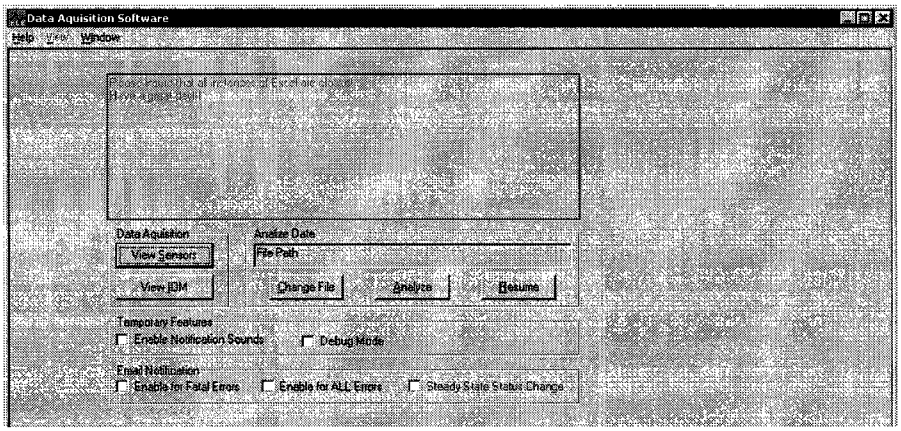

Figure 20 – Data acquisition software start up page

The program has a configuration page which allows the user to set a number of parameters. These parameters include the number of samples to be averaged and the sampling rate. The user can also set the conditions under which a steady state can be

assumed. Previous configuration files and calibration files can also be set in this page along with a variety of debugging, file saving and notification options. The configuration page can be seen in Figure 21 with the connection IP address partially masked.

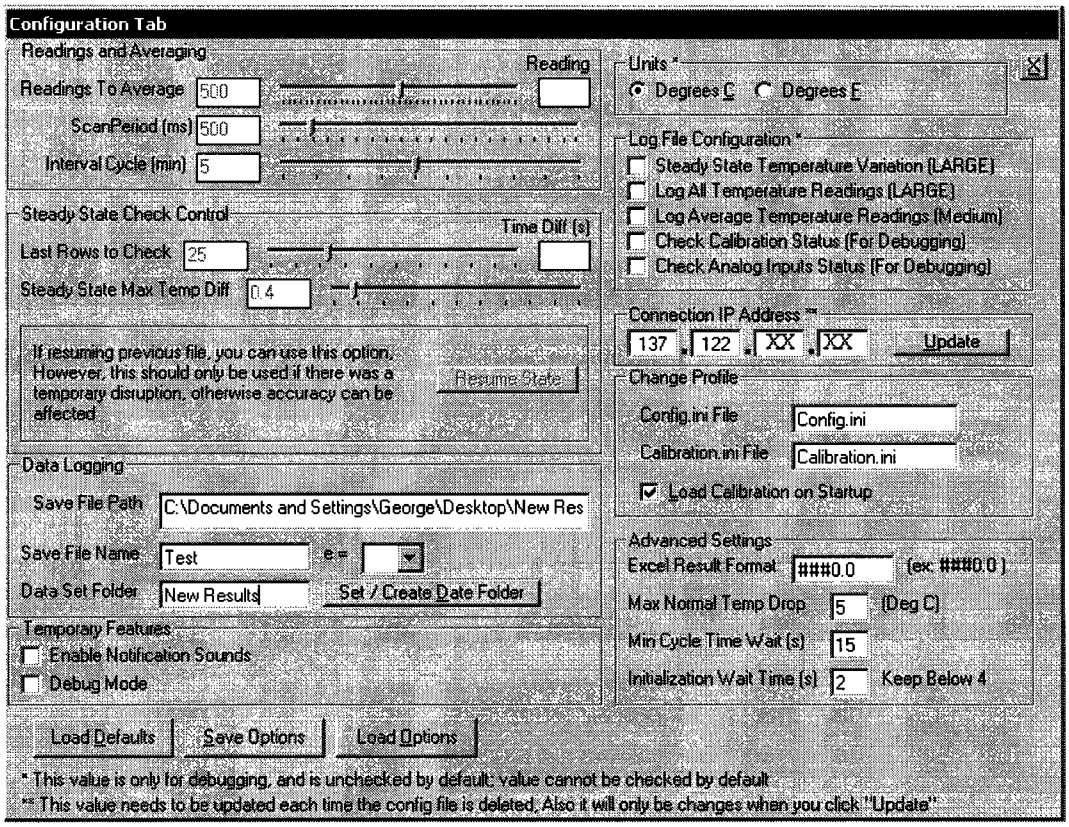

Figure 21 – Data acquisition software configuration page

Additional program features and pages can be seen in Appendix B. This program also automatically performs a large number of calculations and automatically generates useful plots, for example the Nusselt number, Rayleigh number, and Grashof number versus

the eccentricity. It can also calculate the average temperature of the annulus for different values of the eccentricity and the heat flux.

As mentioned previously, the thermocouples used in these experiments were made out of Omega Chromel and Alumel single-strand wires with a diameter of 0.38 mm that were welded together using a thermocouple welder. Omega k-type thermocouple extension wire was also used because this setup required long strands of wire.

3.2.3 Handheld digital thermometer

Figure 22 – Omega digital thermometer with removable probe (Image altered from Omega Inc. promotional data sheet)

A handheld digital thermometer was used to take comparative temperature readings and to help calibrate the thermocouple in the annulus. The digital thermometer used was an

Omega, Model CL3512A calibrator/thermometer. The thermometer was tested using an ice point reference device and a mercury thermometer and was found to be accurate. Some of the manufacturer's specifications are as follows:

- Sampling rate: 1 Hz
- Resolution: 0.1 (to 199.9) or 1 °C
- Measurement uncertainty: ±(0.1% reading + 1°C) in the range -60 to 1372°C (not including thermocouple error)

3.2.4 Particle image velocimetry

Figure 23 – Neodymium YAG double-pulse laser and New Wave Research Solo PIV (Image adapted from the New Wave Research website: www.new-wave.com)

To avoid disturbance of the natural convection in the experimental setup, we needed a non intrusive method of measuring the mass flow rate through the annulus. For this we chose to use particle image velocimetry (PIV). The PIV system used was obtained from

LaVision (Goettingen, Germany) and included a Neodymium: YAG double-pulsed laser, a digital camera, a processor with DaVis 7.2 analysis software, a timing unit and other accessories. The two lasers contained in the housing of the New Wave Research Solo PIV 120XT seen in Figure 23 are directed through the same output and exit the casing following the same path if properly aligned. The laser has a wavelength of 532 nm and produces pulses with energy of up to 120 mJ per pulse. The exit of the housing was fitted with a cylindrical lens having a focal length of -10 mm, which was used to fan the laser beam into a sheet.

The camera used in performing the PIV measurements was a LaVision Imager Pro X 4M, which had a CCD chip size of 2048 × 2048 pixels, a pixel size of 7.4 μm and an image rate of 14 frames/s. The camera was equipped with a Nikon 50 mm, f 1/8 lens and a 532 nm interference filter. This camera has a double-exposure feature with an inter-frame time as low as 100 ns.

3.2.5 Low-Ohm meter

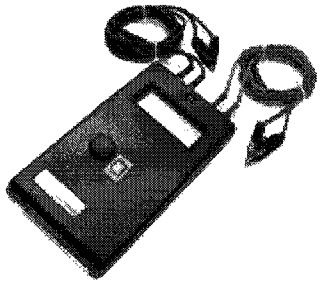

Figure 24 – Isotek M210 milliohmmeter (Image from Isotek website: www.isotekcorp.com)

An Isotek (Swansea, Massachusetts, USA) M210 milliohmmeter, seen in Figure 24, was used to measure the very low resistance in the stainless steel foil. This unit is a hand-

held device which uses a four-terminal network (Kelvin Bridge) in order to eliminate errors caused by the test lead resistance. Some technical specifications of this device have been listed in Table 1 below.

Table 1 – Isotek M210 milliohmmeter specifications (Isotek Corporation, Swansea, Massachusetts, USA)

Range (Selected Automatically)	1.999 Ω, 19.99 Ω , 199.9 Ω
Increments	0.001 Ω, 0.01 Ω, 0.1 Ω
Accuracy	± 0.1 % of range
Zero Offset	± 0.001 Ω
Display	3 -1/2 digit LCD

Chapter 4 Analytical Background

4.1 Buoyancy

All fluid flows require a driving mechanism in order to exist as it is an intrinsic property of fluid flow to dissipate exergy (Bejan, 2004). Without a driving mechanism providing new energy to the flow, it will eventually stop. In natural convection, the driving force is buoyancy caused by a density gradient, which in turn is caused by a temperature gradient.

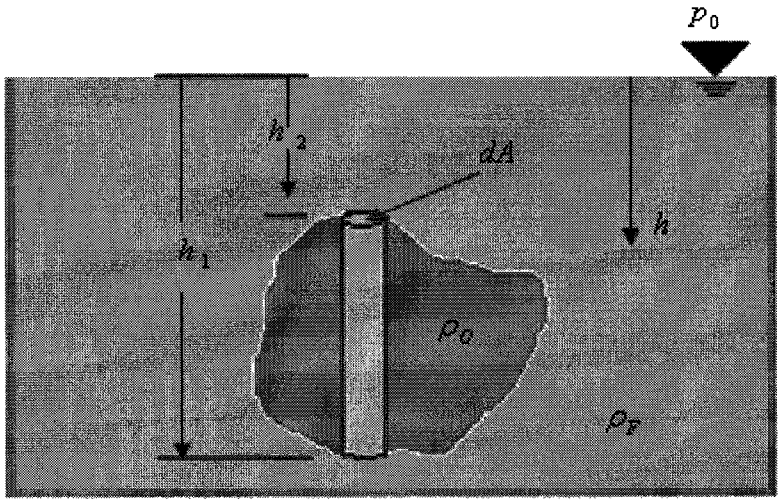

Figure 25 – A body immersed in a fluid

Consider an object of density ρ_O and volume $\forall$ immersed in a fluid of density ρ_F as seen in Figure 25. The buoyancy force is the total vertical force due to hydrostatic pressure acting on the object and is given as

$$F_B = \rho_F g \forall \tag{1}$$

The body force due to gravity acts downwards on the object and equals $F_g = \rho_O g \forall$. Thus the net force acting on the object is

$$F_{net} = F_B - F_g = (\rho_O - \rho_F) g \forall \tag{2}$$

Vertical forces on a mass of fluid of some density that is immersed in a fluid of a different density act in a similar fashion. Density variations could be due to variations in the fluid's composition or to temperature differences.

The change of density of a fluid in response to a change of its temperature at a constant pressure is given by the *volumetric thermal expansion coefficient* (Incropera and DeWitt, 2005)

$$\beta = -\frac{1}{\rho}\left(\frac{\partial \rho}{\partial T}\right)_P \tag{3}$$

For an ideal gas

$$\beta = -\frac{1}{T} \tag{4}$$

4.2 Dependence of air properties on temperature

The change in temperature of the air in the annulus affects its thermodynamic properties. Because we rely on such properties for our calculations, we decided to plot the changes of each property with temperature and fit a polynomial to these data. The temperature range chosen for our plots was between 150 and 500 K. Table 2 shows the values of the thermodynamic properties of air over this range.

Table 2 – Thermodynamic properties of air (Incropera and DeWitt, 2005)

Temperature, T [K]	**Density, ρ** [kg/m^3]	**Specific heat capacity, c_p** [kJ/kg K]	**Thermal conductivity, k** [W/m K]	**Kinematic viscosity, ν** [cm^2/s]	**Prandtl number, Pr** -	**Thermal diffusivity, α** [cm^2/s]
150	2.336	1.012	0.014	0.044	0.758	0.058
200	1.746	1.007	0.019	0.076	0.737	0.103
250	**1.395**	**1.006**	**0.022**	**0.114**	**0.720**	**0.159**
300	**1.161**	**1.007**	**0.026**	**0.159**	**0.708**	**0.225**
350	**0.995**	**1.009**	**0.030**	**0.209**	**0.699**	**0.299**
400	**0.871**	**1.014**	**0.034**	**0.264**	**0.691**	**0.383**
450	0.774	1.021	0.037	0.324	0.686	0.472
500	0.696	1.030	0.041	0.388	0.684	0.567

The variations of air density, specific heat capacity, thermal conductivity, kinematic viscosity, thermal expansion coefficient and thermal diffusivity with temperature within the range of interest have been plotted in Figure 26, 27, 28, 29, 30 and 31, respectively.

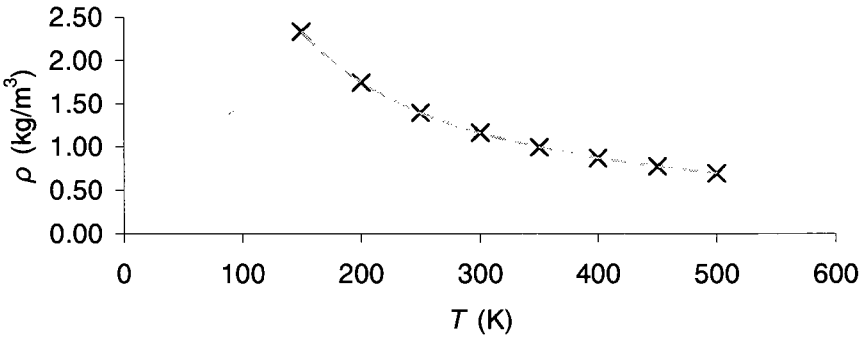

Figure 26 – Density versus temperature for air

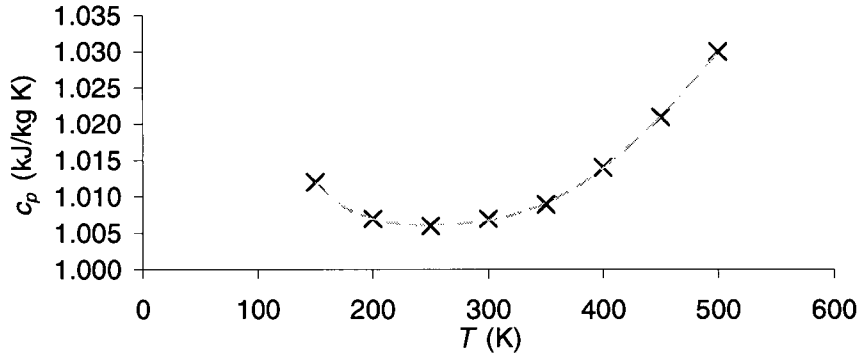

Figure 27 – Specific heat capacity versus temperature for air

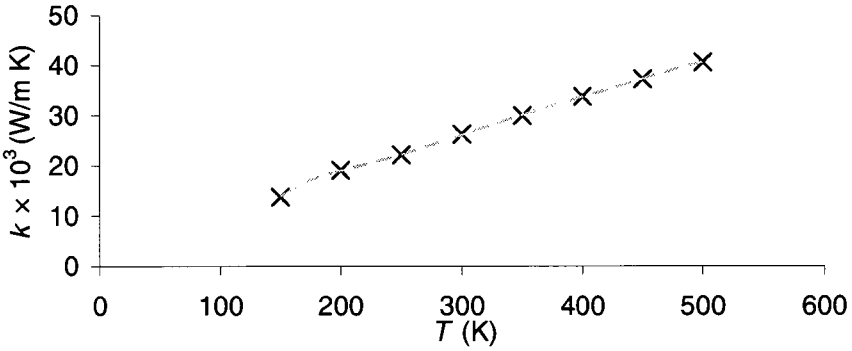

Figure 28 – Thermal conductivity versus temperature for air

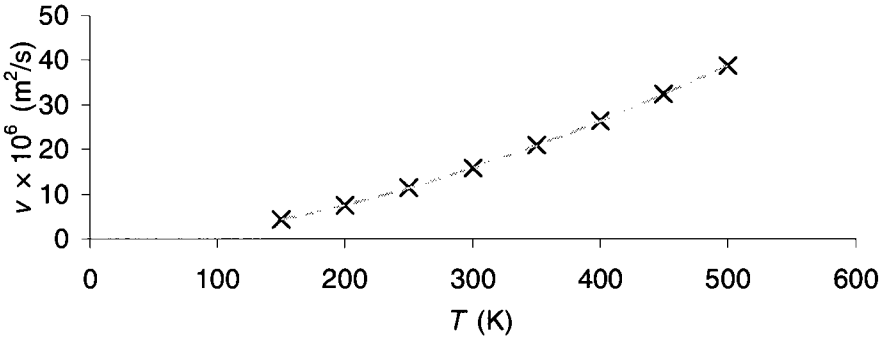

Figure 29 – Kinematic viscosity versus temperature for air

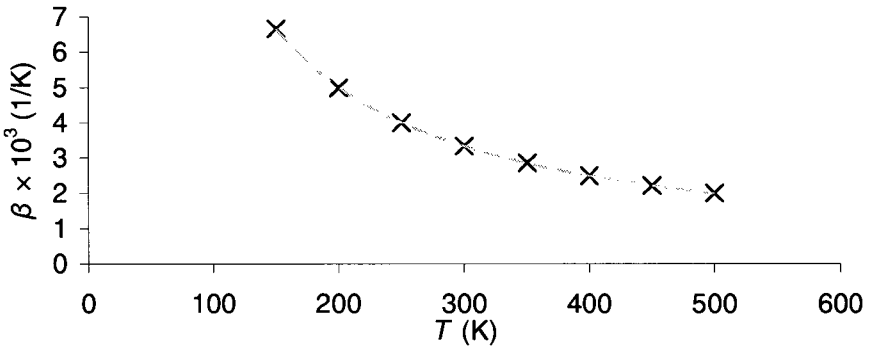

Figure 30 – Thermal expansion coefficient versus temperature for air

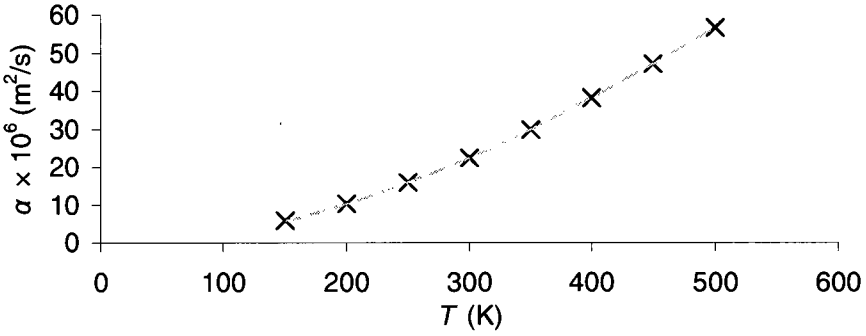

Figure 31 – Thermal diffusivity versus temperature for air

For convenience in calculations, sixth-order polynomial expressions were fitted to these results as follows

$$f(T) = a_6 T^6 + a_5 T^5 + a_4 T^4 + a_3 T^3 + a_2 T^2 + a_1 T^1 + a_0 T^0 \quad (5)$$

The values of the coefficients have been listed in Table 3, in which units match those used in the respective figures presented previously.

Table 3 – Coefficients in the polynomial expression fitted to the thermodynamic properties of air between 150 and 500 K

	Coefficients						
	a_6	a_5	a_4	a_3	a_2	a_1	a_0
ρ	1.9556×10^{-15}	-4.3526×10^{-12}	4.0492×10^{-9}	-2.0374×10^{-6}	5.9762×10^{-4}	-1.0190×10^{-1}	9.3101
c_p	8.8889×10^{-17}	-2.0410×10^{-13}	1.8889×10^{-10}	-8.9903×10^{-8}	2.3545×10^{-5}	-3.2549×10^{-3}	1.1927
k	-2.2222×10^{-13}	4.5631×10^{-10}	-3.8122×10^{-7}	1.6537×10^{-4}	-3.9167×10^{-2}	4.8625	-2.3157×10^{2}
v	-3.7333×10^{-15}	7.3703×10^{-12}	-5.8133×10^{-9}	2.2648×10^{-6}	-3.2668×10^{-4}	6.3287×10^{-2}	-2.9348
β	4.5855×10^{-18}	-1.0399×10^{-14}	9.8765×10^{-12}	-5.0847×10^{-9}	1.5299×10^{-6}	-2.6858×10^{-4}	2.5429×10^{-2}
Pr	3.5556×10^{-17}	-4.7590×10^{-14}	2.4274×10^{-11}	-7.2364×10^{-9}	2.5209×10^{-6}	-9.8270×10^{-4}	8.6427×10^{-1}
α	3.7333×10^{-14}	-7.3703×10^{-11}	5.8800×10^{-8}	-2.4339×10^{-5}	5.7088×10^{-3}	-6.2349×10^{-1}	2.8465×10^{1}

4.3 Heat transfer

4.3.1 Conduction

The rate of heat transferred by conduction between two parallel surfaces with area A, separated by a distance Δz and having a temperature difference ΔT is given by Fourier's law

$$q_z = -kA\left(\frac{\Delta T}{\Delta z}\right) \tag{6}$$

where k is the thermal conductivity of the material. For radial conduction in a tube, as seen in Figure 32, the heat transfer rate is given as

$$q_r = \frac{2\pi kl(T_1 - T_2)}{\ln(r_2 / r_1)} \tag{7}$$

where l is the length of the tube, r_1 is the inner surface radius, r_2 is the outer surface radius, and T_1 and T_2 are the temperatures of the aforementioned surfaces, respectively.

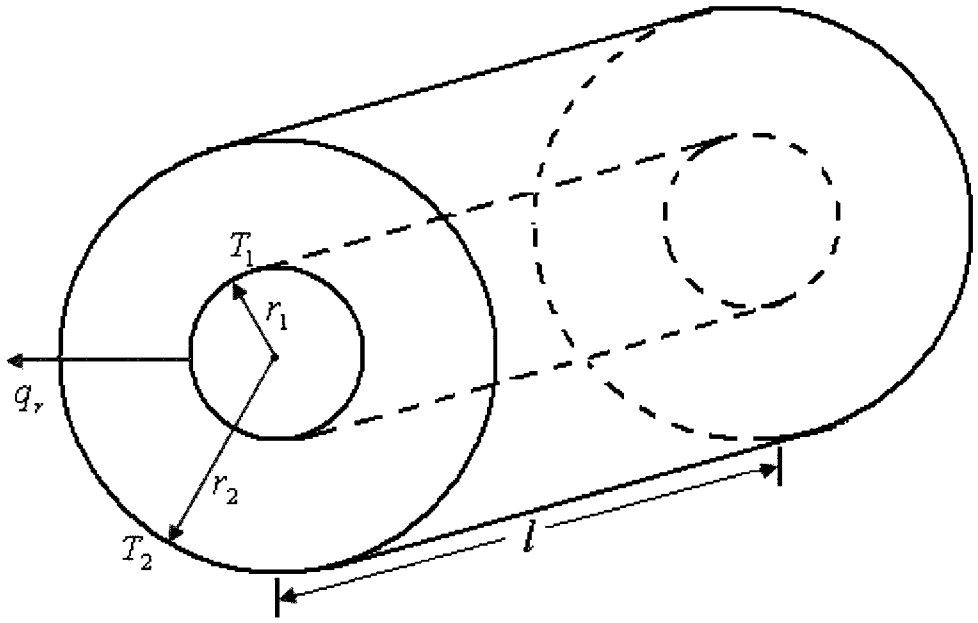

Figure 32 – Radial conduction in a finite tube

4.3.2 Convection

The convective heat transfer rate q from a surface of area A and temperature T_s to a surrounding fluid with temperature T_∞ is given by Newton's law of cooling as

$$q = hA(T_s - T_\infty) \tag{8}$$

where h is the convective heat transfer coefficient. The heat flux can be expressed as

$$q'' = h(T_s - T_\infty) \tag{9}$$

The heat transfer coefficient depends on several factors, including the state of the flow (i.e., whether it is laminar or turbulent), the surface geometry, and the thermodynamic properties (Incropera and DeWitt, 2005). In free convection, the heat transfer coefficient is generally lower than that for forced convection.

The Prandtl number represents the ratio of momentum diffusivity and thermal diffusivity and is defined as

$$\text{Pr} = \frac{c_p \mu}{k} = \frac{\nu}{\alpha} \tag{10}$$

The Nusselt number, a dimensionless group representing the ratio of heat transfer from a surface by convection to that by conduction (Heldman, 2003), is defined as

$$\text{Nu} = \frac{\text{convective heat transfer}}{\text{conductive heat tranfer}} = \frac{h(T_s - T_\infty)}{k(T_s - T_\infty)/l} = \frac{hl}{k} \tag{11}$$

A Nusselt number value of the order of 1 or less corresponds to heat transfer in which conduction dominates. The larger the Nusselt number is, the more significant the convection and the greater the heat transfer are (Heldman, 2003).

Another important non-dimensional number is the Grashof number, which represents the ratio of buoyancy forces to viscous forces and plays the same role in free convection as

the Reynolds number plays in forced convection (Das, 2005). At relatively low Grashof numbers the flow due to natural convection is considered to be laminar, whereas at high Grashof numbers the flow is considered to be turbulent. For a vertical flat plate, the transition Grashof number is between 10^8 and 10^9. For pipe flow, the Grashof number is given as

$$\mathrm{Gr_D} = \frac{\text{buoyancy force}}{\text{viscous force}} = \frac{g\Delta\rho\forall}{\rho\nu^2} = \frac{g\beta\Delta TD^3}{\nu^2} \tag{12}$$

where D is the diameter of the pipe, $\Delta\rho$ is the total change in density between regions of high and low temperature, and ΔT is the difference between these temperatures. In the case of non-circular channels, one can use the hydraulic diameter instead of D.

Finally, another important non-dimensional number is the Rayleigh number, often described as the product of the Grashof number and the Prandtl number. The Rayleigh number provides a criterion for determining whether free convection occurs (Cussler, 1997). The critical Rayleigh number provides the limit for stability in a system; for values lower than the critical value, no free convection would occur, whereas for higher values free convection occurs. Thus the Rayleigh number can be seen as a ratio of buoyancy forces tending to cause flow to other forces tending to resist this flow (Cussler, 1997). The Rayleigh number expressed using a characteristic length D can be written as

$$\mathrm{Ra_D} = \mathrm{Gr_D}\cdot\mathrm{Pr} = \frac{\text{buoyancy force}}{\text{viscous force}}\cdot\frac{\text{viscous diffusion rate}}{\text{thermal diffusion rate}} = \left(\frac{g\beta\Delta TD^3}{\nu^2}\right)\left(\frac{\nu}{\alpha}\right)$$

$$\mathrm{Ra_D} = \frac{g\beta\Delta TD^3}{\alpha\nu} \tag{13}$$

4.3.3 Radiation

Radiative heat transfer is the only form of heat transfer which can occur in a vacuum between two separate surfaces. One theory suggests that the heat is transferred by electromagnetic waves, whereas a more recent theory suggests that the transfer occurs through particles called photons which are emitted by each surface and travel through space. Many factors and complications come into play when looking at the problem of radiative heat transfer. In general, for the majority of applications, conductive and convective heat transfer rates are linearly proportional to temperature differences, while in radiative heat transfer the rates are proportional to the differences in temperatures to the fourth power (Modest, 2003). In the present experiments, radiation from the heated cylinders to the surroundings may be considered as energy loss, whereas radiation from one cylinder to the other is not a loss, as it contributes to the setting of temperature of each surface.

All surfaces emit radiation at all times but the rate of emission depends on the surface properties. A blackbody is a hypothetical surface which is an ideal emitter, emitting the maximum possible radiation power. The total radiation power emitted by a black body Φ_e is given as

$$\Phi_e = \sigma A T^4 \tag{14}$$

where σ is the Stephan-Boltzmann constant. As well, a blackbody can absorb all incoming radiation irrespective of its wavelength or direction. It is important to note that for most

materials the emission and absorption of radiation depends on the wavelength and direction of radiation as well as surface properties.

The *total emissivity* ε of a surface is the ratio of radiation emitted by the surface to that which would be emitted by a blackbody. Emissivity depends on the surface properties of the material and its temperature. As illustrated in Figure 33, unlike that of a blackbody, the emission of radiation from a real surface also depends on the direction at which it is emitted. Additionally, one may define the *monochromatic emissivity* ε_λ, which is a function of each wavelength λ and temperature, as the ratio of the spectral radiance of a surface to the spectral radiance of a black body.

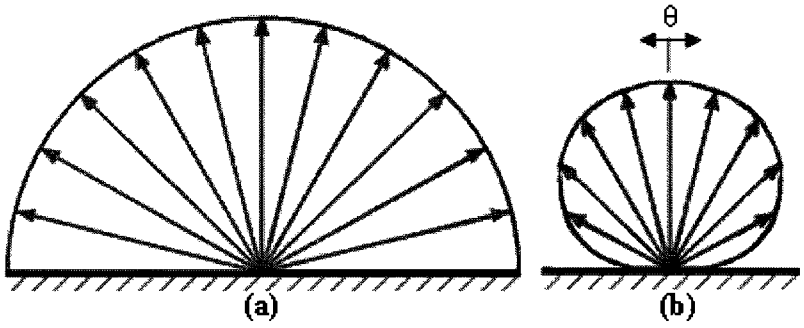

Figure 33 –Directional distribution of surface emission for (a) blackbody, (b) other body

Irradiation is the rate at which radiation is incident on a surface. Incoming radiation is reflected, absorbed, or transmitted through the surface, although for an opaque material, such as stainless steel, transmission is negligible. The total irradiation is the sum of the reflected, absorbed and transmitted irradiations.

The absorptivity of a surface is the ratio of the absorbed irradiation to the total irradiation. Reflectivity is the ratio of reflected irradiation to the total irradiation. The sum of

the absorptivity and reflectivity should be essentially equal to 1 for an opaque surface. The radiosity is the total rate at which radiation leaves a surface. This includes both the emitted and reflected radiation.

The problem of radiation cannot be separated from that of other forms of heat transfer. The net radiation energy emitted and absorbed by a surface depends on the temperature of the surface and that of the surroundings. Therefore, within an enclosure, minimizing the surface temperature differences would minimize the net radiation heat transfer from these surfaces. Of course, bodies are emitting energy through radiation at all times, yet, when what they emit is equal to what they receive, one can ignore the overall transfer of radiation. Unfortunately, even in an ideal enclosure, such as an infinitely long annulus, radiation heat transfer must still be taken into account if temperature differences exist. The radiation heat transfer in this case would affect the local temperature and in doing so also affects the heat transfer taking place by conduction and convection.

Now, let us consider two concentric infinitely long cylinders forming an annulus. The net heat transfer between the two cylinders depends on the amount of radiation being transferred from one to the other, as well as the amount of radiation being transferred from one part of the outer cylinder to another part of it. All radiation emitted from the inner cylinder will be intercepted by the outer cylinder, however, as can be seen in Figure 34, some of the radiation emitted from the outer cylinder will be intercepted by other parts of the outer cylinder itself. As one can expect, changing the position of the inner cylinder would affect the proportion of the radiation emitted by the outer cylinder which impacts on the inner one, which is called the view factor.

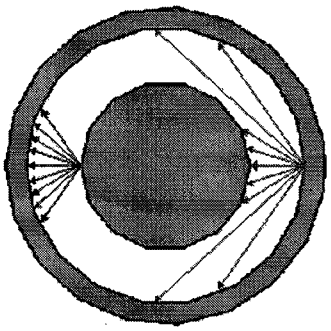

Figure 34 – Radiation leaving the inner and outer cylinders

The view factor between two infinitesimal surface elements dAi and dA_j is given by Modest (2003) as

$$dF_{dAi-dAj} = \frac{\text{diffuse energy leaving } dA_i \text{ directly towards and intercepted by } dA_j}{\text{total diffuse energy leaving } dA_i} \quad (15)$$

Therefore, the view factor $F_{i\text{-}o}$ from the inner cylinder to the outer cylinder would be equal to 1, as all the diffuse energy leaving the inner cylinder is intercepted by the outer cylinder.

From Incropera and DeWitt (2005), we get an expression termed the reciprocity relation as

$$A_i F_{ij} = A_j F_{ji} \quad (16)$$

From this, one can calculate the view factor $F_{o\text{-}i}$ from the outer cylinder to the inner cylinder as

$$F_{o-i} = \frac{A_i}{A_o} F_{i-0} = \frac{\pi D_i l_i}{\pi D_o l_o} F_{i-0} = \frac{D_i}{D_o} \quad (17)$$

Consequently,

$$F_{o-o} = 1 - \frac{D_i}{D_o} \tag{18}$$

and

$$F_{i-i} = 0 \tag{19}$$

For a finite concentric cylindrical annulus of height h, Modest (2003) provides the following relations

$$F_{o-i} = \frac{1}{R}\left(\frac{H^2+R^2-1}{4H} - \frac{1}{\pi}\left\{\cos^{-1}\frac{H^2-R^2+1}{H^2+R^2-1} - \frac{\sqrt{\left(H^2+R^2+1\right)^2-4R^2}}{2H}\cos^{-1}\frac{H^2-R^2+1}{R\left(H^2+R^2-1\right)} - \frac{H^2-R^2+1}{2H}\sin^{-1}\frac{1}{R}\right\}\right) \tag{20}$$

$$F_{o-o} = 1 - \frac{1}{R} - \frac{\sqrt{H^2+4R^2}-H}{4R} + \frac{1}{\pi}\left(\frac{2}{R}\tan^{-1}\frac{2\sqrt{R^2-1}}{H} - \frac{\mathrm{H}}{2\mathrm{R}}\left\{\frac{\sqrt{4R^2+H^2}}{H}\sin^{-1}\frac{H^2+4\left(R^2-1\right)-2H^2/R^2}{H^2+4\left(R^2-1\right)} - \sin^{-1}\frac{R^2-2}{R^2}\right\}\right) \tag{21}$$

in which

$$R = r_o/r_i \qquad H = h/r_i$$

In general, if two surfaces only exchange radiation with each other, then the net rate of radiation transfer from the first surface must equal the net rate of radiation transfer to the second, thus

$$q_{i-o} = q_i = -q_o \tag{22}$$

The network representation of the radiative exchange between the two surfaces can be seen in Figure 35, in which J is the radiosity and ε is the emissivity.

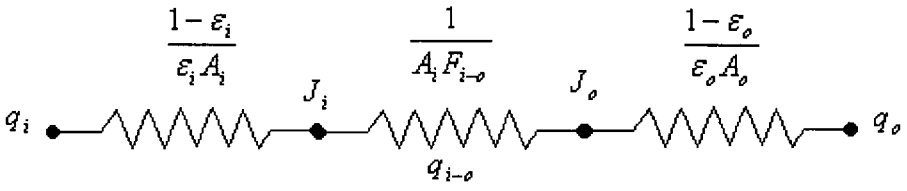

Figure 35 – Network representation of radiation heat transfer in a two-surface enclosure

The net radiation exchange between the two surfaces can be expressed as

$$q_{i-o} = q_i = -q_o = \frac{\sigma\left(T_i^4 - T_o^4\right)}{\frac{1-\varepsilon_i}{\varepsilon_i A_i} + \frac{1}{F_{i-o} A_i} + \frac{1-\varepsilon_o}{\varepsilon_o A_o}} \tag{23}$$

In an enclosure between two infinitely long coaxial cylinders, the net radiation exchange between the two surfaces is given in Incropera and DeWitt (2005) as

$$q_{i-o} = \frac{\sigma A_i\left(T_i^4 - T_o^4\right)}{\frac{1}{\varepsilon_i} + \frac{1-\varepsilon_o}{\varepsilon_o}\left(\frac{r_i}{r_o}\right)} \tag{24}$$

4.4 Joule heating

Electrical resistance is a measure of a material's opposition to the flow of an electrical current through it. As electrons flow through a path in the form of current, friction results from the resistance to this flow and this friction manifests itself in the form of heat.

Resistance or Joule (also referred to as ohmic) heating is the rate at which energy is generated as current passes through a material that has an electrical resistance (Incropera and DeWitt, 2005). This rate (i.e., power) can be determined as

$$q = I^2 R \tag{25}$$

for which I is the current, and R is the electrical resistance.

If current flows uniformly through a material with a uniform electrical resistance and a uniform cross-sectional area, then the rate of heat generated by this material should also be uniform along its length.

The electrical resistance of a material is primarily a function of its length l electrical resistivity ρ (sometimes referred to as specific electrical resistance), and cross-sectional area A as

$$R = \frac{\rho l}{A} \tag{26}$$

Electrical resistance can also be related to voltage E and current through Ohm's law

$$R = \frac{E}{I} \tag{27}$$

Therefore, for a material with a rectangular cross-section through which a constant current passes, the heat flux is a function of the material's resistivity, width and thickness and the current that passes through it, as

$$q'' = \frac{q}{A} = \frac{1}{A}\left[I^2 \frac{\rho l}{A_c} \right] = \frac{1}{w \times l} \times I^2 \frac{\rho l}{t \times w} = \frac{I^2 \rho}{w^2 \times t} \tag{28}$$

The resistivity is determined by the scattering of electrons, which is primarily due to the thermal motion of atoms; the higher the scattering is, the higher the resistivity of the material will be. For the range of temperatures we will encounter, the increase of electrical resistivity with temperature can be considered as being linear and given in terms of the *temperature coefficient of resistance* α, a reference resistivity ρ_0 and the temperature difference as

$$\rho = \rho_0 [1 + \alpha (T - T_0)] \tag{29}$$

This expression can also be written in terms of electrical resistance as

$$R = R_0 [1 + \alpha (T - T_0)] \tag{30}$$

Chapter 5 Measurement Procedures

5.1 Definitions

A sketch of the annular channel can be seen in Figure 36. In this thesis, the term *outer cylinder* will be used to identify the inner surface of the cavity which surrounds the core of the annulus and the term *inner cylinder* will identify the outer surface of the cylindrical core of the annulus. We will designate the vertical axis as the z-axis, the horizontal path of travel of the inner cylinder as the x-axis and the horizontal axis normal to the x-axis as the y-axis. The origin of coordinates would be on the inlet plane and on the outer cylinder axis. The distance between the axes of the two cylinders will be designated as Δx_i. The radii of the outer and inner cylinders will be designated as r_o and r_i, respectively. The corresponding diameters are D_o = 83 mm and D_i = 51 mm. The heights of the outer and inner cylinders were slightly different; the corresponding symbols and lengths are H_o = 1510 mm and H_i = 1501 mm. The cross-sectional area of the annulus may be calculated as

$$A_a = \pi(r_o^2 - r_i^2) \tag{31}$$

The eccentricity of the annulus is defined as

$$e = \frac{\Delta x_i}{r_o - r_i} \tag{32}$$

such that it is equal to 0 when the two cylinders are coaxial and equal to 1 when the two cylinders are in contact.

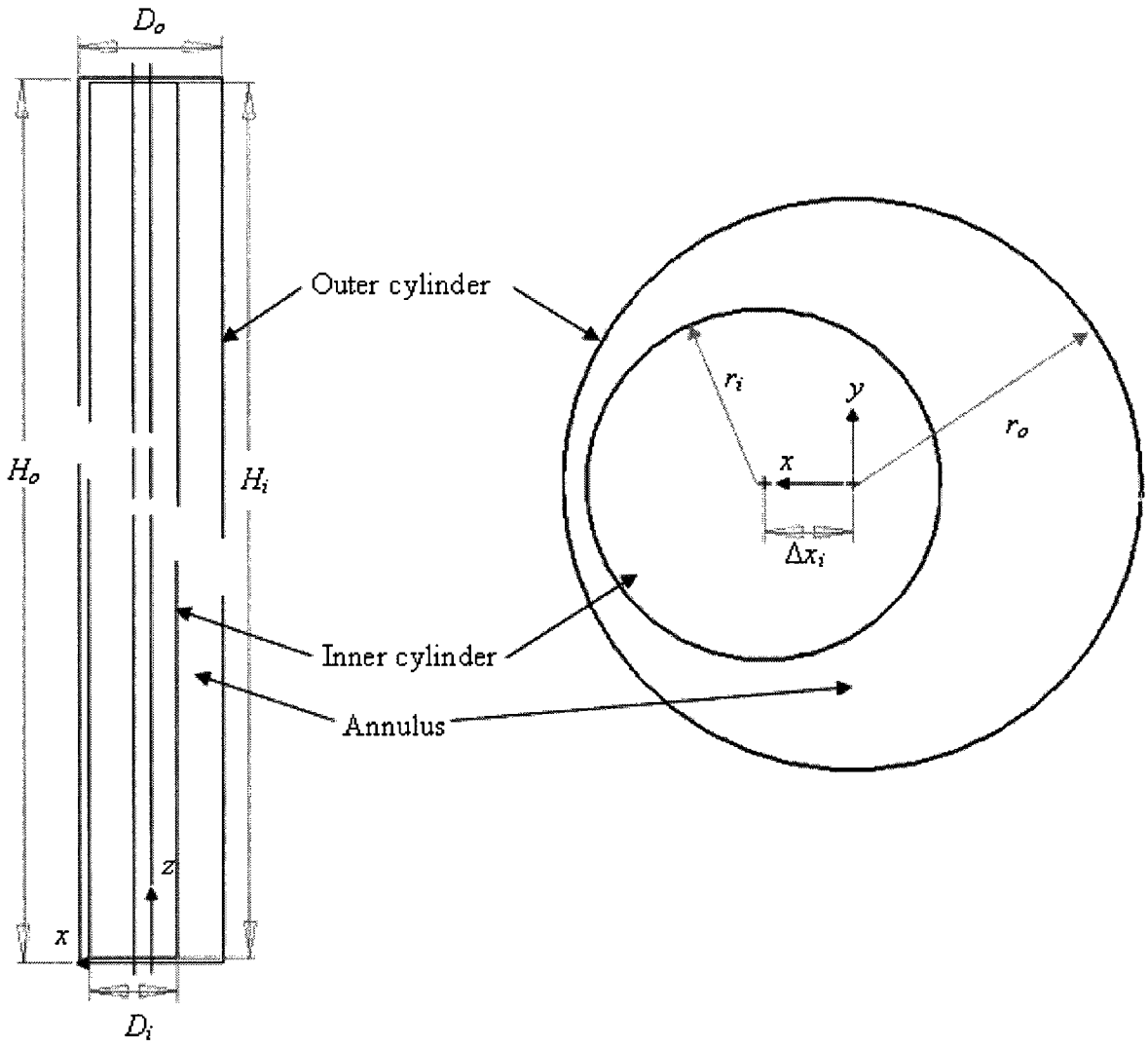

Figure 36 – Sketch of the annular test section with definitions of the dimensions and the coordinate system.

5.2 Resistivity measurement

The foil was made of stainless steel 304 and had a thickness of 50.8 μm. Its resistivity was measured by two methods: first, using a low-ohm meter at room temperature as will be discussed in section 5.2.1 and second by passing a current through the foil and calculating the resistance from Ohm's law as will be discussed in section 5.2.2.

5.2.1 Resistivity at room temperature

A strip of the stainless steel foil was cut to a length of just over 1.6 m and a width of 256 mm. The leads of a low-ohm meter were then connected at the ends of the foil and the resistance of the foil piece was measured. Placing the leads of the low-ohm meter directly on the stainless steel foil gave varying results depending on their position width-wise. This was attributed to the change in the path the electrical current takes. For this reason, copper plates were used at the ends in order to more evenly distribute the current passing through the foil. The foil was folded in half and at each end a 1.58 mm thick copper plate was sandwiched such that the length of stainless steel which did not come into contact with the copper was 1.601 m. Heavy weights were placed at either end as can be seen in Figure 37 to minimize the contact resistance between the copper plates and the foil. The metal weights were electrically insulated from the foil. We assumed that the resistance of the copper plates as well as the contact resistance between the copper and the stainless steel were negligible.

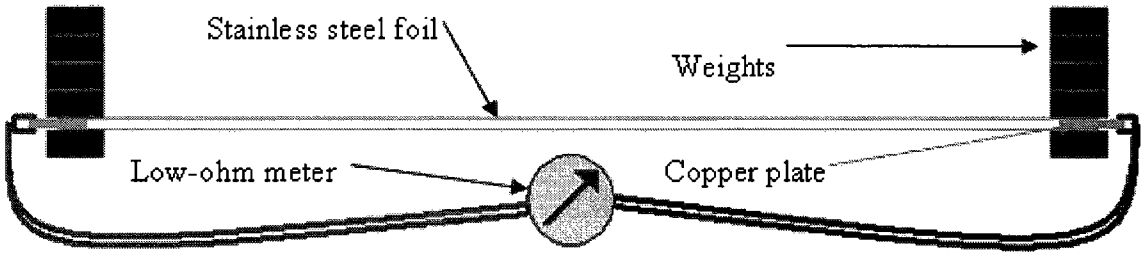

Figure 37 – Resistance measuring setup using a low-ohm meter

It was noticed that even though the contact surfaces of the copper and stainless steel were properly cleaned, not applying enough force to these surfaces resulted in varying readings. For this reason we kept on adding weights until the readings were consistent. The measured resistance was found to be 0.094 Ω and applying equation 26 at the room temperature of 296.5 K we calculated the resistivity to be $\rho = RA/l = 7.67\times10^{-7}\ \Omega\, m$.

5.2.2 Temperature dependence of resistivity

The stainless steel resistivity as well as its temperature dependence was measured by running a constant current through the inner and outer cylinders of the assembled apparatus. The stainless steel wall temperature was measured using the array of embedded thermocouples discussed in section 3.1 and the average temperature was calculated using the method which will be discussed in section 5.4. The voltage and the current were measured using the power supply sensor monitoring setup discussed in section 3.2.1. The resistivity was calculated from the current I, voltage E, cross-sectional area A and length l of the foil as

$$\rho = \left(\frac{E}{I}\right)\frac{A}{l} \tag{32}$$

This process was repeated for a few values of the applied voltage while keeping the current constant and the corresponding values of the resistivity were plotted vs. temperature. Then,

the temperature coefficient of resistivity at the reference temperature T_0 (taken to be the temperature at the start of the experiment) was estimated from the slope of a linear fit to the measurements as

$$\alpha_0 = \frac{1}{\rho_0}\frac{\Delta\rho}{\Delta T} \tag{33}$$

where ρ_0 is the reference resistance at the reference temperature.

In the following plots, we will non-dimensionalize the temperature using the minimum and maximum calculated average temperatures $\overline{T}_{\min}$ and $\overline{T}_{\max}$ of the foil during a given experiment as

$$\overline{T}^{\dagger} = \frac{\overline{T} - \overline{T}_{\min}}{\overline{T}_{\max} - \overline{T}_{\min}} \tag{34}$$

The current and the voltage drop across the cylinders will be non-dimensionalized by using the corresponding reference values I_0 and E_0 at room temperature and the maximum values I_{max} and E_{max} during the experiment as

$$I^* = \frac{I - I_0}{I_{\max} - I_0} \tag{35}$$

$$E^* = \frac{E - E_0}{E_{\max} - E_0} \tag{36}$$

Figure 38 shows that the current through each of the cylinders remained approximately constant over time following the application of power to the foils. Figure 39

shows that both the voltages and the average temperatures of both cylinders increased with time, which also demonstrates that the resistivity changes with temperature. The reference (room) temperature was 295 K, the reference currents for the inner and the outer cylinders were 15.6 A and 26. 7 A, respectively, and the reference voltage was 2.24 V for both.

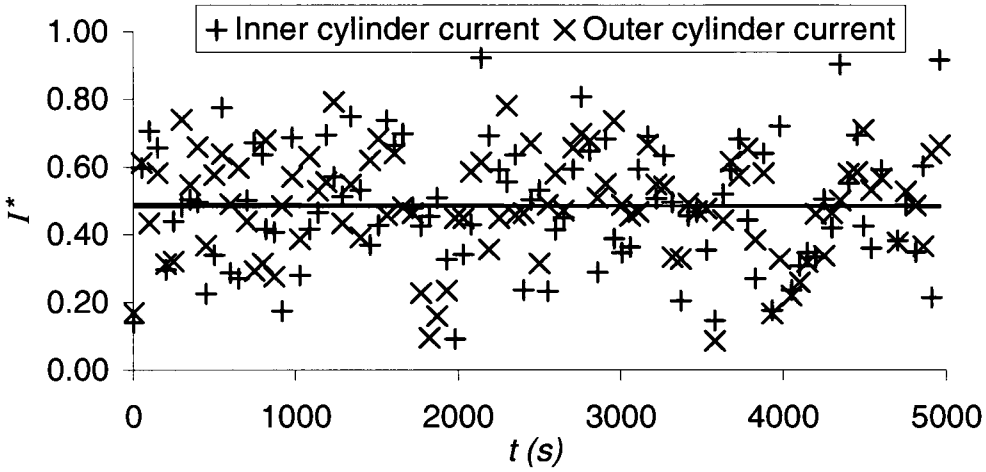

Figure 38 – Variation of currents through the inner and outer cylinders with time; reference current values at 295 K are 15.6 A for the inner cylinder and 26.7 A for the outer cylinder; the maximum current values are 15.7 A and 26.8 A respectively

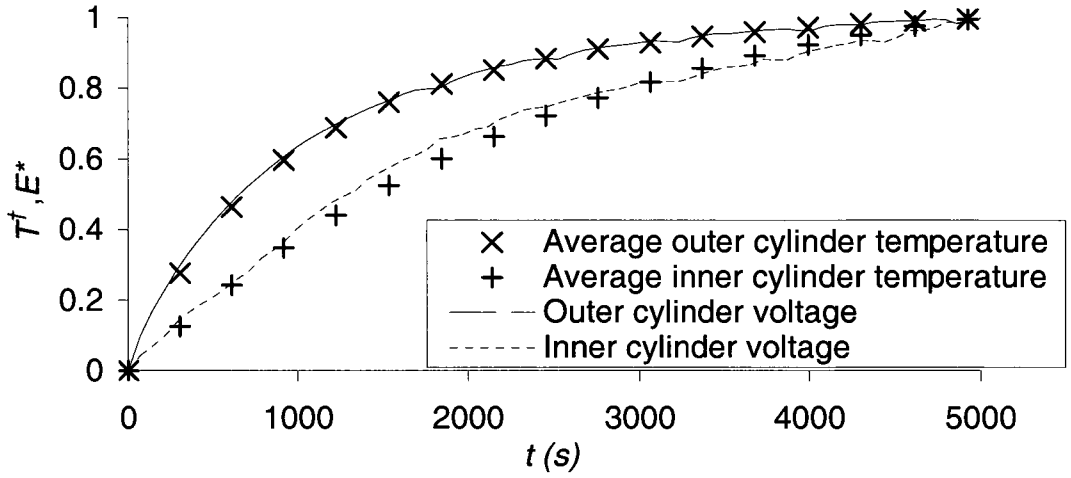

Figure 39 – Temperature and voltage variations with time; for both inner and outer cylinders, $\overline{T}_{\min}$ = 295 K, E_0 = 2.2 V and $E_{\max}$ = 2.3 V; for the outer cylinder $\overline{T}_{\max}$ = 332 K and for the inner cylinder $\overline{T}_{\max}$ = 327 K

The resistances of the foil in the outer and inner cylinders at room temperature were 84 mΩ and 144 mΩ, respectively. The corresponding values of the resistivity of the foil in the outer and inner cylinders at room temperature were 7.3×10^{-7} Ω·m and 7.8×10^{-7} Ω·m, respectively. For comparison, several sources, for example Khatak and Raj (2002), give the electrical resistivity of stainless steel 304 as 7.2×10^{-7} Ω·m at 293 K. The measured resistivity of the foil has been plotted in Figure 40 as a function of the increasing temperature. In this plot, the resistivity is non-dimensionalized by its value ρ_0 at room temperature and the maximum measured value $\rho_{\max}$ as

$$\rho^* = \frac{\rho - \rho_0}{\rho_{\max} - \rho_0} \tag{37}$$

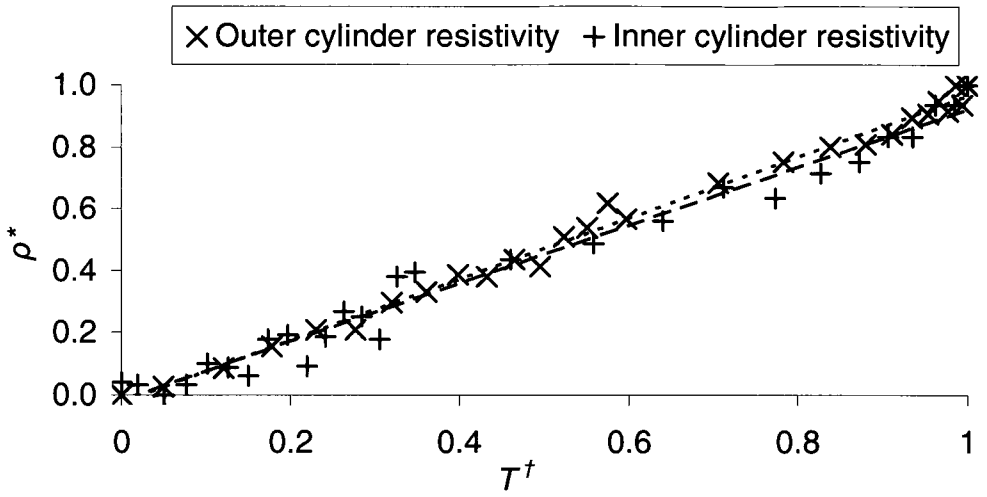

Figure 40 – Variation of resistivity of the stainless steel foil with temperature; for both cylinders $T_{min} = 295$ K, while for the outer cylinder $\overline{T}_{max} = 332$ K, $\rho_0 = 7.34 \times 10^{-7}$ Ω·m and $\rho_{max} = 7.65 \times 10^{-7}$ Ω·m and for the inner cylinder $\overline{T}_{max} = 327$ K, $\rho_0 = 7.78 \times 10^{-7}$ Ω·m and $\rho_{max} = 8.05 \times 10^{-7}$ Ω·m

The temperature coefficients of resistivity of the stainless steel foil in the inner and outer cylinders at 293 K were 1.0×10^{-3} K^{-1} and 1.1×10^{-3} K^{-1}, respectively. Khatak and Raj (2002) cite a value of 1.0×10^{-3} K^{-1} for temperatures ranging between 195 K and 473 K[4]. One should note that the stainless steel foils used for the inner and outer cylinders were purchased at different times.

[4] The temperature coefficient of resistivity is temperature dependent. Providing a single value for this coefficient over such a large range of temperatures is not appropriate. Unfortunately it was difficult to find other sources for the temperature coefficient of resistivity of stainless steel 304. Over the range from 195 to 473 K , the temperature coefficient of resistivity varies by 2.4×10^{-4} K^{-1}

5.3 Heat flux measurement

The heat flux was calculated by two methods, both of which require the knowledge of the current passing through the system. The first method depends on voltage measurements while the second depends on the measurement of the average annulus wall temperature. The only disadvantage of using the voltage measurements directly in order to calculate the heat flux is the need to synchronize the data recorded from the power supply with the data obtained from the temperature measurements. The fact that the datum from the power supply and those from the thermocouples are collected on two different computers makes synchronisation time consuming. Alternatively, as we have calculated the resistivity of the walls of the annulus, as well as the temperature dependence on resistivity, we could, knowing only the current and the wall temperature, calculate the voltage drop. This makes matters much simpler, especially if we consider that the current was constant.

First, the heat flux on the surface of the inner and outer cylinders was calculated from the voltage drops across and the currents flowing through the inner and outer cylinders as

$$q_i'' = \frac{I_i E_i}{A_i} \qquad \text{for the inner cylinder} \tag{38}$$

$$q_o'' = \frac{I_o E_o}{A_o} \qquad \text{for the outer cylinder} \tag{39}$$

Because the outer cylinder was insulated well around its exterior, heat losses from that side were neglected.

Let us consider a control volume in the annulus bounded by two horizontal planes on which thermocouples were installed. The current passing through the stainless steel walls of the annulus generates a heat flux which varies with wall temperature, as described in section 4.4. However, in this control volume, the variation in the wall temperature is small and heat flux variation can be neglected. Figure 41 illustrates the heat flux from the annulus walls in the control volume as well as the flow of air into and out of the annulus.

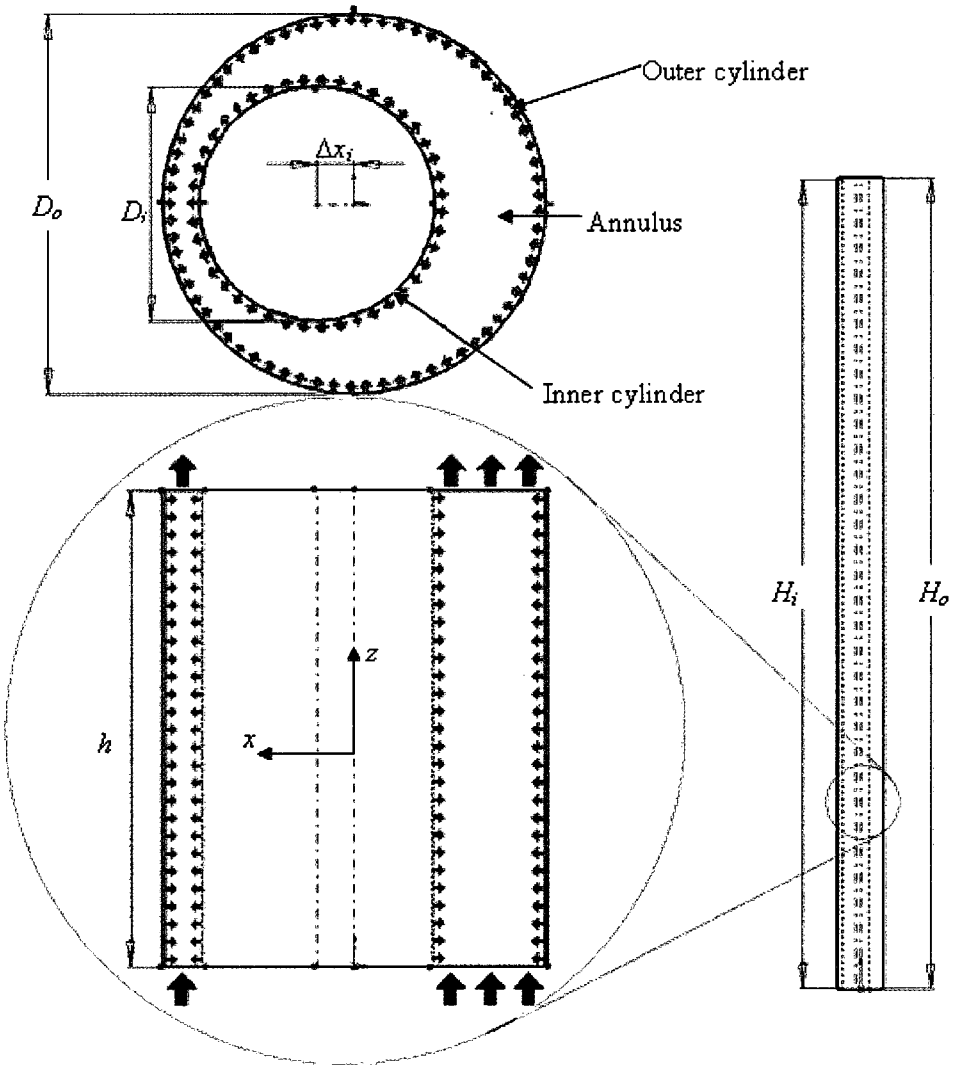

Figure 41 – Control volume of interest, with height h equal to 10 cm, illustrating the wall heat flux (red arrows) and the flow of air into and out of this control volume (blue arrows)

The total heat power Q_{cv} generated in the control volume can be calculated from Joule's law as

$$Q_{cv} = I_o^2 R_o + I_i^2 R_i \tag{40}$$

where R_o and R_i are the electrical resistances of the stainless steel foil of the inner and outer cylinders in the control volume. Each resistance is calculated from the average wall temperatures $\overline{T}$ of the inner and outer cylinders as

$$R_i = \frac{\rho_0 \left[1 + \alpha_0 \left(\overline{T}_i - T_0\right)\right] l}{A_i} \tag{41}$$

$$R_o = \frac{\rho_0 \left[1 + \alpha_0 \left(\overline{T}_o - T_0\right)\right] l}{A_o} \tag{42}$$

Therefore, the heat fluxes in the control volume for the inner and outer cylinders can be determined as

$$q_i'' = \frac{I_i^2 R_i}{A_i} \tag{43}$$

$$q_o'' = \frac{I_o^2 R_o}{A_o} \tag{44}$$

Because temperature directly affects the resistivity of the stainless steel foil, the heat flux would not be uniform along the entire length of the annulus unless its wall temperature were also constant, which is not the case. Throughout our experimental runs, the highest

variation in heat flux due to temperature differences at any given time for the entire length of the annulus was estimated to be less than 5%.

An attempt was made to automatically adjust the values of voltage and current in order to keep a constant average heat flux irrespective of the annulus wall temperature. Unfortunately, the remotely programmable voltage and current resolutions for the power supply were not high enough for this to be possible. As a result, the smallest possible adjustments to the voltage or the current led to an overshoot or undershoot of the desired heat flux. In conclusion, it would be more suitable to say that we have a constant current, rather than a constant heat flux, condition. Nevertheless, the heat flux variation was sufficiently small to meet the objective of this work, which was to investigate the effects of eccentricity for an approximately constant wall heat flux.

5.4 Temperature measurement

5.4.1 Thermocouple calibration

Temperature readings were taken for each thermocouple within the annulus and plotted against the distance from the inlet of the annulus. Readings from each thermocouple were recorded approximately every 5 minutes over a 15 hour period. During this time, the room temperature (more specifically, the temperature at the inlet of the annulus) varied by only 0.4 K. Using the hand-held thermocouple reader, the temperatures at the inlet and the outlet of the annulus were recorded while no power was applied to the foil and it was noticed that the temperature at the exit was 0.5 K higher than that at the inlet; this was attributed to thermal stratification in the room. The readings of the handheld digital thermometer were

found to match those of a mercury thermometer and also were in agreement with the zero value of a thermoelectric ice point reference device.

In order to determine corrections for possible offsets of the thermocouples, it was assumed that the temperature in the unheated annulus varied linearly from the inlet value to the outlet value. As can be seen in Figure 42, all the thermocouple readings were lower than values determined from measurements by the hand held device by amounts varying between approximately 0.5 and 2 K. In this figure, the plotted temperature difference is

$$T^{\ddagger} = T - T_0 \tag{45}$$

where the reference temperature at the inlet of the annulus was, on the average, $T_0 = 295.3$ K. Figure 42 was generated by averaging 230 recorded readings over a 15 hour period. Each recorded reading itself is the average of 500 individual readings taken approximately 0.5 seconds apart from each other.

The reading of each thermocouple was offset by an appropriate value so that the corrected readings essentially collapsed on the assumed linear temperature relationship along the tube. This correction also takes into account any possible offsets of the data acquisition system.

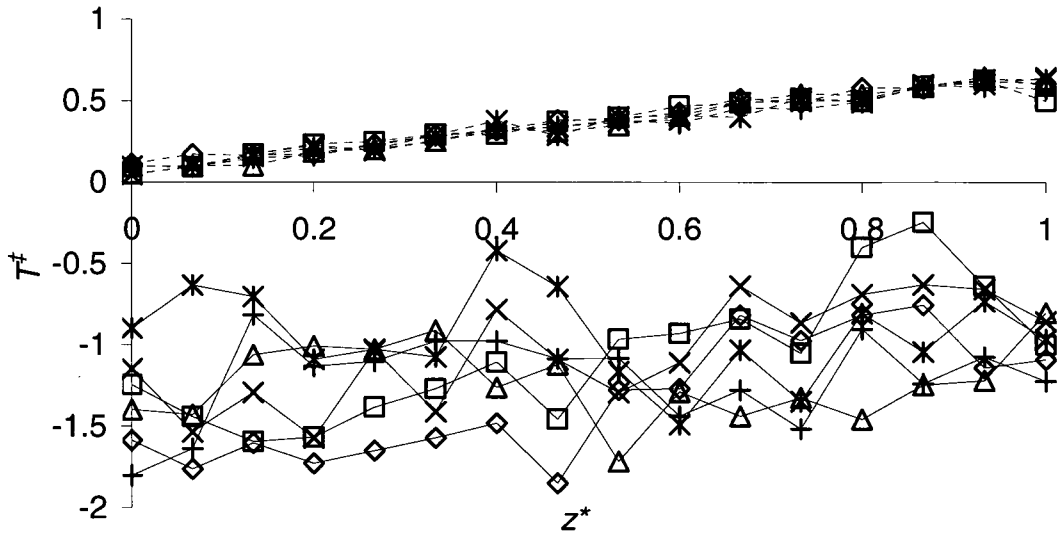

Figure 42 – Temperatures measured by the thermocouples in the unheated annulus versus distance from the inlet; △ = Inner 1, □ = Inner 2, ◇ = Inner 3, + = Outer 1, ✳ = Outer 2 and × = Outer 3; solid lines represent the uncorrected measurements, whereas dashed lines represent the corrected ones

5.4.2 Annulus wall temperature averaging

When electric power is applied to the stainless steel foil, its temperature begins to increase at a relatively slow rate until it eventually reaches a plateau, typically within four hours of any considerable change in the power input or eccentricity. When the temperature levels off, we assume that a *steady state* has been reached. Nevertheless, because the room temperature fluctuates throughout the day, an exact steady state is impossible to attain. For convenience, we consider that a steady state has been reached if, within two hours, no recorded thermocouple reading varies by more than 0.5 K. Each recorded thermocouple reading is the average of 500 individual samples over approximately 5 minutes.

Typically we start each experiment with a concentric annulus and the current adjusted such that the heat fluxes of both cylinders are the same. We then keep the current constant and vary the eccentricity after we are satisfied that a steady state has been reached. Throughout each run, temperature readings from all the thermocouples within the annulus as well as the temperature of the air entering the annulus are recorded.

The average annulus wall temperature is calculated in two parts, the inner cylinder wall temperature and the outer cylinder wall temperature. As we move up the annulus, the wall temperature increases except at the top where we notice a drop in temperature due to radiation losses and possibly other end effects. At each designated height, at 10 cm intervals, we have three thermocouples placed 90° apart on both the inner and the outer cylinder, as seen in Figure 43.

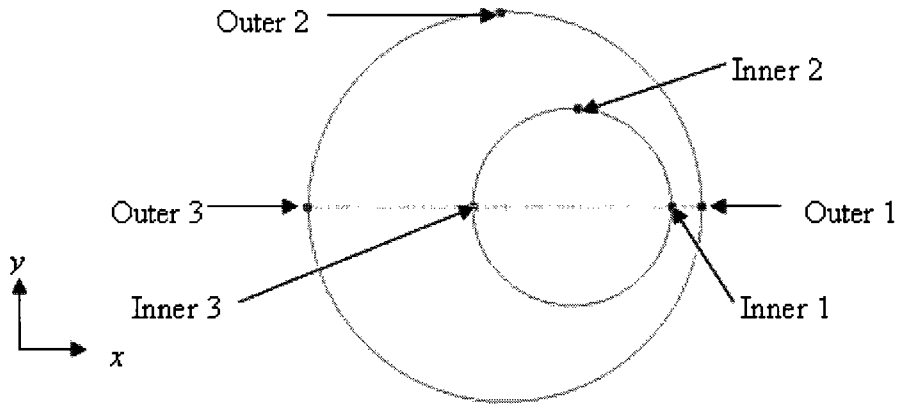

Figure 43 – Thermocouple locations and labels on a cross section of the annulus

The values of the eccentricity considered in these experiments are 0, 0.1, 0.3, 0.5, 0.7, 0.8 and 0.9. Figure 44 shows temperature readings for two heat fluxes, 30 and 80 W/m^2, and an eccentricity of 0.5.

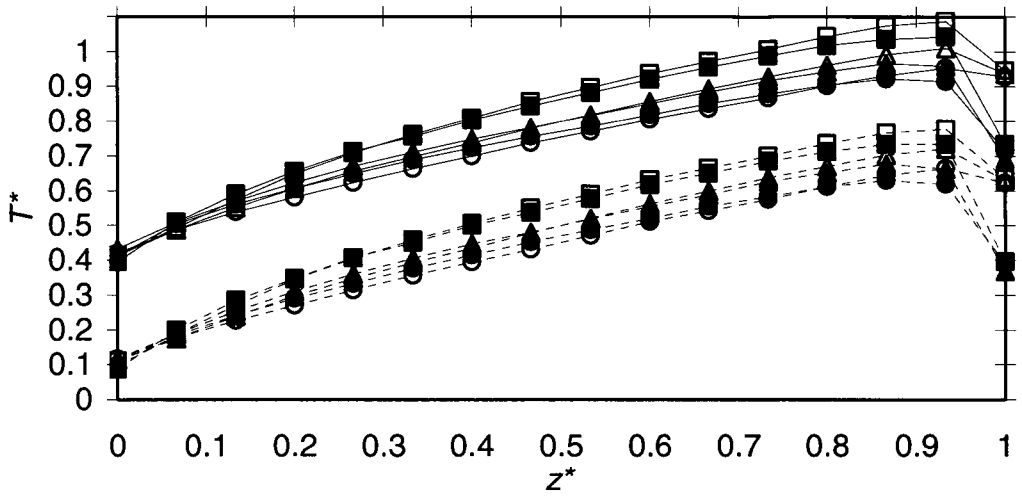

Figure 44 – Temperature versus height along the annulus for $e = 0.5$; □, △, and ○ represent positions 1, 2, and 3 of the inner cylinder, respectively, while matching solid symbols are for the outer cylinder; dashed lines correspond to $q'' = 30$ W/m^2 and solid ones to $q'' = 80$ W/m^2 (the latter results have been shifted upwards by 0.3; all results are normalized by the inlet temperature and the mid temperature at position 2 for each cylinder

A typical set of time-average temperatures at all measured locations in the annulus is presented in Table 4.

Table 4 – Time-averaged temperatures (in K) for $e = 0.5$ and $q'' = 80$ W/m^2

	Outer cylinder															
Location	**0**	**1**	**2**	**3**	**4**	**5**	**6**	**7**	**8**	**9**	**10**	**11**	**12**	**13**	**14**	**15**
Outer 1	303	310	314	318	321	323	326	328	330	332	334	336	337	339	339	322
Outer 2	306	310	313	316	318	321	323	324	326	328	330	332	333	335	334	320
Outer 3	305	309	313	315	317	320	322	323	325	327	329	330	332	332	332	321
	Inner cylinder															
Location	**0**	**1**	**2**	**3**	**4**	**5**	**6**	**7**	**8**	**9**	**10**	**11**	**12**	**13**	**14**	**15**
Inner 1	305	309	313	318	321	324	327	329	331	334	336	338	340	341	342	334
Inner 2	304	309	312	315	318	320	322	325	327	329	331	333	335	337	338	**334**
Inner 3	305	308	311	314	**317**	318	320	322	324	326	328	330	332	333	335	333

Two of the 96 thermocouples (Inner [3, 4] and Inner [2, 15]) were found to have electrical contact with the stainless steel foil, so these were disconnected from the data acquisition system and the vacated channels were used to measure room temperature. The missing temperature values were replaced by averages of neighbouring readings: for the first one, the readings of Inner [3, 3] and Inner [3, 5] were averaged, whereas for the second one the average Inner [1, 15] and Inner [3, 15] were used.

To estimate an azimuthally averaged temperature along the circumferences of each of the two cylinders in the annulus at any given horizontal plane, we have assumed that the circumferential temperature variation would have a minimum at the location of maximum spacing between the two cylinders and a maximum at the minimum gap location as well as matching the values measured by the three thermocouples at that station. Figure 45 shows a typical azimuthal variation of the non-dimensionalized temperature.

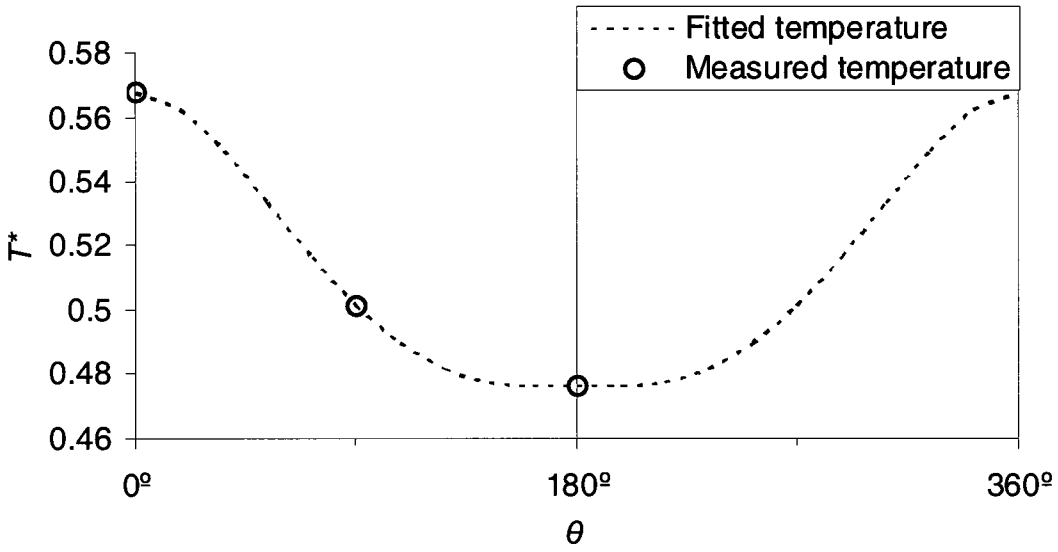

Figure 45 – Plot of temperature T^* versus azimuthal angle θ at a height of 0.8 m for the outer cylinder with $e = 0.5$ and $q'' = 80$ W/m^2

The fourth-order polynomial

$$T = a_4\theta^4 + a_3\theta^3 + a_2\theta^2 + a_1\theta + a_0 \tag{46}$$

is the lowest-order polynomial which can pass through three points and have extrema at two given locations. Its coefficients were determined by satisfying the following five conditions.

1. At $\theta = 0$ (narrowest gap) the temperature is maximum

$$\left.\frac{\partial T}{\partial \theta}\right|_{\theta=0} = 4a_4 0^3 + 3a_3 0^2 + 2a_2 0 + a_1 = 0 \quad \Rightarrow a_1 = 0$$

2. At $\theta = \pi$, the temperature is minimum

$$\left.\frac{\partial T}{\partial \theta}\right|_{\theta=\pi} = 4a_4\pi^3 + 3a_3\pi^2 + 2a_2\pi + a_1 = 0$$

and at the three thermocouple locations, located at 0°, 90° and 180°,

3. $T(0) = a_4 0^4 + a_3 0^3 + a_2 0^2 + a_1 0 + a_0 \qquad \Rightarrow a_0 = T(0)$

4. $T\left(\frac{\pi}{2}\right) = a_4\left(\frac{\pi}{2}\right)^4 + a_3\left(\frac{\pi}{2}\right)^3 + a_2\left(\frac{\pi}{2}\right)^2 + a_1\left(\frac{\pi}{2}\right) + a_0$

5. $T(\pi) = a_4\pi^4 + a_3\pi^3 + a_2\pi^2 + a_1\pi + a_0$

The remaining coefficients can be found by solving a system of three linear algebraic equations.

The azimuthally averaged temperature for each of the two cylinders and on each horizontal plane was computed by integrating the fitted polynomial

$$\overline{T}_\theta = \frac{\int_0^\pi \left(a_4\theta^4 + a_3\theta^3 + a_2\theta^2 + a_1\theta + a_0\right)d\theta}{\pi} \tag{47}$$

The average temperature for the entire outer and inner cylinders was calculated by applying the trapezoid rule to each of the calculated azimuthally average temperatures along the height of the annulus, as

$$\overline{T} \approx \frac{1}{15}\sum_{n=0}^{14} \frac{\overline{T}_\theta\big|_{n+1} + \overline{T}_\theta\big|_n}{2} \tag{48}$$

Finally, the average wall temperature of the annulus was computed as the average of the average wall temperatures of the two cylinders, weighted by their surface areas as

$$\overline{T}_a = \frac{\overline{T}_o A_o + \overline{T}_i A_i}{A_o + A_i} \tag{49}$$

5.4.3 Average temperature considerations

After examining the temperature distribution in the annulus, it was noticed that it was apparently influenced by end effects, which may be attributed largely to radiation and conduction losses. The addition of insulation at the ends had little effect. We have decided to focus on the mid-section of the annulus, where end effects are expected to be of low importance, although it is acknowledged that end losses may affect the temperature and the flow dynamics within the entire annulus.

5.4.4 Room temperature measurement

After taking several temperature measurements around our apparatus with a handheld digital thermometer, it was noticed that the room temperature increased slightly (approximately 0.5 K) with distance from the inlet of the annulus. For this reason, the ambient temperature for our experiments was measured near the inlet. To minimize disturbances to the flow and heating of the thermocouple tip by radiation, the thermocouple was positioned at the center of the inner most past of the glass inlet as seen in Figure 46.

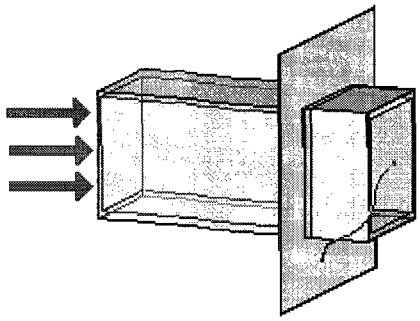

Figure 46 – Position of thermocouple used to measure the room temperature.

5.5 Mass flow rate measurement

In natural convection heat transfer, it is often difficult to measure the mass flow rate without disturbing the flow. As we observed while attempting to find the proper cross-sectional area for the rectangular glass inlet of our apparatus, even a slight obstruction to the flow can affect the system. For this reason, we decided to use particle image velocimetry (PIV) to measure the mass flow rate, as it was the least intrusive method available to us. The PIV setup we employed can be seen in Figure 47.

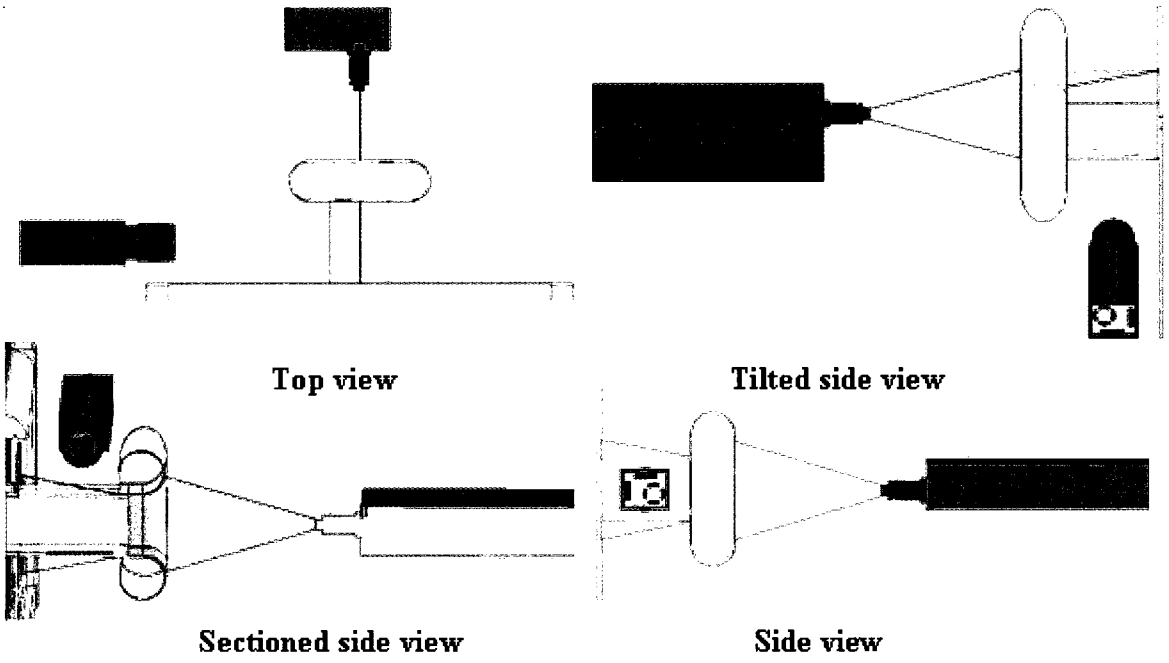

Figure 47 – PIV setup showing laser sheet and camera positioning with respect to the inlet of the bottom enclosure section of the apparatus

The glass inlet duct is the only inlet through which air can enter our setup. Therefore, the flow rate of the air entering this passage should be equal to the flow rate through the annulus. To enhance the uniformity of the velocity in the glass inlet duct we added a cylindrical lip formed out of brown paper at the inlet. Comparing measurements with and without this cylindrical lip, we found little change in the velocity values, however, the presence of the lip helped minimize the scattering of the laser as it hit the edges of the glass, which was helpful.

Two different arrangements were used for the PIV, the first was with the laser sheet horizontal and the camera looking down on the glass duct, and the second was with the laser sheet vertical and the camera looking sideways, as seen in Figure 47. The latter setup proved

to be more appropriate for our needs. Several seeding methods were tried and the best method found was to create a localized cloud of fine particles which are suspended in the air near the inlet. Because the particles used would be released into the lab from the outlet of the annulus, we decided to avoid any possibly dangerous seeding particles, and opted to use talcum powder. The chosen particles were of Johnson & Johnson scented baby powder, which not only worked quite well for our needs, but also filled the lab with an agreeable fragrance. The particle cloud near the inlet was created by means of agitating the particulate of choice in a slightly filled container by a strong jet of air. The agitated powder exited the container and filled the immediate vicinity. We then waited for a short period of time, to allow the heavier particles to settle and to allow the effects of the air jet used to agitate the particles to subside. A series of measurements were then taken with the PIV with the camera focused on the particles moving through the glass channel. In most cases, the particle cloud was quickly sucked into the inlet, followed by a plume of powder exiting the annulus at the top. PIV measurements were taken for several eccentricities and for different heat fluxes.

To calculate the mass flow rate, several assumptions were made. First, we assumed a uniform air temperature, which was measured with the thermocouple positioned at the end of the glass inlet. Second, we assumed a uniform velocity in the glass inlet. Finally, we assumed that the presence of the seeding particles did not affect the fluid properties. The mass flow rate was calculated as

$$\dot{m} = \rho V A \tag{50}$$

where ρ is the density, V is the velocity, and A is the cross-sectional area of the glass duct.

Chapter 6 Uncertainty

6.1 Temperature uncertainty

For temperature measurements using thermocouples, there are generally three sources of errors: the thermocouple sensor, the circuit which connects the thermocouples to the data acquisition system and the data acquisition system itself (Carleton and Agalloco, 1998). It may be difficult to distinguish between errors in the circuit and those in the sensor. In general, conformity and interchangeability errors are attributed to the sensor, while non-homogeneous effects are attributed to the circuit.

The conformity error is defined as the difference between the temperature reading of a thermocouple and the standard temperature[5] for a thermocouple of the same type and producing the same voltage. The maximum conformity error for a K-type thermocouple which meets acceptable industrial standards is the greater of ±2.2°C or ±0.75% of the temperature in degrees Celsius, for temperatures higher than 0°C[6]. The conformity error can be eliminated by calibration of individual thermocouples over a temperature range.

---

[5] Standard temperature is the one published in tables for a specific thermocouple type.

[6] According to the revised thermocouple reference tables provided in "The Temperature Handbook" 21st Century 2nd Edition, 2000, by Omega Engineering Inc, Laval, Quebec, Canada.

The interchangeability error has to do with the degree to which different thermocouples produce the same voltage output at the same temperature. Using thermocouples formed from the same batch of wires, the typical maximum interchangeability error is the greater of ±0.1°C or ±0.1% (Carleton and Agalloco, 1998). Similar to the conformity error, this error can be eliminated by calibration.

Depending on the exact composition and the annealing of the alloys which form the thermocouples, slight variations could lead to varying temperature readings. If the same metallic constitution is used throughout the setup, then calibration alone would eliminate most of the errors encountered in thermocouple measurements. However, it is often required to use connectors of varying composition and this introduces the error caused by non-homogeneity. In our case, thermocouple extension wire was used to connect the sensors to the data acquisition system and on the data acquisition board itself pin connectors were used. Generally, if this non-homogeneity exists on both terminals of the thermocouple and the temperatures of the terminals are the same, this effect is minimized. The data acquisition system we are using has for each module eight temperature sensors, four on each side, which are periodically sampled and used for cold junction compensation. The manufacturer, (Sensoray, Tigard, Oregon, USA) gives a cold junction uncertainty U_{RJ} of ±0.1°C for the temperature range we will encounter.

The device used as a standard for thermocouple calibration should be a highly accurate instrument, such as a platinum resistance temperature detector. As this was not available, we used a digital hand-held thermometer. The calibration of the hand-held digital thermometer was verified using an ice point reference (Model K110, Kaye Instruments, Billerica, Massachusetts, USA), which has a nominal uncertainty of ±0.1 °C. For a relatively

narrow range of temperatures, compared to the full range of the thermocouple, one could calibrate using a single reference temperature.

The 96 thermocouples in our apparatus were all corrected to the room temperature by offsetting their readings by the difference from the temperature measured with the handheld digital thermometer. Generally, there are several factors to consider when looking at sources of error in the calibration of thermocouples. These include errors inherent to the calibration device used, errors produced by curve fitting, and random errors. The calibration uncertainty U_{cal} is computed from the uncertainty of the hand held thermocouple reader U_{hh-TC} and that of the ice point reference $U_{ice-ref}$ as

$$U_{cal} = \sqrt{(U_{hh-TC})^2 + (U_{ice-ref})^2} \tag{51}$$

The data acquisition system used to record the temperatures from the 96 thermocouples is part of the Sensoray 2600 family and consists of a main module which connects to various add-on modules with various functions. We have chosen six 2608 modules, specifically designed for thermocouple sensor hook-ups. Each of the 2608 modules has 16 analog inputs and built-in reference junction compensation. These modules have a 16-bit analog to digital converter and, for thermocouples, use an input range of ±100 mV. The input impedance is 100 MΩ.

The uncertainty which arises in the data acquisition system itself can be calculated as follows. The system has a 16-bit ADC, therefore, it is capable of 2^{16} (65,536) distinct digital readings. Thus, its resolution is

$$100 \text{ mV} / 65{,}536 = 1.52 \text{ } \mu\text{V or } 1.52 \times 10^{-3} \text{ \% of the range}$$

The sensitivity of K-type thermocouples is approximately 42 μV/°C (Wilson et al., 2008), therefore, the temperature resolution of the ADC is

$$1.52 \text{ } \mu\text{V} / 42 \text{ } \mu\text{V/°C} = 0.036 \text{ °C}$$

The quantization uncertainty can be calculated as being half the ADC resolution (Tavoularis, 2005)

$$U_{ADC} = \frac{\text{resolution}}{2} \tag{52}$$

The total temperature measurement uncertainty can be calculated as

$$U_T = \sqrt{(U_{cal})^2 + (U_{ADC})^2 + (U_{RJ})^2} \tag{53}$$

Figure 48 provides sample values for uncertainties and the dependence of some uncertainties on others. This allows us to identify which uncertainties contribute the most to the overall measurement uncertainty; in this case, the handheld thermocouple reader used for calibration was found to be the greatest contributor. At the end of this chapter, we will present tables containing typical values of uncertainties.

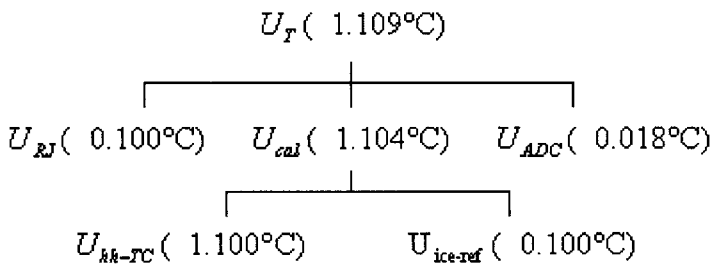

Figure 48 – Sample values of temperature related uncertainties

6.2 Heat flux uncertainty

As mentioned in section 5.3, we used two methods to calculate the heat flux, both of which required the knowledge of the current which was constant for each experimental run. As stated in section 3.2.1, the current and the voltage were recorded using a data acquisition board with a 12-bit ADC. Two configurations were used. For the majority of the experimental runs, spurious spikes in the current were present in the readings; this forced us to use a trimmed mean feature of LabVIEW, which removes potential outliers. Later on, we replaced the single ended inputs with differential inputs and reduced the analog input range of our data acquisition board from ±500 mV to ±50 mV; this eliminated such spikes.

In both configurations, the current reported by the data acquisition system was compared to measurements by a hand held ammeter and good agreement was found. It was noticed however, that increasing the percentage trim used for the first configuration resulted in a slightly different reading. The trim is applied to the extreme ends of the probability density function of a large number of samples before the average of the results is displayed and recorded. In order to avoid biasing our results, we used the largest percentage trim which would not result in a current reading difference greater than 1% of the total current. The value for the trim was fixed at 2.5% for each end. For the second configuration, no trimming was necessary.

The current is measured across a 180 A / 100 mV shunt which was built into the power supply. In the first configuration, the resolution was calculated to be 43.94 mA, whereas, in the second, the resolution was 4.39 mA. Using equation 52, the uncertainty U_I due to the ADC in the first configuration is ±21.97 mA while the uncertainty for the second configuration is ±2.19 mA. The trimming in the first configuration produces a measurable bias which can be calculated, and is not part of the uncertainty.

The voltage did not need to be corrected and did not show any spikes or anomalies. Also, because the voltage was measured at the source, we did not need to account for the voltage drop in the power cables from the power supply to the annulus. Therefore, the only uncertainty associated with the voltage measurement is that of the analog to digital converter. The range for the voltage was set to ± 5 V and, therefore, the resolution for the voltage was 2.44 mV. The uncertainty U_E due to the ADC is ±1.22 mV.

There is also an uncertainty in the calculation of the area of the stainless steel foil which should be taken into account. If we consider that we have an uncertainty of ±0.5 mm variation in the length l and the width w of the foil, which are mainly due to the cutting technique used, then the uncertainty of the area can be given as

$$U_A = \sqrt{(lU_w)^2 + (wU_l)^2} \tag{54}$$

Because the resistivity depends on the surface temperature and the heat flux depends on the resistivity, an exactly constant heat flux was unattainable along the entire annulus. One way to estimate the contribution of the uncertainty of resistivity due to temperature is to simply assume any variation as part of the uncertainty; this is done as follows

$$U_\rho = \pm\left(\frac{\rho_{\max} - \rho_{\min}}{2}\right) \tag{55}$$

for which ρ_{max} and ρ_{min} are the resistivities at the maximum and minimum temperature points on the foil.

The resistance is affected by the resistivity as well as the dimensions of the foil, namely its length and cross-sectional area. Variations in the thickness of the foil are a concern when looking at uncertainties in resistance. However, because we do not have any information on this, and we did not perform any experiments to determine any possible variation in thickness, we have not included possible thickness variations in our estimates of uncertainty. The uncertainty of the resistance of the foil can be calculated as follows

$$U_R = \sqrt{\left(\frac{l}{wt}U_\rho\right)^2 + \left(\frac{\rho}{wt}U_l\right)^2 + \left(-\frac{\rho l}{w^2 t}U_w\right)^2} \tag{56}$$

The uncertainty of the heat flux can be computed from the uncertainties of the electrical current, area and resistance as follows

$$U_{q''} = \sqrt{\left(\frac{2IR}{A}U_I\right)^2 + \left(\frac{I^2}{A}U_R\right)^2 + \left(-\frac{I^2 R}{A^2}U_A\right)^2} \tag{57}$$

One should note that we did not take into account the precision uncertainty; this is because we used such a high number of samples that this uncertainty is negligible. Figure 49 shows the uncertainty of the heat flux and its dependence on other uncertainties. This figure presents a sample of uncertainty values for the inner cylinder with an eccentricity of 0.5 and

a wall heat flux of 80 W/m^2. A table with typical values of uncertainties for the outer cylinder is presented at the end of this chapter.

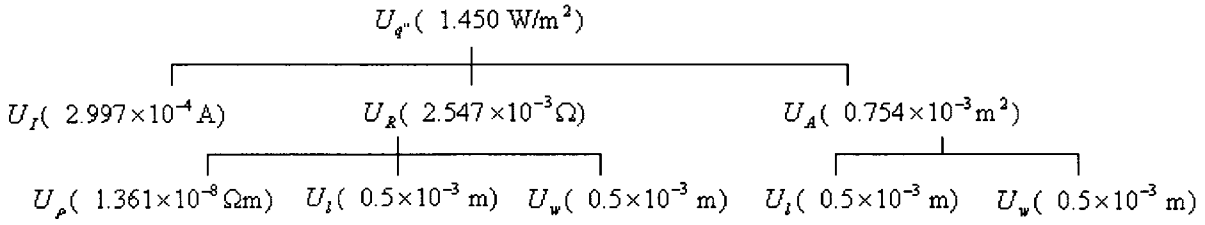

Figure 49 – Sample values of heat flux related uncertainties for the inner cylinder; e = 0.5, q'' = 80 W/m^2

6.3 Convection heat transfer coefficient

The overall heat transfer coefficient is defined as

$$\bar{h} = \frac{q''}{(\bar{T}_w - \bar{T}_m)} \tag{58}$$

where $\bar{T}_w$ is the average wall temperature and $\bar{T}_m$ is the average mean fluid temperature. Therefore its uncertainty can be estimated as

$$U_{\bar{h}} = \sqrt{\left(\frac{1}{(\bar{T}_w - \bar{T}_m)} U_{q''}\right)^2 + \left(-\frac{q''}{(\bar{T}_w - \bar{T}_m)^2} U_{T_w}\right)^2 + \left(\frac{q''}{(\bar{T}_w - \bar{T}_m)^2} U_{T_m}\right)^2} \tag{59}$$

Figure 50 shows a sample value of the overall heat flux coefficient uncertainty for the inner cylinder with e = 0.5 and q'' = 80 W/m^2.

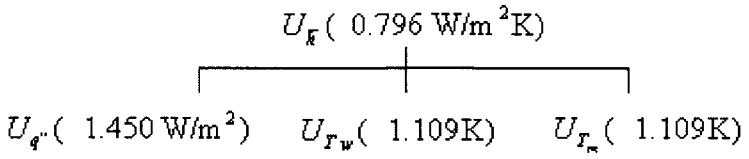

Figure 50 – Sample values of heat flux coefficient related uncertainties for the inner cylinder; $e = 0.5$, $q'' = 80$ W/m^2

6.4 Typical values of uncertainties

Table 5 contains typical values of temperature related uncertainties. These uncertainties vary with temperature, but, for the temperature range we will encounter, the variation is very small. The uncertainties presented in this table are realistic and close to the maximum uncertainty provided by the data acquisition supplier (Sensoray, Tigard, Oregon, USA). The supplier claimed that the data acquisition system was calibrated such that in the worst case we would have ±1°C, which included errors introduced by the thermocouples.

Table 5 – Typical temperature related uncertainties

T [ºC]	U_T [ºC]	U_{RJ} [ºC]	U_{cal} [ºC]	U_{ADC} [ºC]	$U_{hh\text{-}TC}$ [ºC]	$U_{ice\text{-}ref}$ [ºC]
20	1.03	0.10	1.02	0.02	1.02	0.10
70	1.08	0.10	1.07	0.02	1.07	0.10

In Table 6 we present typical values of heat flux and heat transfer coefficient uncertainties for the outer cylinder. The maximum heat flux uncertainty was 2.1% that of the total heat flux. In the case of the heat transfer coefficient, we encountered very large relative uncertainties, up to 34.4%. One of the greatest contributors to this uncertainty is temperature.

Because the average wall to mean fluid temperature difference is not very large, particularly in the case of 30 W/m^2 and zero eccentricity, the uncertainty of the temperature sensors turns out to have a magnitude comparable to that of the temperature difference itself. The values of the relative uncertainties of the heat flux and the heat flux coefficient can be found in Table 7.

Table 6 – Typical heat flux and convection coefficient related uncertainties

e	q'' [W/m^2]	$U_{q''}$[W/m^2]	U_h[W/m^2K]	U_A [cm^2]	U_R [mΩ]	U_ρ [μΩ-cm]
0.0	**30.13**	0.27	2.27	7.61	0.65	0.56
0.9	**30.42**	0.34	0.59	7.61	0.89	0.78
0.0	**80.31**	1.21	0.93	7.61	1.28	1.12
0.9	**81.00**	1.68	0.38	7.61	1.78	1.57

Table 7 – Relative uncertainties of heat flux and heat flux coefficient

e	q'' [W/m^2]	$U_{q''}$[%]	U_h[%]
0.0	**30.13**	0.9	34.4
0.9	**30.42**	1.1	16.9
0.0	**80.31**	1.5	13.4
0.9	**81.00**	2.1	8.8

Chapter 7 Experimental Results

7.1 Wall temperature thermocouple readings

In this section, we shall present the temperature distributions measured by the thermocouples in the inner and outer cylinders of the annulus. We non-dimensionalize the average wall temperature T of the inner and outer cylinders by the inlet air temperature T_{in} and the mid-height wall temperature of the annulus T_{mid} (see Figure 51) as follows

$$T^* = \frac{T - T_{in}}{2\left(T_{mid}\big|_{e=0} - T_{in}\right)} \tag{60}$$

We have chosen to use a common mid-height temperature for all eccentricities (one for the inner cylinder and another for the outer cylinder); this was the value for $e = 0$; otherwise, all dimensionless temperature curves would coincide at the midpoint, and the significance of the temperature variation may be difficult to see.

Ideally, one would have non-dimensionalized using the inlet and the exit wall temperatures. Due to end effects, however, we found that the maximum wall temperature is actually not located at the exit of the annulus. Also, it was noticed as can be seen in the results, that the temperature gradient away from the ends of the annulus is approximately linear. This means, that if we extrapolate the central temperature profile along the height of

the annulus, we would get a higher maximum wall temperature as a result of removing end effects.

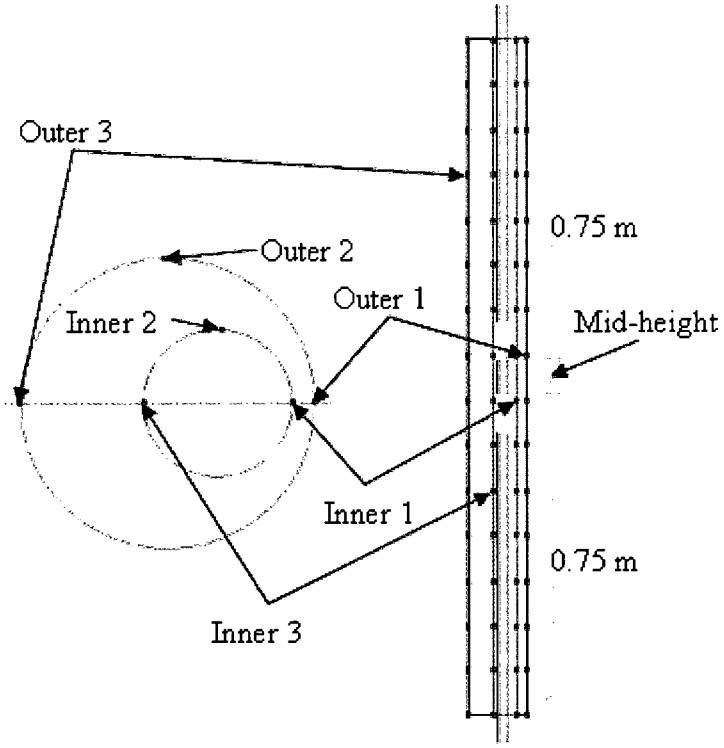

Figure 51 – Thermocouple positions (marked in red) and mid-height position definition

As opposed to extrapolating and having the added ambiguity due to fitting a linear profile to the temperature curve, we decided to use the directly measurable temperature at the mid-height of the annulus. For consistency of value range with the idealized non-dimensionalization approach, we doubled the denominator. This will give non-dimensional temperatures that would nominally be within the range between 0 and 1. Nevertheless, because the wall temperature at the inlet is always greater than the inlet air temperature, we will never encounter a non-dimensional temperature equal to 0; similarly, because of the wall temperature drop at the outlet, the maximum dimensionless temperature presented will

never be as high as 1. The inlet and mid-height temperatures are presented in Table 8 and Table 9 for wall heat fluxes of 30 W/m^2 and 80 W/m^2, respectively.

Table 8 – Inlet and mid-height temperatures for a wall heat flux of 30 W/m^2

	T_{in} [K]	T_{mid} [K]					
e	**All**	**Inner 1**	**Inner 2**	**Inner 3**	**Outer 1**	**Outer 2**	**Outer 3**
0	295.8	307.2	307.4	307.5	307.3	307.4	307.6
0.1	295.4	307.1	306.9	306.7	307.0	306.9	306.9
0.3	295.6	308.6	307.6	307.0	308.2	307.5	307.2
0.5	295.6	310.8	308.9	307.6	310.0	308.5	307.7
0.7	296.3	313.5	311.1	309.1	312.3	310.2	308.9
0.8	298.6	317.0	314.5	312.1	315.9	313.4	311.9
0.9	297.6	316.8	314.3	311.6	315.7	313.0	311.6

Table 9 – Inlet and mid-height temperatures for a wall heat flux of 80 W/m^2

	T_{in} [K]	T_{mid} [K]					
e	**All**	**Inner 1**	**Inner 2**	**Inner 3**	**Outer 1**	**Outer 2**	**Outer3**
0	296.9	320.7	320.9	321.2	321.2	321.3	321.8
0.1	297.9	322.6	322.1	322.1	322.9	322.6	322.7
0.3	298.4	325.1	323.2	322.3	324.9	323.5	322.9
0.5	297.6	329.4	325.2	322.7	328.1	324.7	323.1
0.7	297.8	335.4	329.3	324.5	333.1	327.5	324.7
0.8	297.6	337.3	330.9	325.3	335.0	328.5	325.3
0.9	297.1	338.0	331.6	325.6	336.0	328.9	325.4

It may be argued that, for each of the six horizontal temperature profiles designated by the azimuthal thermocouple locations such as Inner 1 and Outer 1, we should have non-dimensionalized the measurements using the mid-height temperature of that specific profile. However, doing so would make it difficult to see the effects of eccentricity on the temperature profiles, because we would be forcing all the temperature curves to pass through

the same point for $z^* = 0.5$. To avoid this problem, we have decided to non-dimensionalize the temperature profiles for the inner cylinder by the inlet temperature and the mid-height temperature at Inner 2; similarly, for the outer cylinder, we used the inlet temperature and the mid-height temperature at Outer 2. As well, due to the fact that the dimensionless temperature profiles for the two wall heat fluxes are very close to each other, with a maximum difference of 0.04, we have shifted the temperature profiles of the 80 W/m^2 case upwards by 0.3, so that the results for the two cases can be clearly distinguished.

Figure 52 to 58 present temperature measurements versus distance from the inlet of the annulus for different eccentricities. In all these figures, dashed lines correspond to a wall heat flux of 30 W/m^2 while solid ones correspond to a wall heat flux of 80 W/m^2. Moreover, □, △, and ○ represent positions 1, 2, and 3 of the inner cylinder, respectively, while matching solid symbols represent corresponding positions of the outer cylinder.

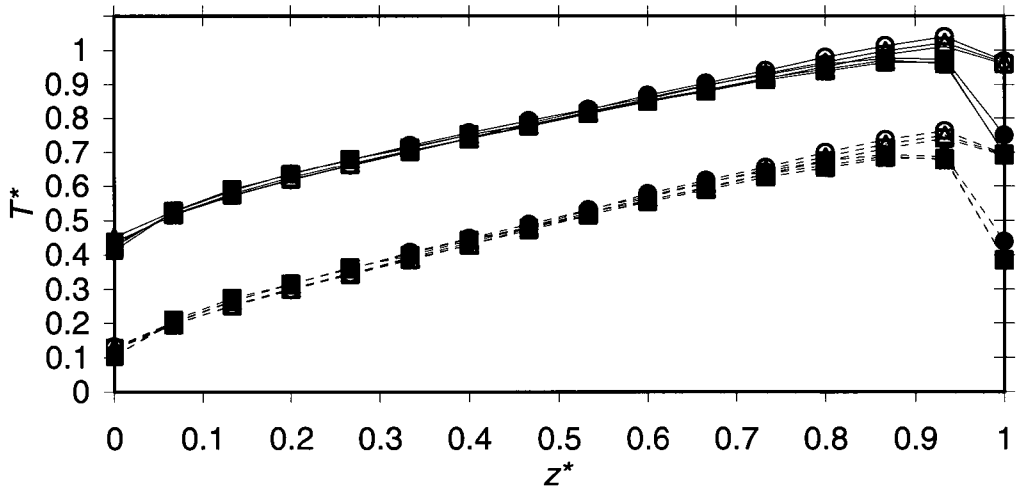

Figure 52 – Dimensionless temperature along the inner and outer cylinders for e = 0

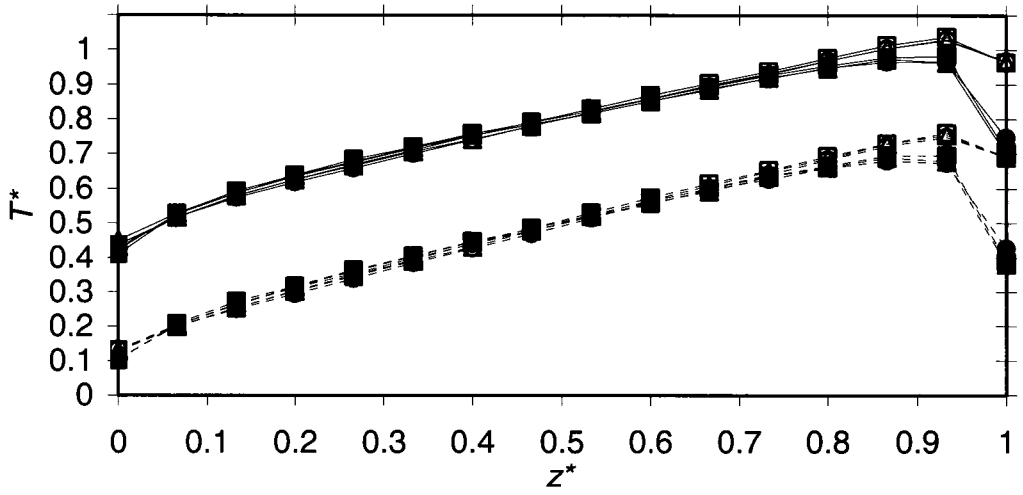

Figure 53 – Dimensionless temperature along the inner and outer cylinders for e = 0.1

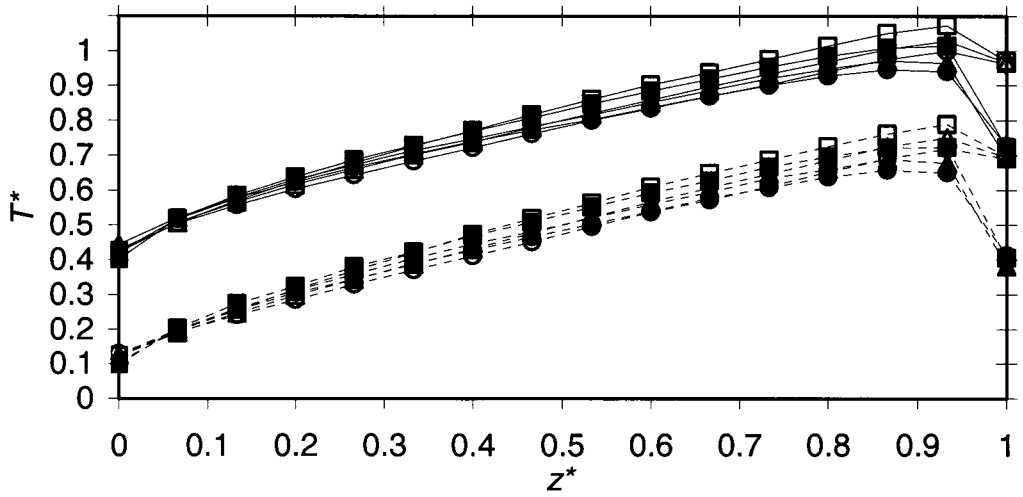

Figure 54 – Dimensionless temperature along the inner and outer cylinders for e = 0.3

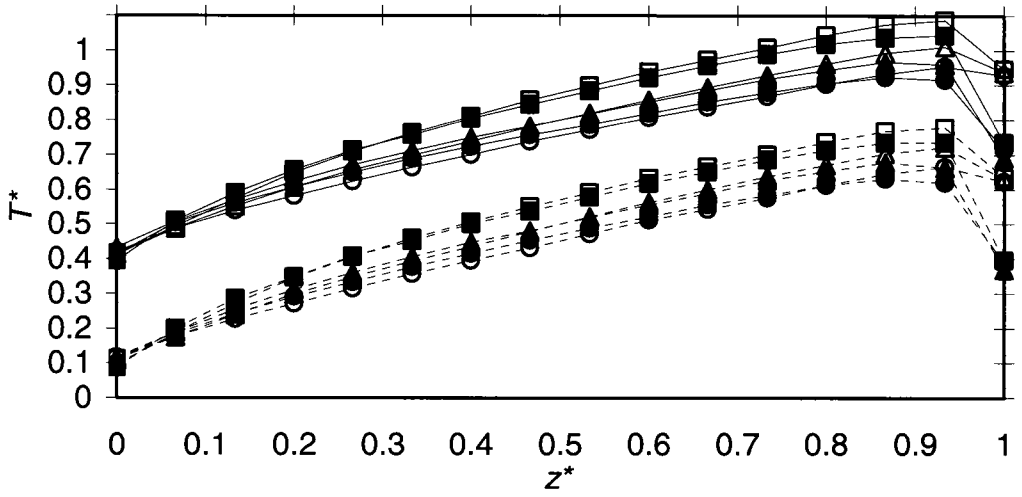

Figure 55 – Dimensionless temperature along the inner and outer cylinders for e = 0.5

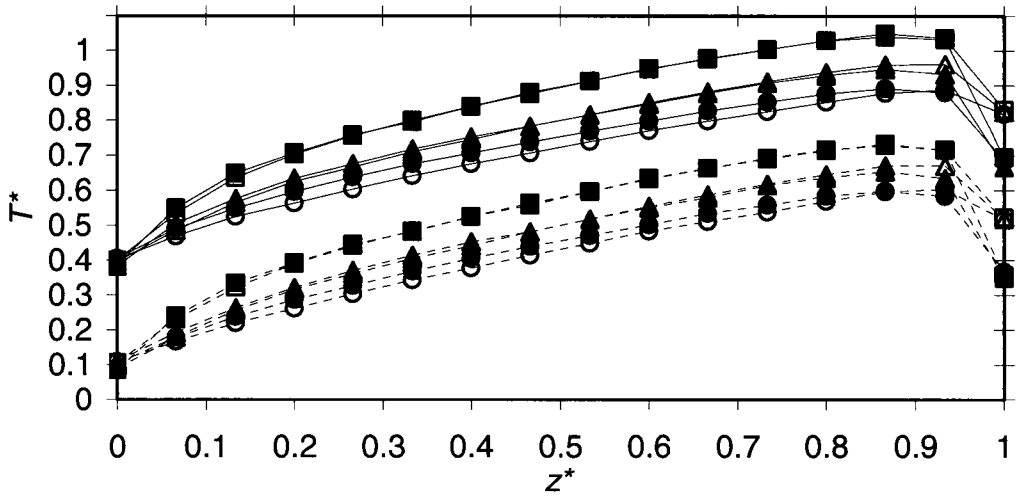

Figure 56 – Dimensionless temperature along the inner and outer cylinders for e = 0.7

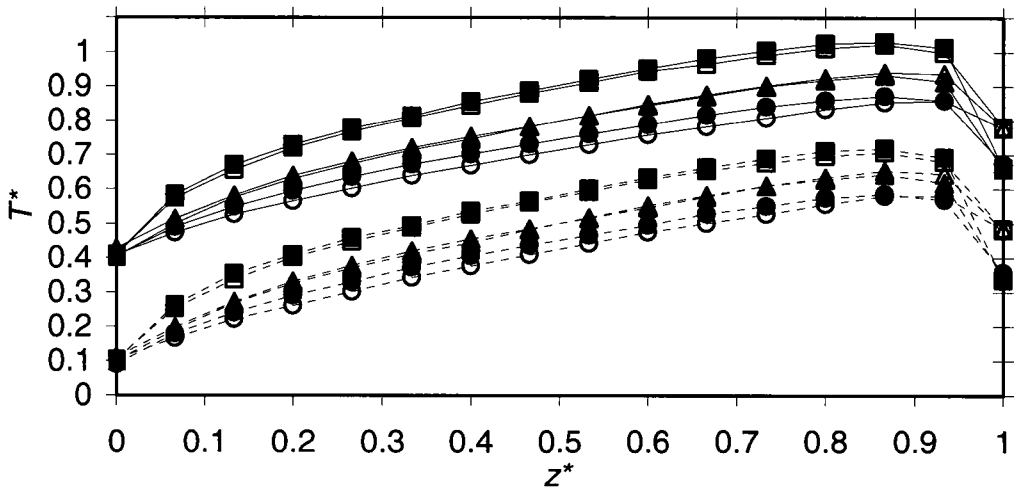

Figure 57 – Dimensionless temperature along the inner and outer cylinders for e = 0.8

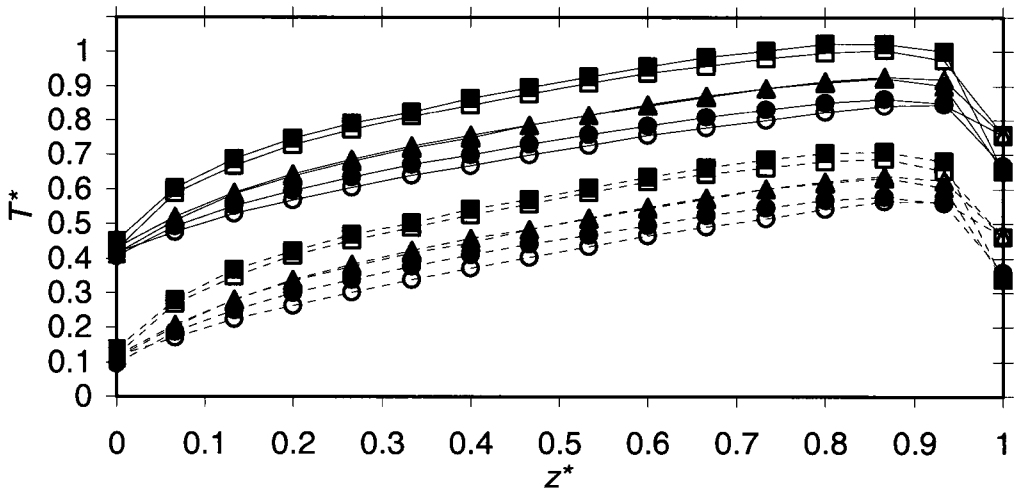

Figure 58 – Dimensionless temperature along the inner and outer cylinders for e = 0.9

Figure 59 shows the temperature variation recorded by six thermocouples at a height of 0.8 m from the inlet over an approximately 250 hour time period. Eccentricity was varied from 0 to 0.8 and one can see the effect of this on the different azimuthal thermocouple positions. It is noticed that thermocouple positions *inner 3* and *outer 3* are affected by the

changes in eccentricity to a lesser extent than those of positions *inner 1* and *outer 1*. As well, just before the 100 hour mark, a noticeable spike in the temperature at all thermocouple positions can be seen. This spike was a result of a slight constriction to the flow at the glass inlet of our setup. The result was an increase in temperature until the constriction was removed. This demonstrates the sensitivity of the setup, and the importance of properly sizing the glass inlet.

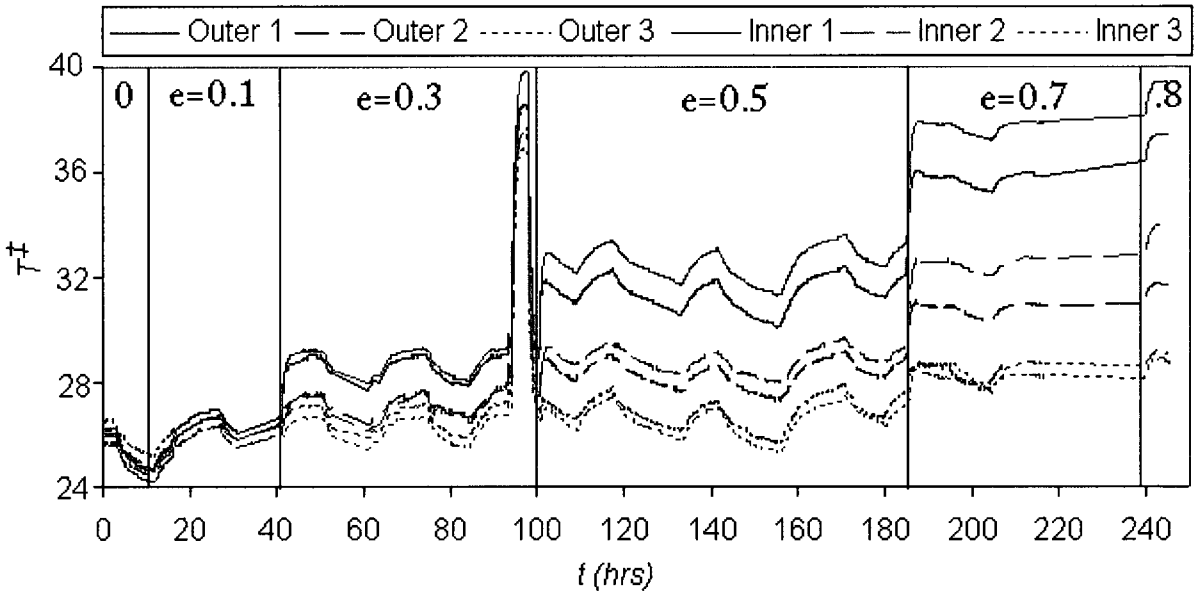

Figure 59 – Temperature variation with time starting from $e = 0$ till $e = 0.8$ for $q'' = 80$ W/m^2 and at an annulus height $z^* = 0.533$

As can be seen in Figure 52, for the concentric case, the azimuthal temperature profiles seam to collapse. As eccentricity increased, particularly in the highly eccentric case presented in Figure 58, the temperature profiles for *inner* 1, 2 and 3, and *outer* 1, 2, and 3,

are spread apart, with thermocouple positions *inner* and *outer* 1, having the highest temperatures and thermocouple positions *inner* and *outer* 3 having the lowest temperatures.

To further illustrate this, we have plotted the azimuthal temperature variations at the mid-height of the channel for the inner and outer cylinders for wall heat fluxes of 30 W/m^2 (Figure 60 and Figure 61, respectively) and 80 W/m^2 (Figure 62 and Figure 63, respectively).

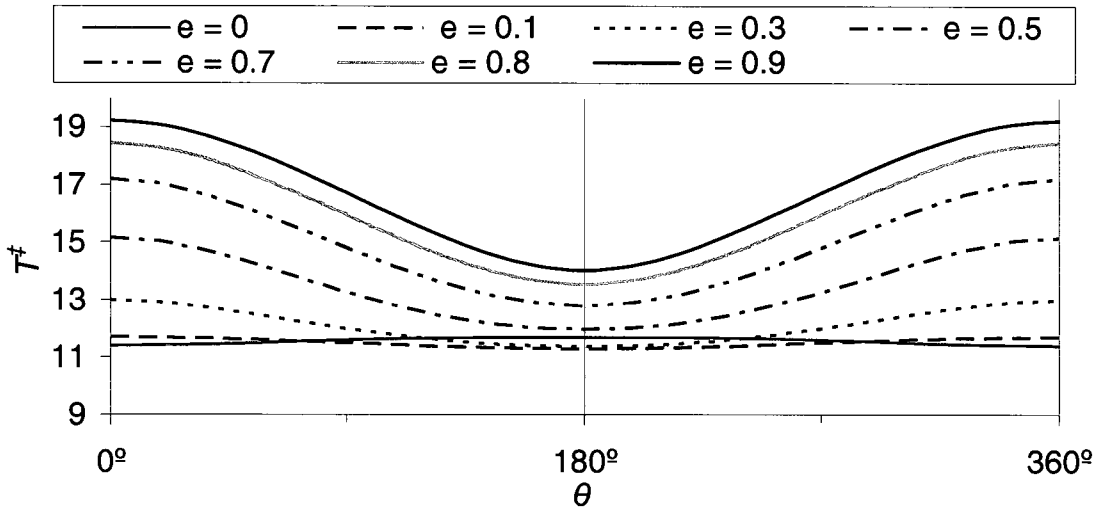

Figure 60 – Azimuthal temperature distribution for the inner cylinder at the mid-height of the annulus for $q'' = 30$ W/m^2

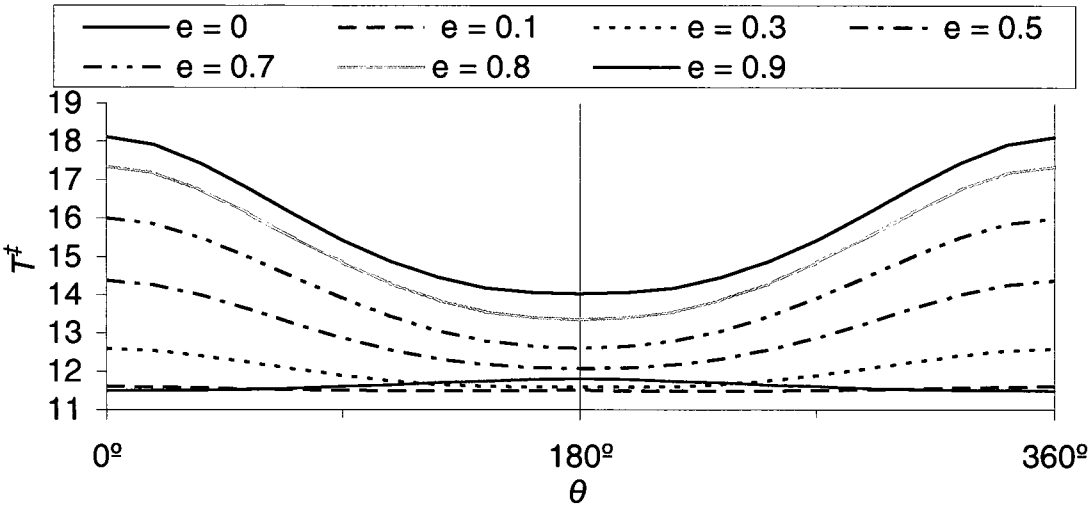

Figure 61 – Azimuthal temperature distribution for the outer cylinder at the mid-height of the annulus for $q'' = 30$ W/m^2

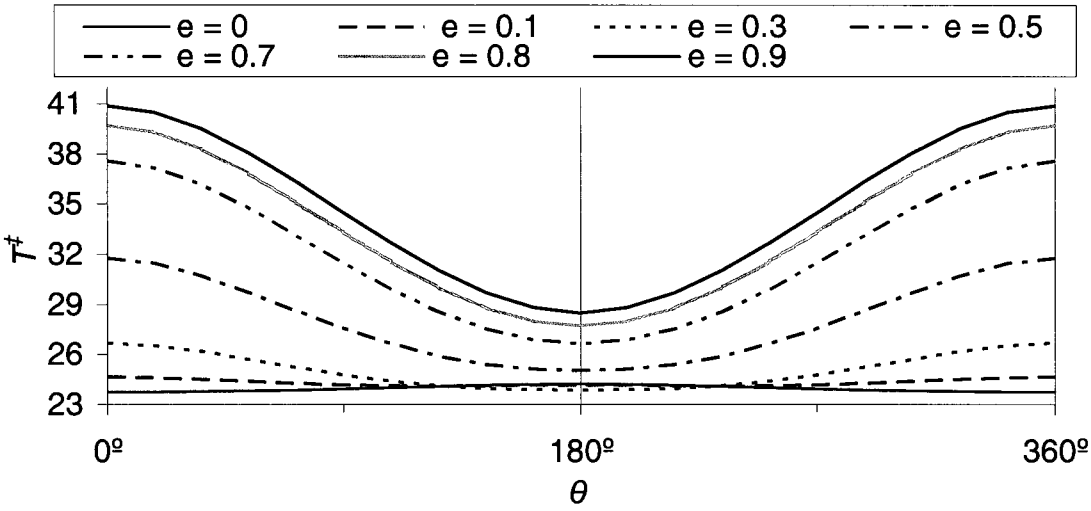

Figure 62 – Azimuthal temperature distribution for the inner cylinder at the mid-height of the annulus for $q'' = 80$ W/m^2

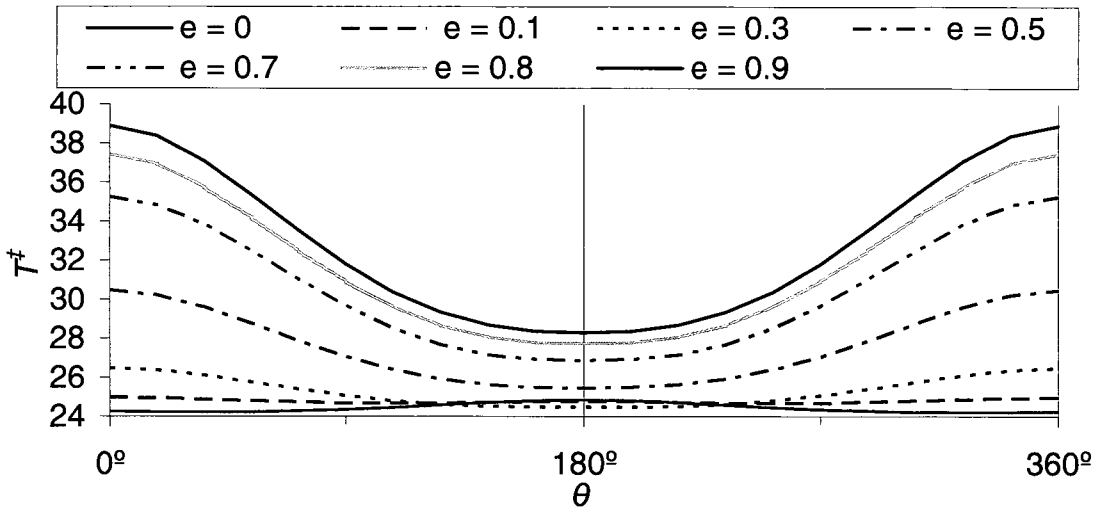

Figure 63 – Azimuthal temperature distribution for the outer cylinder at the mid-height of the annulus for $q'' = 80$ W/m^2

In Figure 60 to 63 it may be noticed that, for an eccentricity of zero, the azimuthal temperature profile was slightly non-uniform, whereas the temperature profile for an eccentricity of 0.1 appeared to be less non-uniform. This may be a result of imperfections in the geometry of the annulus.

The azimuthally averaged temperatures of the inner and outer cylinders at each horizontal thermocouple plane, non-dimensionalized by the inlet temperature and the mid-height average temperature at each eccentricity, are presented in Table 10.

Table 10 – Inlet and mid-height temperatures along the annulus

	30 W/m^2		80 W/m^2	
e	T_{in} [K]	$\overline{T}_{mid}$ [K]	T_{in} [K]	$\overline{T}_{mid}$ [K]
0	295.8	307.4	296.9	321.2
0.1	295.4	306.9	297.9	322.5
0.3	295.6	307.6	298.4	323.6
0.5	295.6	308.8	297.6	325.3
0.7	296.3	310.7	297.8	328.7
0.8	298.6	314.0	297.6	330.0
0.9	297.6	313.7	297.1	330.5

The average azimuthal wall temperature $\overline{T}_w$ was non-dimensionalized using the inlet air temperature T_{in} and the average mid-height annulus temperature $\overline{T}_{mid}$ as follows

$$\overline{T}^* = \frac{\overline{T}_w - T_{in}}{2\left(\overline{T}_{mid} - T_{in}\right)} \tag{61}$$

Average temperatures take into account the wall temperature of both the inner and outer cylinder as well as the areas of these cylinders as presented in equation 49. The average annulus temperature taken at each horizontal thermocouple plane is plotted versus distance from the inlet in Figure 64.

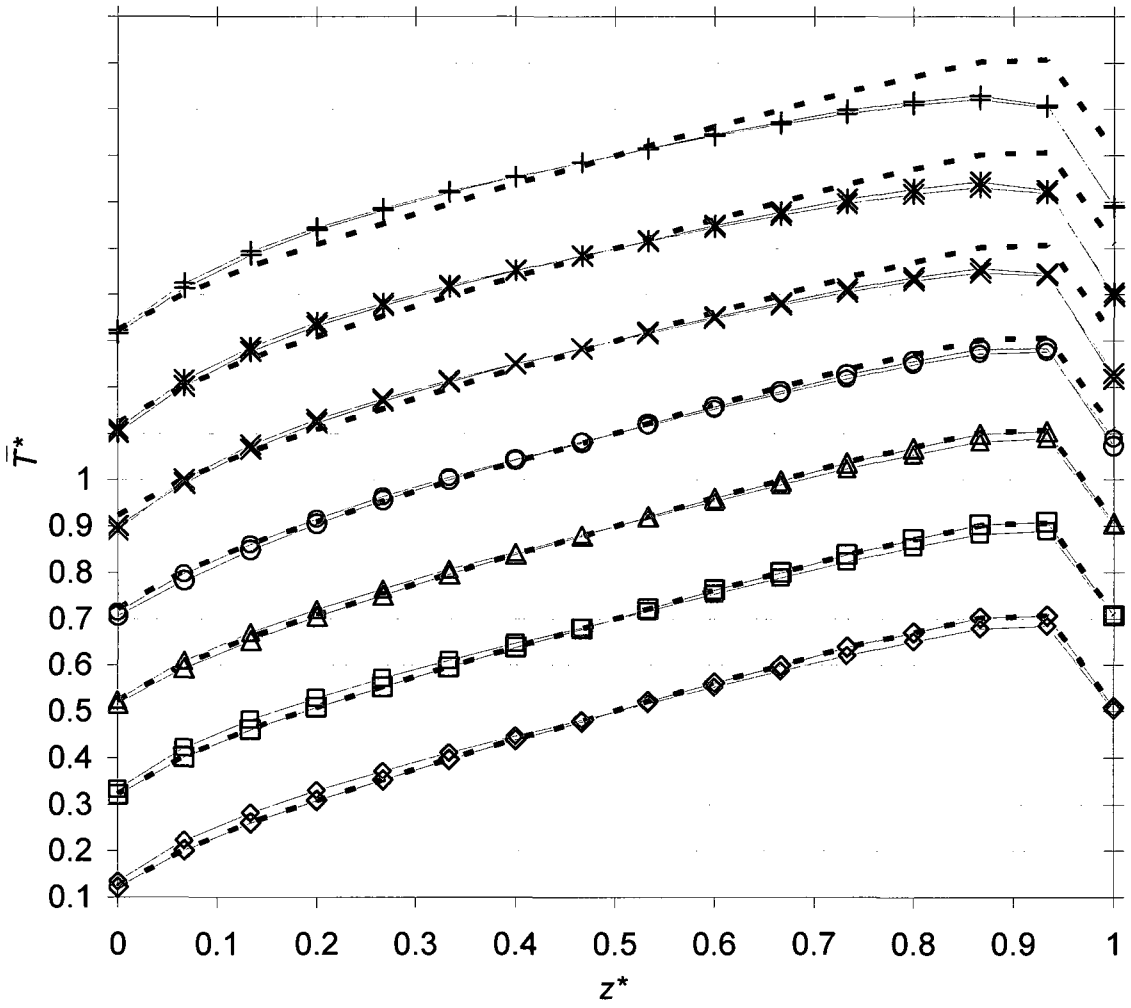

Figure 64 - Dimensionless azimuthally averaged temperature variation along the annulus for e = 0 (◇), 0.1 (□), 0.3 (△), 0.5 (○), 0.7 (×), 0.8 (✳), and 0.9 (+); the scale for each eccentricity has been shifted upwards by 0.2 compared to the scale for the previous value; dashed black lines show the temperature profile for the concentric case with $q'' = 30$ W/m^2 as a reference; blue symbols correspond to $q'' = 30$ W/m^2, red ones correspond to $q'' = 80$ W/m^2

It has been observed that the average annulus wall temperature increases with increased eccentricity over the entire measured range of eccentricity for both wall heat fluxes. The general effect of eccentricity on wall temperature for different wall heat fluxes appears to be consistent; however the higher wall heat flux gives a higher temperature gradient along the annulus. At lower eccentricities, the increase in the average wall

temperature is primarily dominant in the upper half of the annular channel, while at higher eccentricities the increase of the wall temperature is more evident in the lower half. This is illustrated in Figure 65.

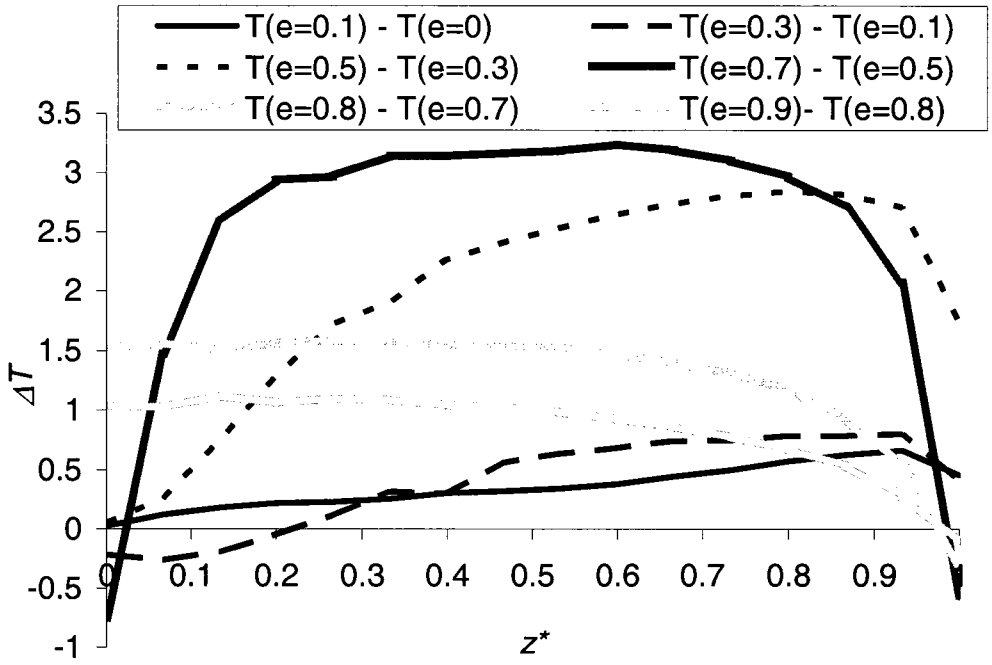

Figure 65 – Average wall temperature increase as eccentricity is increased for $q'' = 80$ W/m^2

7.2 Current and voltage measurements

Table 11 and 12 list measurements of the current and voltage and the corresponding heat fluxes. The standard deviations presented in these tables were computed from recorded measurements over several hours. The maximum relative standard deviation for the current was 0.44% while that for the voltage was 0.19%. As we held the current constant and because the annulus temperature increased with eccentricity, an increase in the voltage and consequently an increase in the wall heat flux occurred with eccentricity. The maximum

variation in the wall heat flux was 2.15% while the maximum increase in voltage was 1.14%.

Table 11 – Averages and standard deviations of current and voltage measurements and corresponding heat fluxes for different eccentricities for $q'' \approx 30$ W/m^2

	Inner cylinder					Outer cylinder				
e	I [A]	σ_I [mA]	E [V]	σ_E [mV]	q'' [W/m^2]	I [A]	σ_I [mA]	E [V]	σ_E [mV]	q'' [W/m^2]
0	7.12	23.92	1.01	0.33	30.01	11.76	22.68	1.00	0.36	30.13
0.1	7.15	13.45	1.01	0.34	30.19	11.80	16.71	1.00	0.34	30.25
0.3	7.16	13.83	1.02	0.34	30.25	11.80	16.56	1.00	0.32	30.28
0.5	7.15	12.26	1.02	0.24	30.27	11.80	14.92	1.00	0.45	30.28
0.7	7.16	12.52	1.02	0.33	30.41	11.80	14.80	1.01	0.42	30.33
0.8	7.21	14.11	1.02	0.44	30.65	11.81	18.16	1.01	0.52	30.40
0.9	7.21	31.90	1.02	0.89	30.63	11.81	27.15	1.01	0.48	30.42

Table 12– Averages and standard deviations of current and voltage measurements and corresponding heat fluxes for different eccentricities for $q'' \approx 80$ W/m^2

	Inner cylinder					Outer cylinder				
e	I [A]	σ_I [mA]	E [V]	σ_E [mV]	q'' [W/m^2]	I [A]	σ_I [mA]	E [V]	σ_E [mV]	q'' [W/m^2]
0	11.59	14.55	1.65	0.29	79.59	19.09	15.99	1.65	0.44	80.31
0.1	11.63	17.50	1.65	3.20	79.94	19.09	18.61	1.65	1.76	80.26
0.3	11.61	14.46	1.65	0.64	79.85	19.07	14.64	1.65	1.05	80.24
0.5	11.61	16.32	1.66	2.71	80.20	19.08	15.06	1.65	1.33	80.45
0.7	11.61	12.74	1.67	0.33	80.41	19.08	14.01	1.65	0.50	80.67
0.8	11.60	14.26	1.67	0.36	80.52	19.09	15.41	1.66	0.63	80.82
0.9	11.61	16.87	1.67	0.91	80.61	19.10	16.93	1.66	0.76	81.00

The variation in the wall heat flux for different eccentricities previously presented is based on average values of the wall heat flux. Local variation in the wall heat flux also exists for each eccentricity due to temperature variations. From the maximum temperature

variation we can calculate the maximum change in resistance and, using also the corresponding current, we get the maximum local heat flux variation. The maximum local variation of wall heat flux for the 30 W/m^2 case was 2.14%, while that for the 80 W/m^2 was 4.50% corresponding to maximum wall temperature differences of 19.5 K and 41.3 K, respectively. In both cases, the maximum wall temperature difference occurred in the inner cylinder for an eccentricity of 0.8.

7.3 PIV inlet velocity measurements

Particle image velocimetry was used to measure the average velocity of the air entering the square glass inlet duct at the bottom of the apparatus. This channel is the only inlet into our setup. We assume that the density of the air entering this duct is uniform and dependent only on the inlet temperature. The average inlet velocity is obtained by integrating the 2D velocity profile curve obtained from the PIV over the square cross section of the glass inlet. From the average velocity through this channel we are able to estimate the mass flow rate of air into the annulus. Figure 66 shows a typical velocity vector map of the air passing through the glass channel. This image was produced by DaVis 7.2.

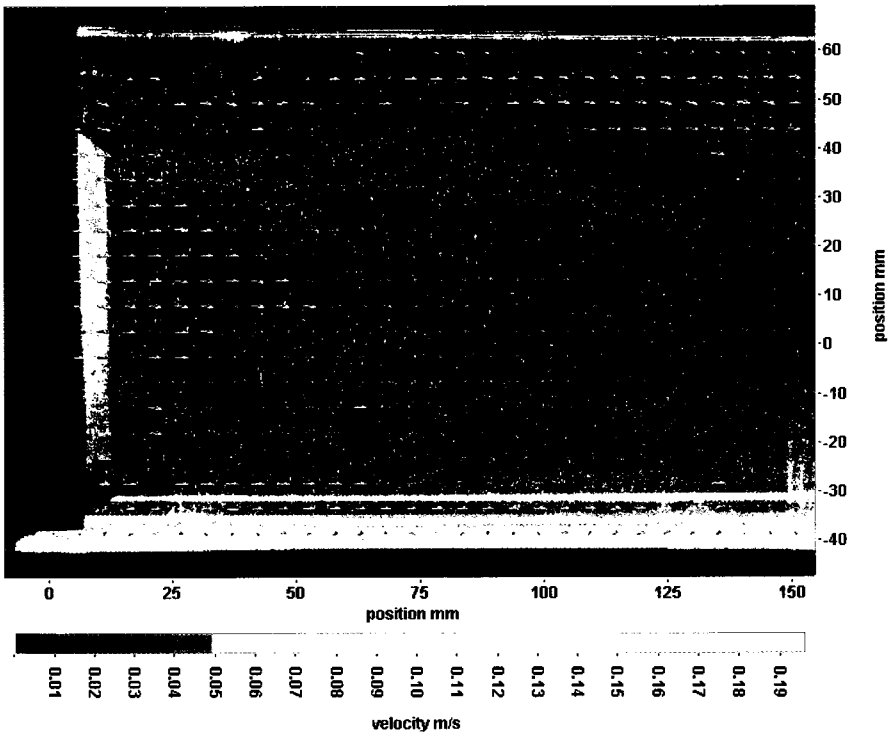

Figure 66 – Velocity vector map of air entering the glass channel

For each eccentricity, 50 PIV frame sets (0.81 seconds apart) were recorded. Each of these sets provided a velocity vector map. In the majority of the vector maps, the velocity away from the glass walls was approximately uniform, but dropped significantly as the walls were approached. In some cases, however, the vector map was irregular, and this was attributed to possible disturbances at the inlet; a typical example of such a map can be seen in Figure 67.

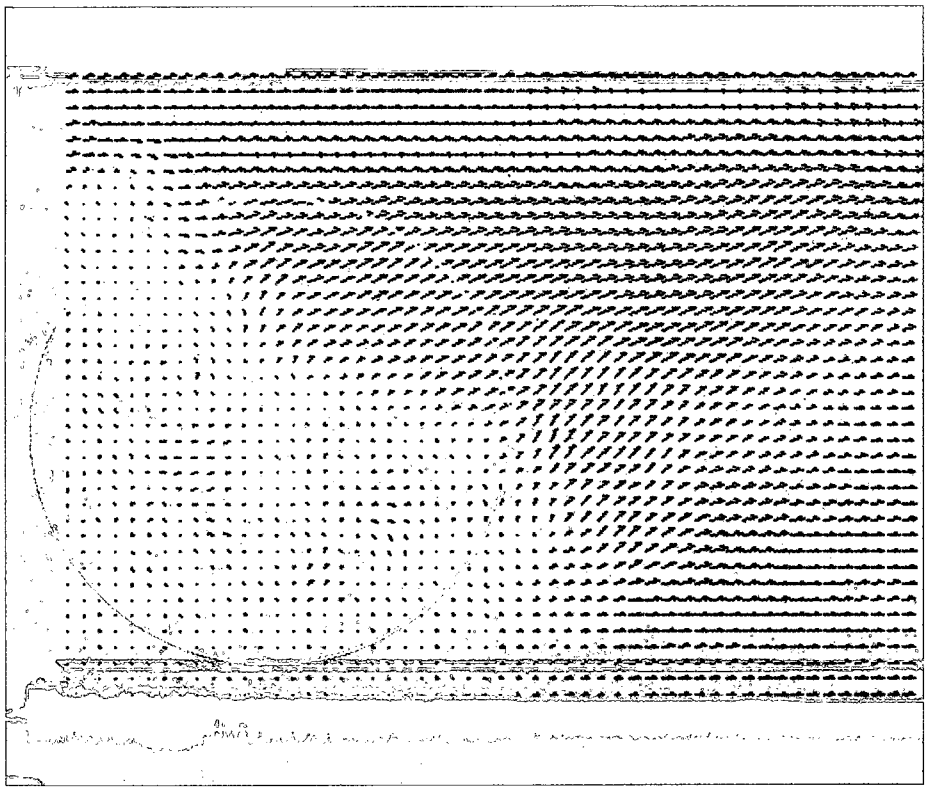

Figure 67 – Anomalous velocity vector map of air entering the glass channel (circled in red)

The purpose of the PIV measurements was to validate the estimated mass flow rates of the air passing through the annulus for different eccentricities. PIV measurements were only done for a wall heat flux of 80 W/m^2 and only for selected eccentricities. The measured velocity variations along the height of the inlet duct are presented in Figure 68, whereas Table 13 presents the corresponding average velocities and mass flow rates.

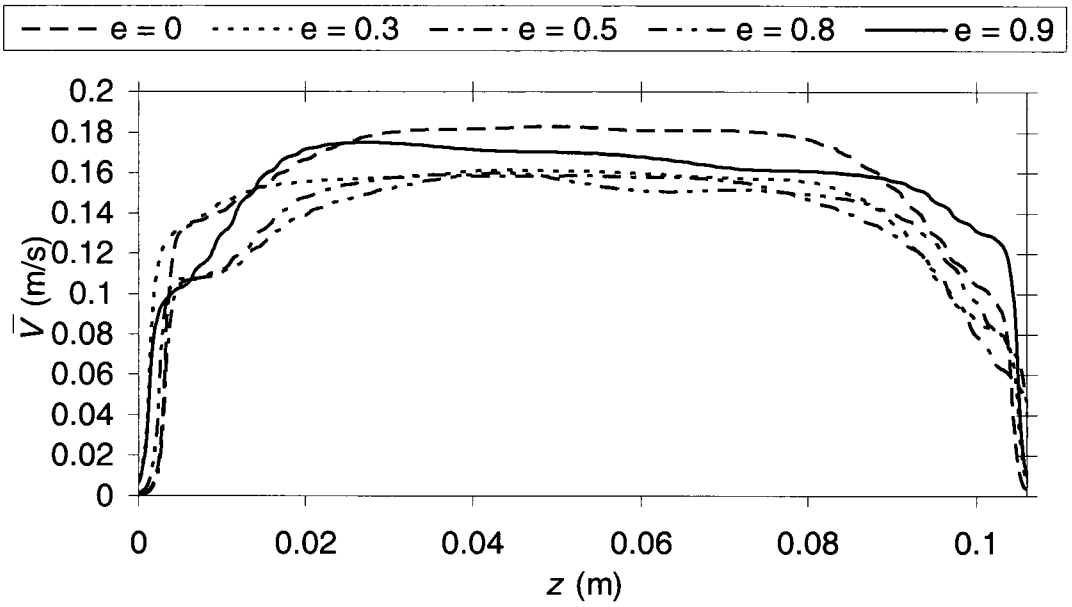

Figure 68 – Velocity variation along the height of the glass channel for $q'' = 80$ W/m^2

From Table 13, it can be seen that the mass flow rate is only mildly sensitive to eccentricity, with its values changing by less than 20% over the entire eccentricity range examined. It also appears that there is a minimum mass flow rate for an eccentricity of 0.5.

Table 13 – Average velocity and mass flow rate through the channel for $q'' = 80$ W/m^2

e	**0**	**0.3**	**0.5**	**0.8**	**0.9**
$\bar{V}$ **[m/s]**	0.137	0.130	0.117	0.121	0.140
dm/dt **[g/s]**	1.728	1.623	1.465	1.495	1.734

We compared the calculated mass flow rate using velocity obtained from PIV results with those using the velocity term in equation 67 in the upcoming chapter, by plotting the

two on the same graph. Figure 69, 70, 71, 72 and 73 show the two calculated mass flow rates for eccentricities of 0, 0.3, 0.5, 0.8 and 0.9, respectively.

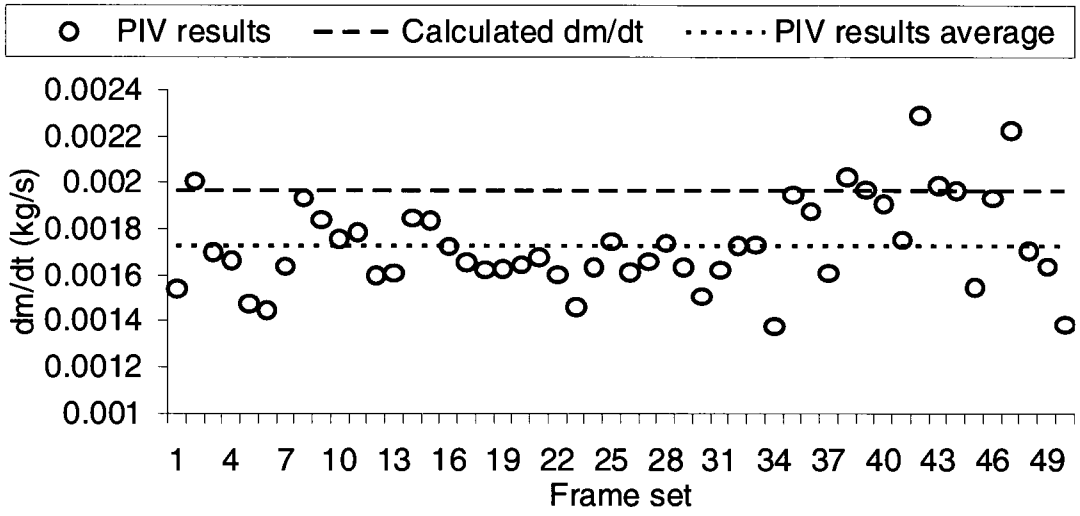

Figure 69 – Mass flow rate through the annulus calculated from PIV results compared to that calculated using measured wall temperatures for $q'' = 80$ W/m^2 and e = 0

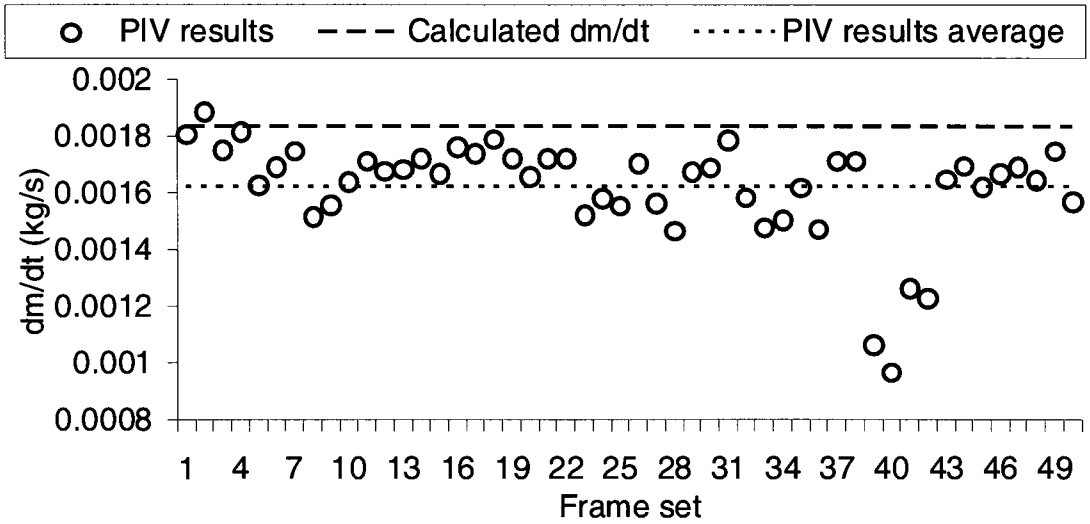

Figure 70 – Mass flow rate through the annulus calculated from PIV results compared to that calculated using measured wall temperatures for $q'' = 80$ W/m^2 and e = 0.3

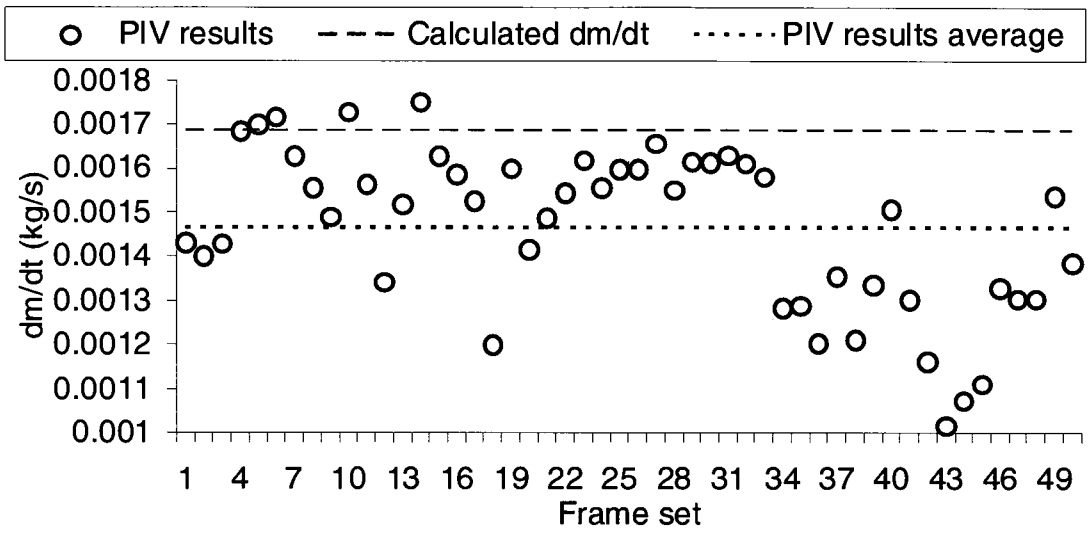

Figure 71 – Mass flow rate through the annulus calculated from PIV results compared to that calculated using measured wall temperatures for $q'' = 80$ W/m^2 and e = 0.5

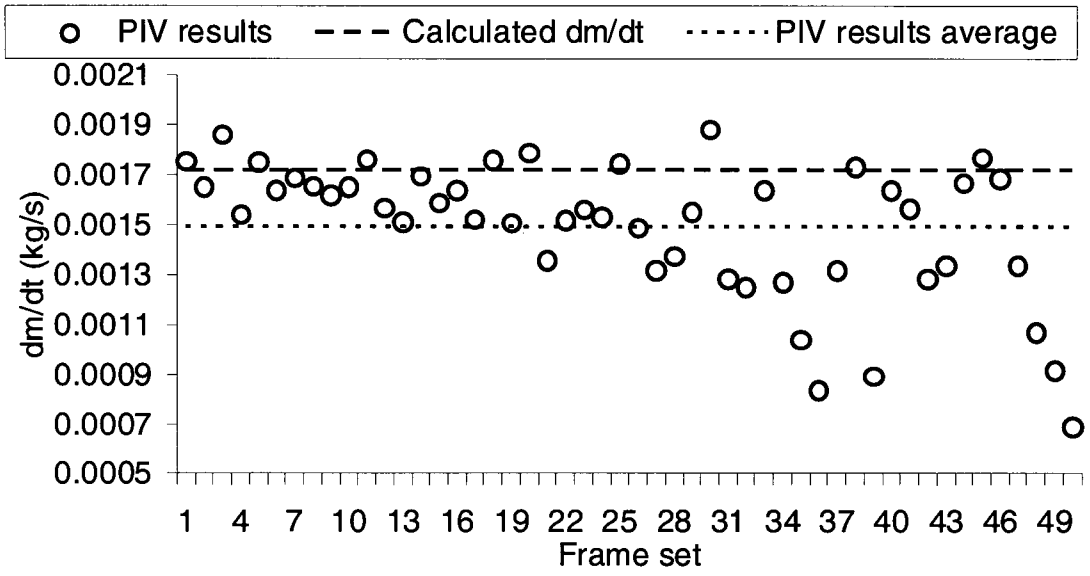

Figure 72 – Mass flow rate through the annulus calculated from PIV results compared to that calculated using measured wall temperatures for $q'' = 80$ W/m^2 and e = 0.8

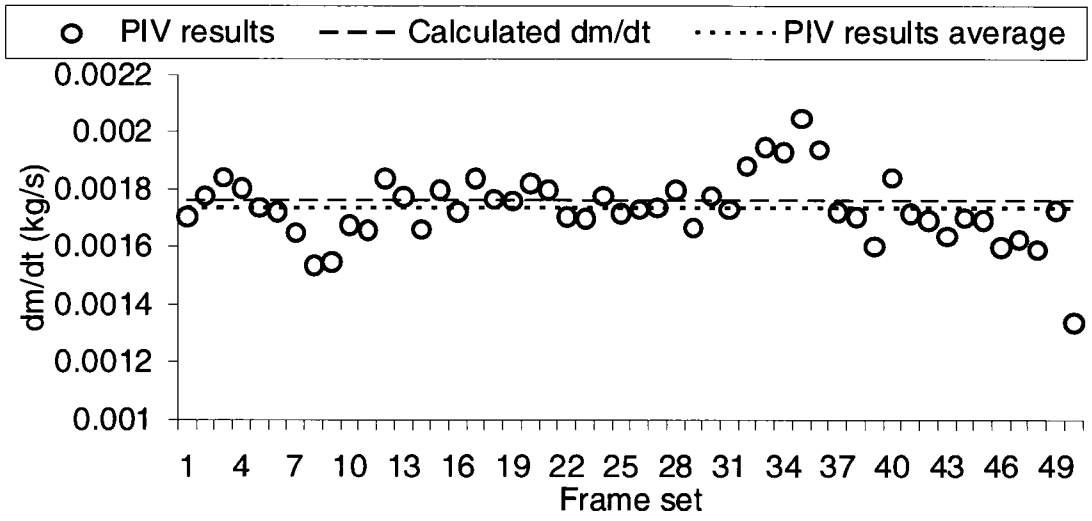

Figure 73 – Mass flow rate through the annulus calculated from PIV results compared to that calculated using measured wall temperatures for $q'' = 80$ W/m^2 and e = 0.9

For nearly all eccentricities, the mass flow rate calculated using PIV results was 11 to 13% lower than that calculated from equation 67. In the $e = 0.9$ case, however, the two mass flow rates were very close, differing by less than 2%. The reason for this is unclear; however, because of this we cannot say that the difference in the two estimates is insensitive to eccentricity. In Figure 74 we plot the mass flow rates calculated in the two different methods versus eccentricity. Both show an apparent minimum for an eccentricity of about 0.5. Figure 75 combines the mass flow rates calculated from PIV results for all 50 frame sets. Curiously, in the initial 30 frame sets the mass flow rate fluctuates within a fixed band of approximately ± 0.25 g/s, but in the following 20 frame sets the fluctuations become stronger. This may be due to a decrease in the number of particles in the flow which leads to higher uncertainty in the PIV results and brings forth some of the limitations of this approach, particularly because we did not use a steady supply of seeding particles.

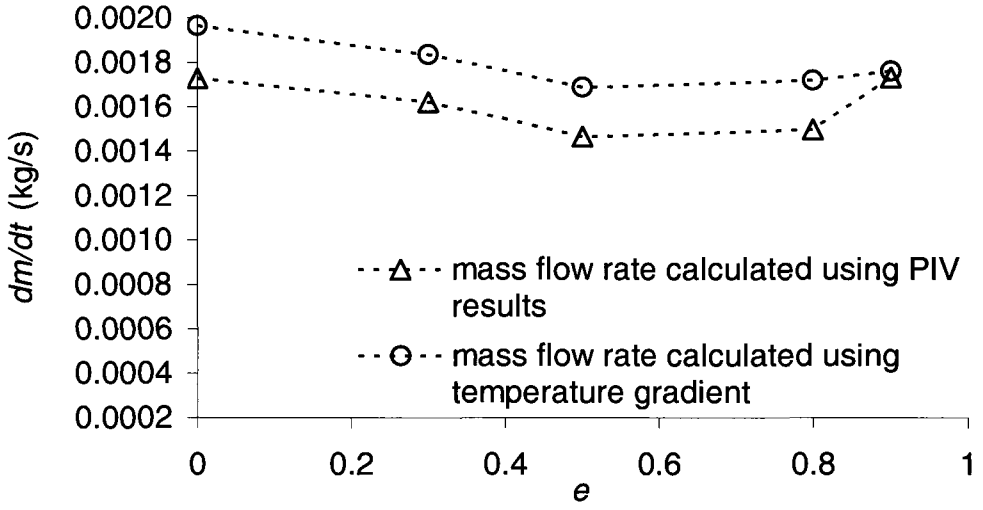

Figure 74 – Mass flow rate versus eccentricity

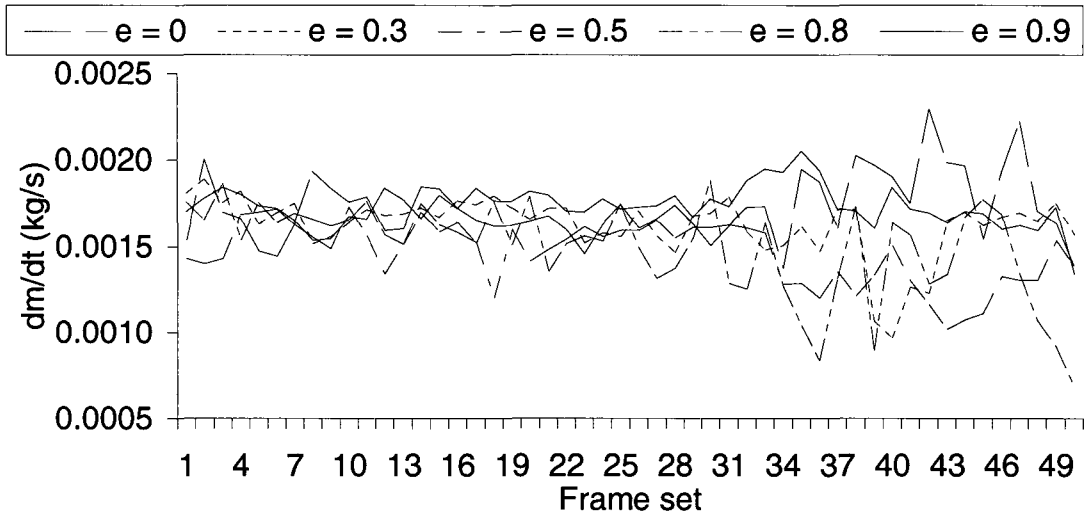

Figure 75 – Comparison of mass flow rates calculated from 50 frame sets of PIV measurements for different eccentricities

Chapter 8 Analysis and Discussion

8.1 Consideration of undesirable effects

8.1.1 Room temperature variation

A change in room temperature obviously affects directly the temperature in the annulus, as wall heating raises its temperature above the current temperature of its surroundings. In addition, however, as the wall temperature changes, the resistivity of the stainless steel foil would also be affected. In consequence, if the current were maintained constant, the Joule power would change due to the change in resistance and so would the wall heat flux. After recording the room temperature over several days, we noticed that the room temperature varied cyclically, typically (but not consistently) following a daily cycle. The room temperature depends on the ventilation system which is shut off in the evening. It was noticed that the variation during a 24 hour period was different on weekdays and weekends. On weekdays, the highest temperatures are recorded around 10:00 P.M., just before the ventilation is turned off and the lowest temperatures are recorded between 6:00 and 7:00 A.M., presumably just before the ventilation is turned on again. One should note that these measurements were taken during the winter and this trend may change during the summer.

Figure 76 shows the room temperature variation over several days. The presented values are the difference from the lowest room temperature during that time, which was 296.3 K, i.e.,

$$T^{\dagger\dagger} = T - T_{\min} \tag{62}$$

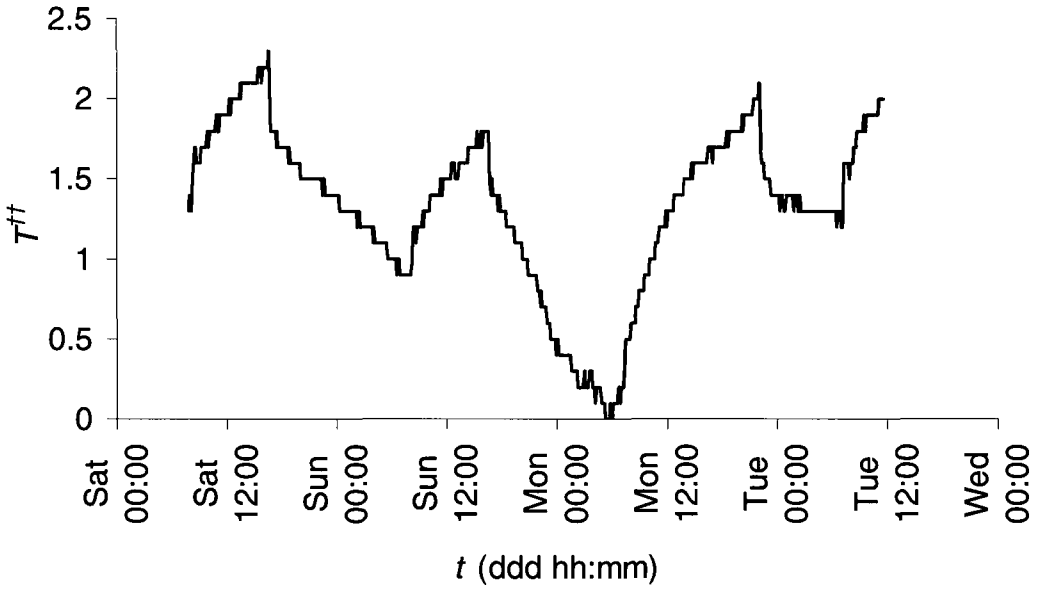

Figure 76 – Room temperature variation during three days

The maximum temperature variation during the three days considered was 2.3 K, which, if left unaccounted for, would increase significantly the uncertainty of wall temperature measurement. As maintaining the room temperature constant was beyond our control, it became necessary to investigate how the fluctuating room temperature affects the annulus temperature. Towards this objective, we monitored both the room temperature and the average wall temperature in the heated annulus for the representative conditions of a wall heat flux of 80 W/m^2 and an eccentricity of 0.5 over the same three-day period. The

differences of these temperatures from their corresponding minimum values have been plotted in Figure 76, which shows that the temperature in the annulus followed roughly, but not exactly, the room temperature and that the maximum temperature changes in both were approximately the same, i.e., 2.3 K.

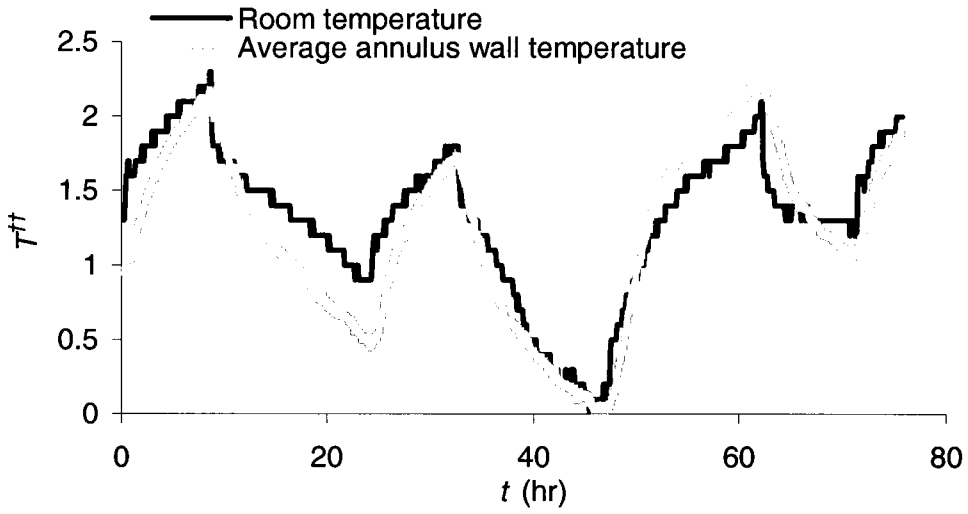

Figure 77 – Variations of the room temperature and the average annulus wall temperature for a wall heat flux of 80 W/m^2 and an eccentricity of 0.5

Any time the eccentricity or the power applied to the annulus were changed, the wall temperature would change gradually, approaching a new asymptotic value, assuming of course that the room temperature would remain constant. As this was not the case, an exact steady state was impossible to attain. For the purposes of this thesis, we consider that a *quasi-steady state* would be reached, if within two hours no recorded thermocouple reading would vary by more than 0.5 K. Figure 78 shows the same data as Figure 77, but with the values found to satisfy the *quasi-steady state* condition highlighted.

All recorded temperatures that did not satisfy the aforementioned conditions for *quasi-steady state* were initially rejected. After any change in wall heat flux or eccentricity took place, there was an initial transition period in which the *quasi-steady state* is disturbed and the annulus temperature moves towards a new *quasi-steady state* under different wall temperature conditions. After this new *quasi-steady state* is reached for the first time (as indicated by the first set of highlighted points in Figure 78), cyclic variations in the room temperature lead to a violation on the conditions set for steady-state. Because we have seen that, after complying with the steady-state conditions, the annulus temperature varies directly with the room temperature, it was decided that we should not dismiss recorded temperature readings which do not strictly adhere to the imposed conditions of steady-state. As a result, we consider that *quasi-steady state* exists from the first initial adherence to the conditions until a change is done to the setup.

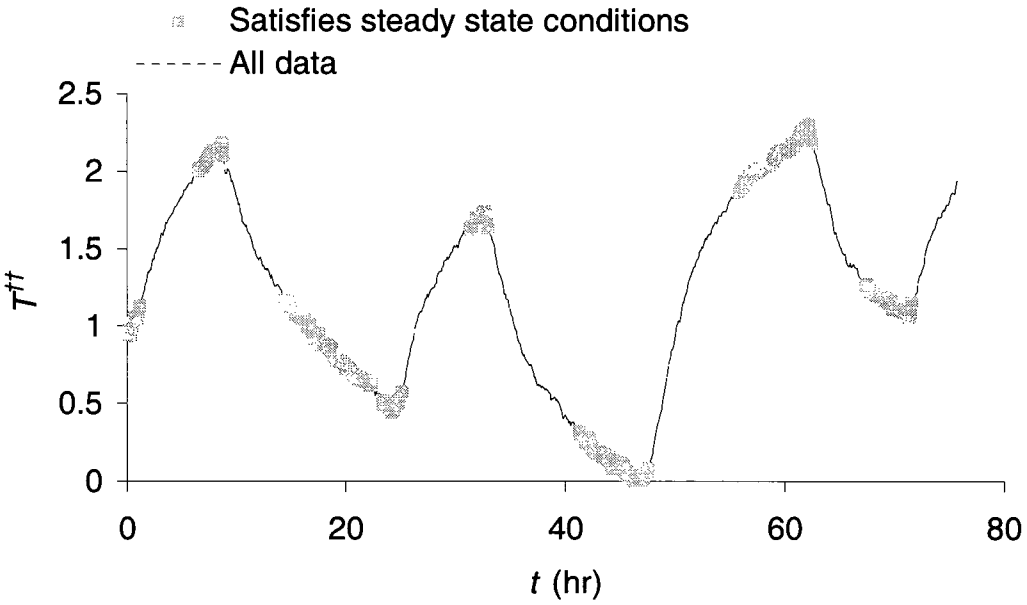

Figure 78 – Average annulus wall temperature variation; time periods during which *quasi-steady state* conditions are met have been highlighted; $q'' = 80$ W/m^2 and $e = 0.5$

8.1.2 End losses

As was discussed in a previous chapter, radiation to the surroundings and other end effects resulted in significant decreases of the wall temperature near the annulus ends. It was also noticed that, away from these ends, the wall temperature increased approximately linearly with distance from the inlet. Because it was difficult to correct for end effects, we have decided to base the present study of natural convection only on the measurements in the middle section of the annulus. To determine the minimum distance from the ends beyond which measurements should be retained, we have plotted in Figure 79 the changes in the average temperatures along the middle parts of the inner and outer cylinders of the annulus, computed from thermocouple readings from which an increasing number near the ends has been disregarded. A concentric case with a heat flux of 80 W/m^2 was considered as representative. The 16 planes of the thermocouples have been numbered such that 0 corresponds to those closest to the inlet and 15 to those closest to the outlet. As can be seen in this figure, the differences between the temperatures computed by averaging all thermocouple (0-15) readings and those computed by averaging only those closest to the mid-section (7-8) were 1.8 K for the outer cylinder and 1.4 K for the inner cylinder, which proves that end effects can affect the average temperature significantly. The same figure also shows that both averages where essentially the same when only thermocouples 5-10, 6-9 and 7-8 were taken into consideration.

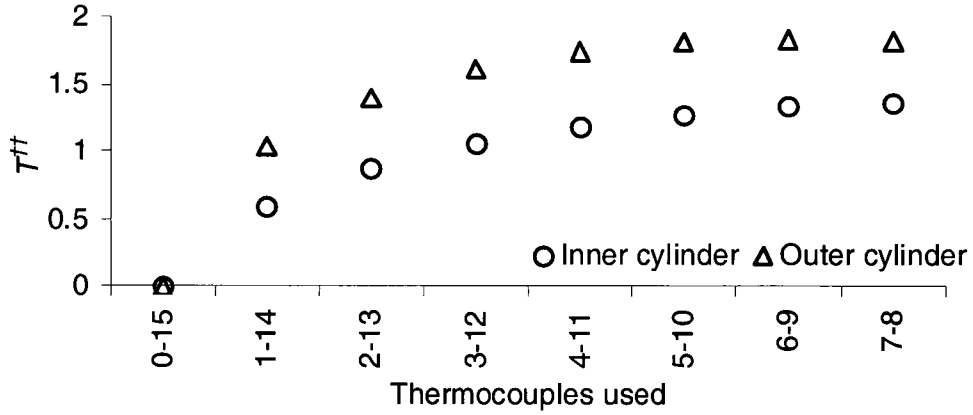

Figure 79 – Changes of the average wall temperatures of the inner and outer cylinders when different numbers of thermocouples are considered; $q'' = 80$ W/m^2 and $e = 0.5$

Radiation losses from the ends are expected to increase with increasing eccentricity, because the space between the cylindrical core and the surrounding cavity would increase on one side of the annulus, allowing more radiation to escape. This is confirmed by the results shown in Figure 80.

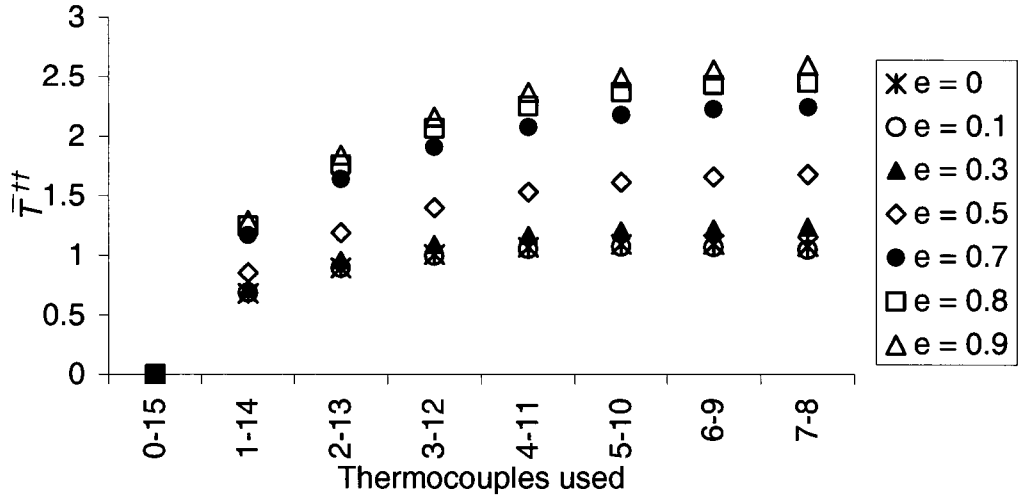

Figure 80 – Changes of the overall average wall temperature of the annulus when different numbers of thermocouples are considered for different eccentricities; $q'' = 80$ W/m^2

In Figure 80, we see that at higher eccentricities there may still be a very small effect of radiation at the 7-8 thermocouple boundaries. In order to use as many thermocouples as possible while still being able to consider that radiation end-effects were negligible, it was decided that a suitable thermocouple boundary would be that between thermocouple positions 5 and 10.

8.1.3 Wall conduction

Because the exterior of the apparatus and the core of the inner cylinder were well insulated, the corresponding conduction losses have been assumed to be negligible. Moreover, because the foil is very thin and the wall temperature gradient is relatively small conduction within the foil will be very small.

To estimate the conduction heat transfer rate through the foil axially and azimuthally, we considered a section of the outer cylinder between two thermocouple planes having a wall heat flux of 80 W/m^2 and an eccentricity of 0.9. We used actual temperature variations obtained in our experiments to determine the conduction heat transfer taking place in the stainless steel foil. The thermal conductivity of stainless steel 304 at 300 K is 14.9 W/m K (Incropera and DeWitt, 2005). For a foil of thickness 5.08×10^{-5} m, a width of 0.26 m (equivalent to the circumference of the outer cylinder) having an average temperature difference of 2°C measured between two thermocouple planes 10 cm apart, the axial conduction heat transfer rate is

$$q_z = -\frac{kA\Delta T}{l} = \frac{14.9 \times \left[0.26 \times 5.08 \times 10^{-5}\right] \times 2}{0.1} \approx 15\,\text{mW}$$

The azimuthal conduction heat transfer rate, for a foil of length 10 cm and maximum temperature difference between adjacent sides of 11°C is

$$q_\theta = 2\left(-\frac{kA\Delta T}{l}\right) = 2\times\left(\frac{14.9\times\left[0.1\times 5.08\times 10^{-5}\right]\times 11}{0.26/2}\right) \approx 13\,\text{mW}$$

The convection heat rate in the 10 cm section of the annulus which would lead to a rise of 2°C in the air temperature is calculated as

$$q_{convection} = \dot{m}c_p\Delta T = 0.0016\times 1012\times 2 = 3.2\,\text{W}$$

Comparing the conduction heat transfer through the foil to the convection heat transfer from the surface of the foil, we find that the rate of conduction heat transfer is less than 0.5% of that of convection. Therefore, the axial and azimuthal heat conduction from warmer to cooler parts of the foil can be neglected.

At the ends of the annulus, heat may be conducted through the metal supports of the inner and outer cylinders and then transferred by convection into the surroundings. The apparatus was constructed such as to keep these losses as low as possible, although any estimates of them are likely to be quite uncertain. In any case, these losses would contribute to the end effects which have been avoided by only considering readings in the mid-section of the apparatus.

8.1.4 Radiation losses

One of the main reasons for heating both the inner cylinder and the surrounding cavity to approximately the same temperature was to reduce the effect of radiation on the heat transfer in the annulus, thus allowing the study of the effect of eccentricity on

convection heat transfer with as little interference from other phenomena as possible. Moreover, heating both walls also seemed to eliminate the backflow near a cold wall at the exit of the annulus which we observed in experimental runs having only the inner cylinder heated. This flow reversal has been observed in similar experiments, for example those done by Sparrow et al. (1984), in an open ended vertical rectangular channel with one wall unheated. At the ends of the annulus, however, losses due to radiation are unavoidable.

To estimate these losses, we considered the view factors for the outer cylinder with the inner cylinder and with itself. The sum of these two view factors is a measure of the radiation energy emitted by the surface of the outer cylinder which is either intercepted by the inner cylinder or other parts of the outer cylinder. The remaining radiation energy is considered to be lost to the surroundings. The surroundings absorb and reemit radiation, so emitted radiation from the surroundings also enters the annulus from the ends. The sum of the two view factors for the outer cylinder, computed using equations 20 and 21, presented in section 4.3.3 for concentric annuli with different aspect ratios $z^{\dagger}$ has been plotted in Figure 81. The aspect ratio is defined as the ratio of the height of the annulus to the outer cylinder diameter.

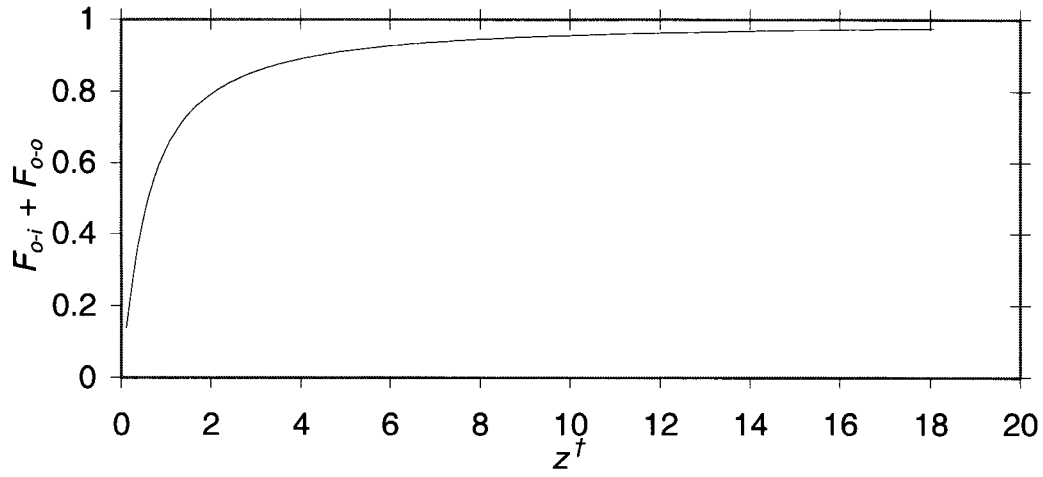

Figure 81 – $(F_{o-i} + F_{o-o})$ versus aspect ratio height for concentric annuli with the same diameter ratio as our setup

The difference between unity and the view factor, called the complementary view factor, represents radiation losses to the surroundings. The percentage of the total radiation energy emitted by the outer cylinder which is lost to the surroundings can be expressed as

$$[1-(F_{0-i}+F_{o-o})]\times 100\% \tag{63}$$

If we consider each end of the annulus separately, then the complementary view factor at each end would be equal to half of the total complementary view factor. From the above equation and Figure 81 we can see that radiation losses at the ends of the annulus are much more significant than those towards the central region. For the present geometry, we find that only 2.5% of the total radiation emitted from the outer cylinder leaves the annulus and that the majority of this occurs near the ends.

In the absence of radiation losses and other end effects, as will be discussed, one would expect the azimuthally averaged wall temperature in the thermally fully developed flow region of the annulus to increase linearly with distance from the inlet. Because of end effects, deviations from linearity were observed. To explore this point further, Figure 82 compares two plots for the outer cylinder in the concentric case with $q'' = 80$ W/m^2. The first plot is that of the difference between an idealized, linearly increasing, average wall temperature $\overline{T}_L$ and the measured average wall temperature $\overline{T}$ vs. non-dimensionalized distance from the inlet. The second plot is that of one half the complementary view factor for the outer cylinder versus the aspect ratio.

The one half complementary view factor plotted in Figure 82 represents the amount of radiation energy which leaves the surface of the outer cylinder and exits the annulus from the top section. For an infinitesimally short annulus, approximately half of all the radiation leaving the surface of the annulus will be lost from each side. Applying this to our setup, and considering only the very end of the annulus, or an infinitesimally small height at the end of the annulus ($z^\dagger = 0$; $z^* = 1$), half the radiation leaving this section will be lost, while the other half will be projected back into the annulus. Now if we consider an aspect ratio $z^\dagger = 8.43$ (corresponding to the area between $z^* = 0.53$ and $z^* = 1$), only 2.6% of the radiation energy is lost from the top of the annulus. It can be seen that there is some qualitative agreement between the temperature difference variation and the radiation loss variation, which suggests that the majority of the losses at the exit are likely due to radiation.

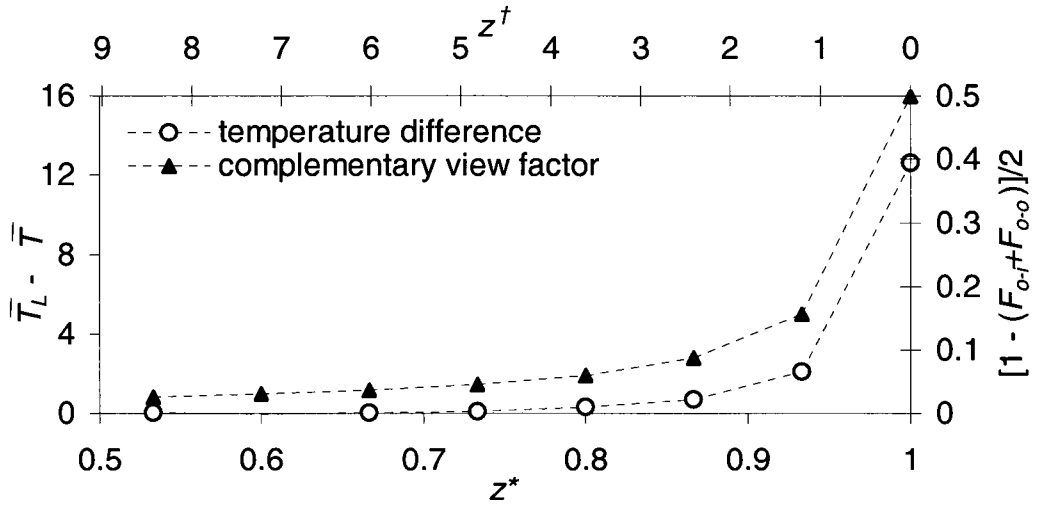

Figure 82 – Radiation effects for the outer cylinder and temperature difference from idealized case versus $z^{\dagger}$ and z* respectively for $q'' = 80$ W/m^2 and e = 0

As we increase the eccentricity, the wider gap between the inner and the outer cylinders increases as well and as a result the corresponding surfaces would become more susceptible to heat losses due to radiation. Figure 83 demonstrates the variation between the idealized average wall temperature and the actual average wall temperature. This figure shows that indeed radiation losses increase with increasing eccentricity.

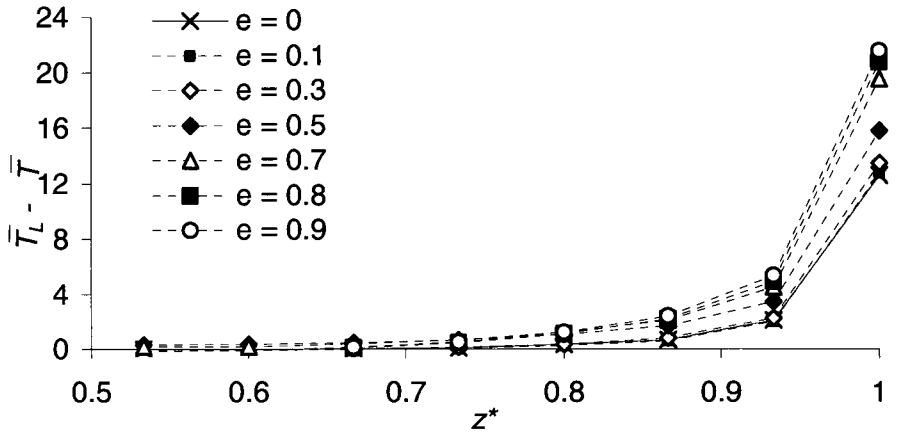

Figure 83 – Comparison of end effects on wall temperature for different eccentricities

Quantitatively, we have expressed the effect of eccentricity on the end effects by comparing the deviation from linearity for the concentric case with that for the set of eccentric cases. We defined the difference in the percentages of deviation as follows

$$P_R = \left[\left| \frac{T_L - T}{T_L} \right| - \left| \frac{T_L - T}{T_L} \right|_{e=0} \right] \times 100 \tag{64}$$

Table 14 shows P_R for selected eccentricities and non-dimensional heights. One should keep in mind the uncertainty in temperature measurements when looking at this table, especially for very small values of P_R. In the broad sense, we can see that end effects increase with increased eccentricity, although they remain very small near the center of the annulus.

Table 14 – End effect variation with eccentricity

	e					
	0.1	**0.3**	**0.5**	**0.7**	**0.8**	**0.9**
z*	**P_R [%]**					
0.53	0.02	0.08	0.51	0.28	0.27	0.28
0.60	0.02	0.08	0.55	0.26	0.19	0.18
0.67	0.07	0.06	0.76	0.55	0.08	0.12
0.73	0.10	0.02	1.00	0.94	0.55	0.65
0.80	0.17	0.02	1.15	1.30	1.06	1.25
0.87	0.21	0.10	1.47	1.96	2.02	2.33
0.93	0.26	0.09	1.72	3.01	3.54	4.13
1.00	0.29	0.35	2.79	6.92	8.39	9.39

8.1.5 Mean wall and fluid temperature analysis

For steady flow, the mass flow rate through any cross-section of the annulus is

$$\dot{m} = \rho_{in} \overline{V}_{in} \left(\frac{\pi}{4} \left(D_o^2 - D_i^2 \right) \right) \tag{65}$$

where $\overline{V}_{in}$ and ρ_{in} are the average velocity and density of the fluid at the inlet of the annulus.

Consider a control volume (CV) in the annulus bounded by two horizontal planes with distance δz. From the first law of thermodynamics for steady flow through this CV and considering that the fluid in the CV does not produce any work, the flow is adiabatic and air may be treated as an ideal gas, one gets

$$\dot{m} c_p \delta T_m = q'' \pi (D_o + D_i) \delta z \tag{66}$$

where δT_m is the change in the mean temperature of the air within the CV. In the limit of vanishing height of the CV, one may compute the mean fluid temperature gradient as

$$\frac{dT_m}{dz} = \frac{4q''}{\rho_{in} \overline{V}_{in} c_p (D_o - D_i)} \tag{67}$$

Assuming c_p to be constant, and for a constant wall heat flux, the mean fluid temperature gradient in the annulus would also be constant. Equation 67 can be re-written as

$$\frac{dT_m}{dz} = \frac{4h(T_w - T_m)}{\rho_{in} \overline{V}_{in} c_p (D_o - D_i)} = \text{constant} \tag{68}$$

Both the left and right hand sides of equation 68 are constant and independent of z, therefore, if we integrate from the inlet to any height z in the annulus, we get the mean fluid temperature as

$$T_m(z) = T_{m-in} + \left[\frac{4h(T_w - T_m)}{\rho_{in} \overline{V}_{in} c_p (D_o - D_i)} \right] \tag{69}$$

where T_{m-in} is the mean fluid temperature at the inlet of the annulus. Therefore, the mean fluid temperature in the annulus varies linearly with z. As explained by Incropera and DeWitt (2005), for a *thermally fully developed* flow[7] of a fluid with constant properties, the local heat transfer coefficient is constant and independent of z. Accordingly, in the *thermally fully developed* regions of the annulus, we expect $T_w - T_m$ to be independent of z. The presence of such a region in the present test section is illustrated by the results in Figure 84.

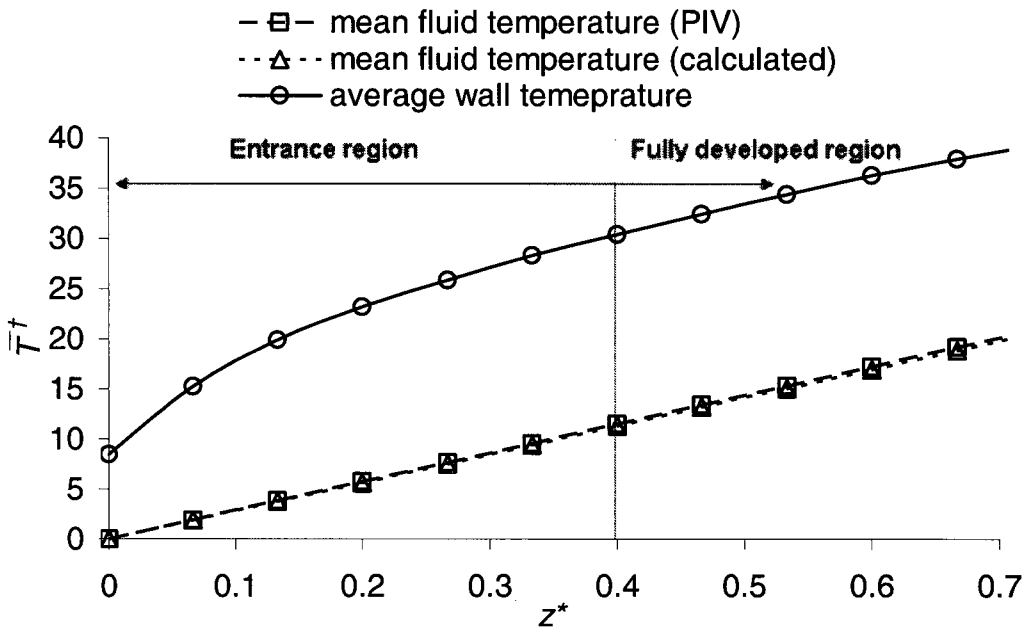

Figure 84 – Mean wall and mean fluid temperature variations for $q'' = 80$ W/m^2 and e = 0.9[8]

---

[7] *Thermally fully developed* flow in a pipe is defined by Incropera and DeWitt (2005) as the region of the flow where an appropriately non-dimensionalized radial profile of temperature is independent of axial distance.

[8] In Figure 84, we chose to present the highly eccentric case because of the relatively small difference between the measured (PIV) and calculated mass flow rate.

8.2 Effect of eccentricity on the heat transfer coefficient

The average convection heat transfer coefficient $\overline{h}$, computed from equation 9 using the mean wall and fluid temperature difference $T_w - T_m$ in the central region of the annulus, is presented in Figure 85. At low eccentricities, the effect of e on $\overline{h}$ appears to be small. As eccentricity is increased, however, there is a significant monotonic decrease in $\overline{h}$. For $q'' = 30$ W/m^2, the convective heat transfer coefficient in the concentric case is nearly twice that for the highly eccentric case at e = 0.9. For $q'' = 80$ W/m^2, $\overline{h}$ for the concentric case is 1.6 times that of the highly eccentric case at e = 0.9. Moreover, this figure shows that increasing q'' increases the convective heat transfer.

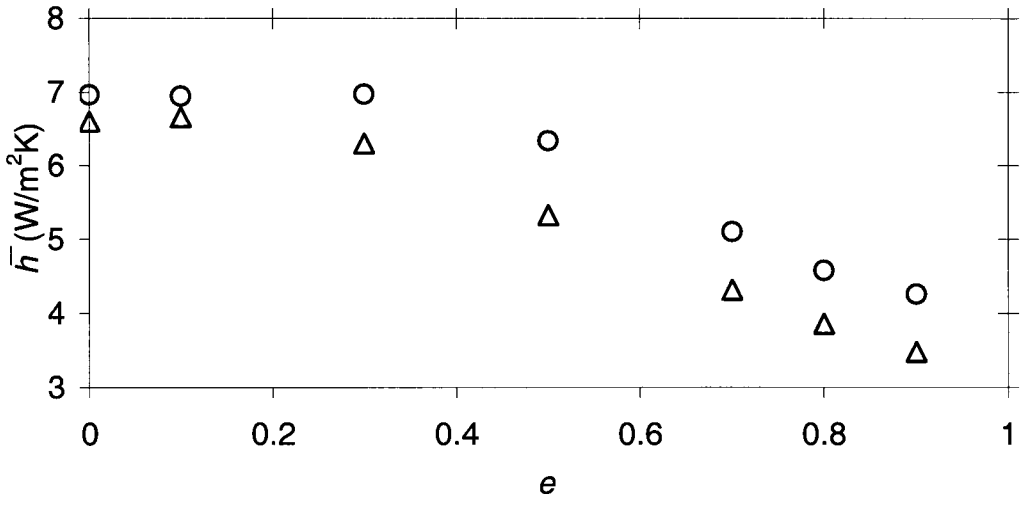

Figure 85 – $\overline{h}$ vs. e for $q'' = 30$ W/m^2 (△) and $q'' = 80$ W/m^2 (○)

To gain further understanding of the dependence of natural heat convection upon the eccentricity, we have plotted the azimuthal variations of the local convection heat transfer

coefficient at a height of $z^* = 0.5$ in Figure 86 and Figure 87. As can be seen in these figures, at low eccentricities, a decrease in the local convection heat transfer coefficient at position 1 where the two cylinders are the closest to each other is compensated for by an increase in the local convection heat transfer coefficient at position 3 where the two cylinders are the farthest apart. As a result, the average heat transfer coefficient appears to remain constant. As eccentricity is further increased, a general decrease in the local convection heat transfer coefficient in the entire annulus is observed.

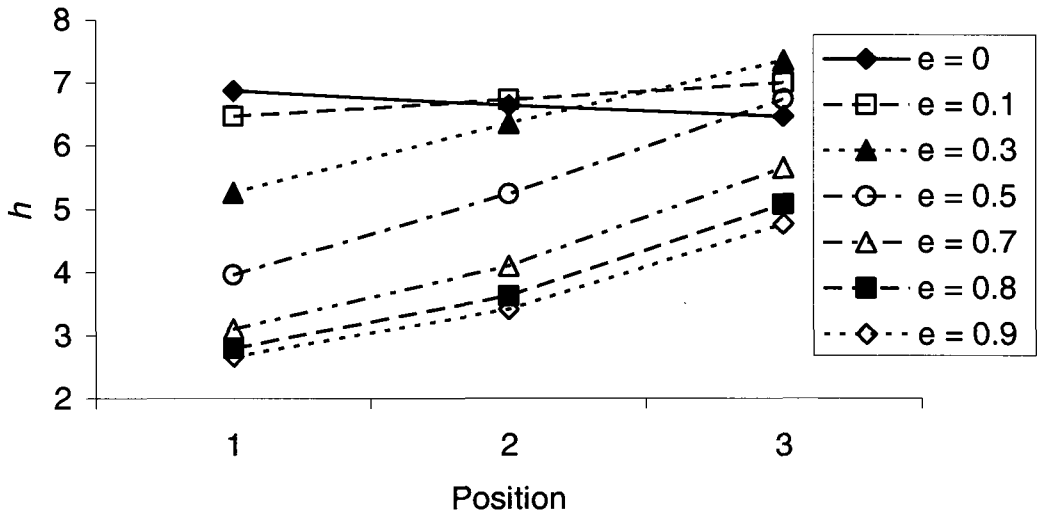

Figure 86 – Azimuthal variation of the local heat flux coefficient; $q'' = 30$ W/m^2 and $z^* = 0.5$

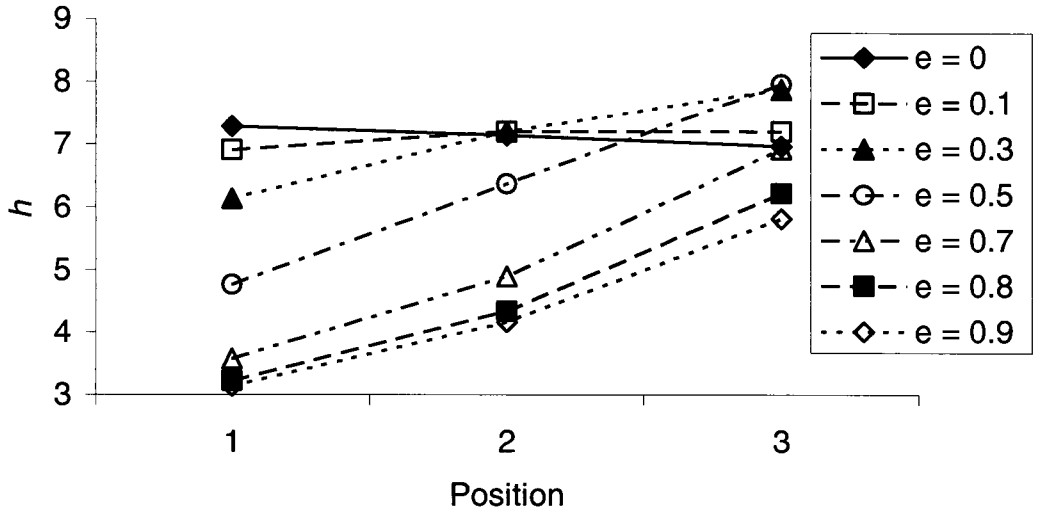

Figure 87 – Azimuthal variation of the local heat flux coefficient; $q'' = 80$ W/m^2 and $z^* = 0.5$

Figure 88, 89 and 90 present the axial variations in the local convection heat transfer coefficient for the three thermocouple positions at eccentricities of 0, 0.5 and 0.9 respectively and for a wall heat flux of 30 W/m^2. Figure 91, 92 and 93 present the axial variations of the local convection heat transfer coefficient for the aforementioned eccentricities and for a wall heat flux of 80 W/m^2.

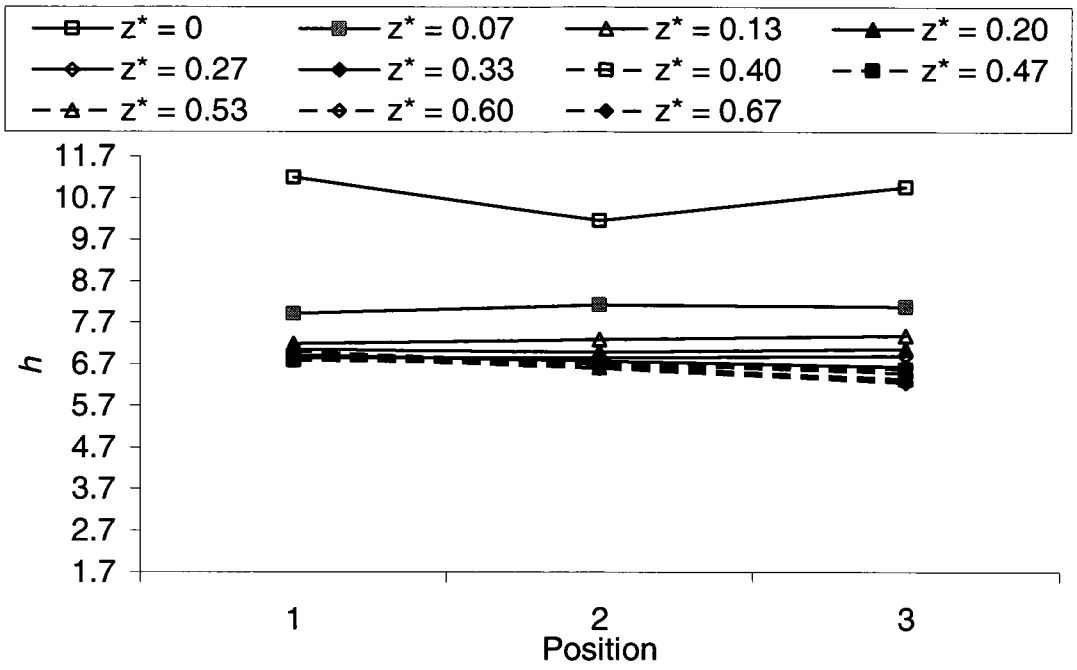

Figure 88 – Axial variation of the local heat flux coefficient for e = 0 and $q'' = 30$ W/m^2

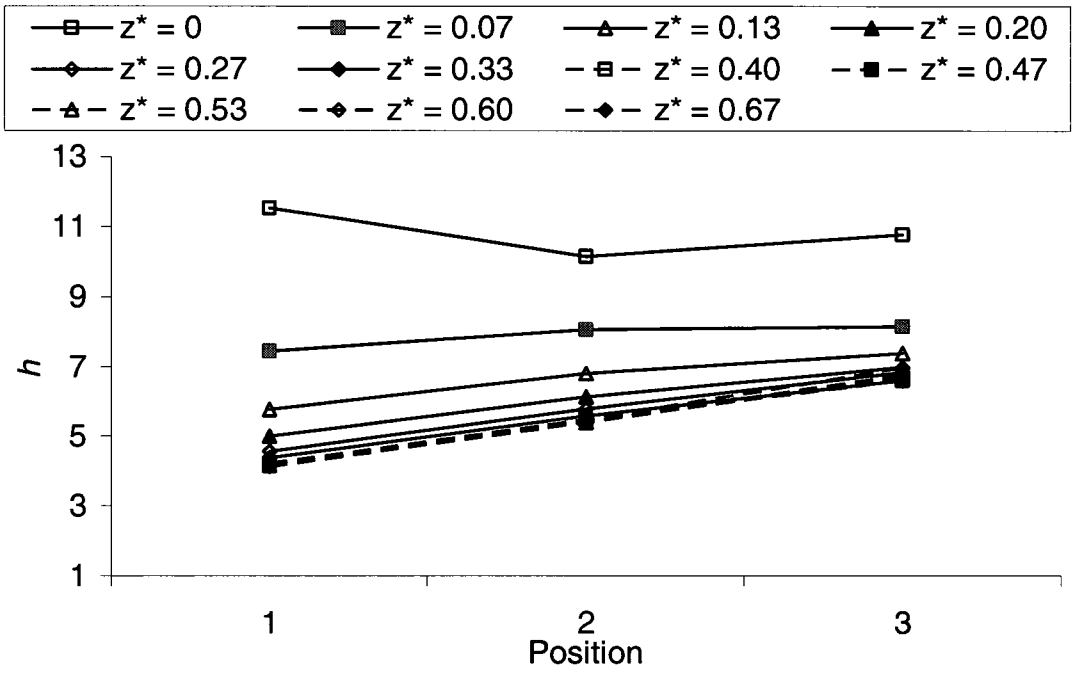

Figure 89 – Axial variation of the local heat flux coefficient for e = 0.5 and $q'' = 30$ W/m^2

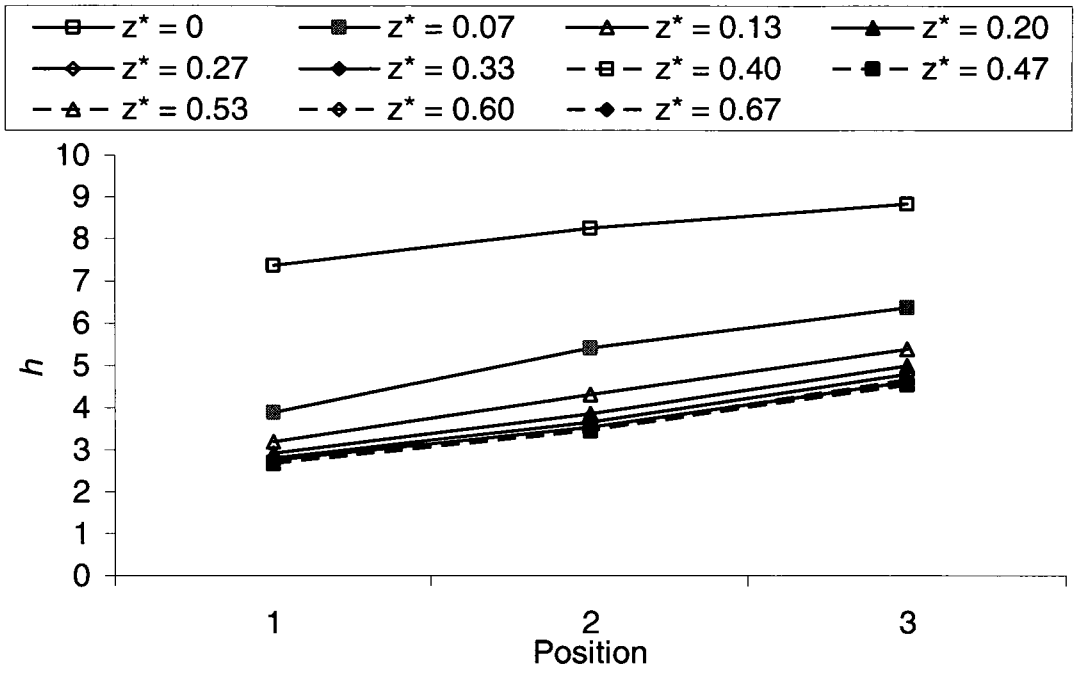

Figure 90 – Axial variation of the local heat flux coefficient for e = 0.9 and $q'' = 30$ W/m^2

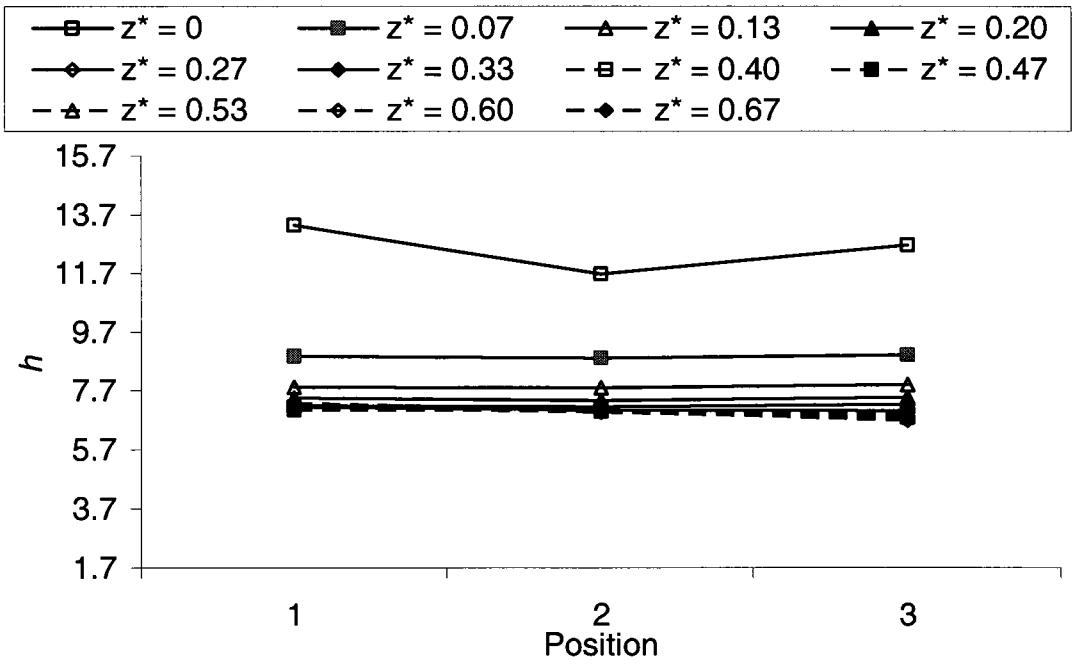

Figure 91 – Axial variation of the local heat flux coefficient for e = 0 and $q'' = 80$ W/m^2

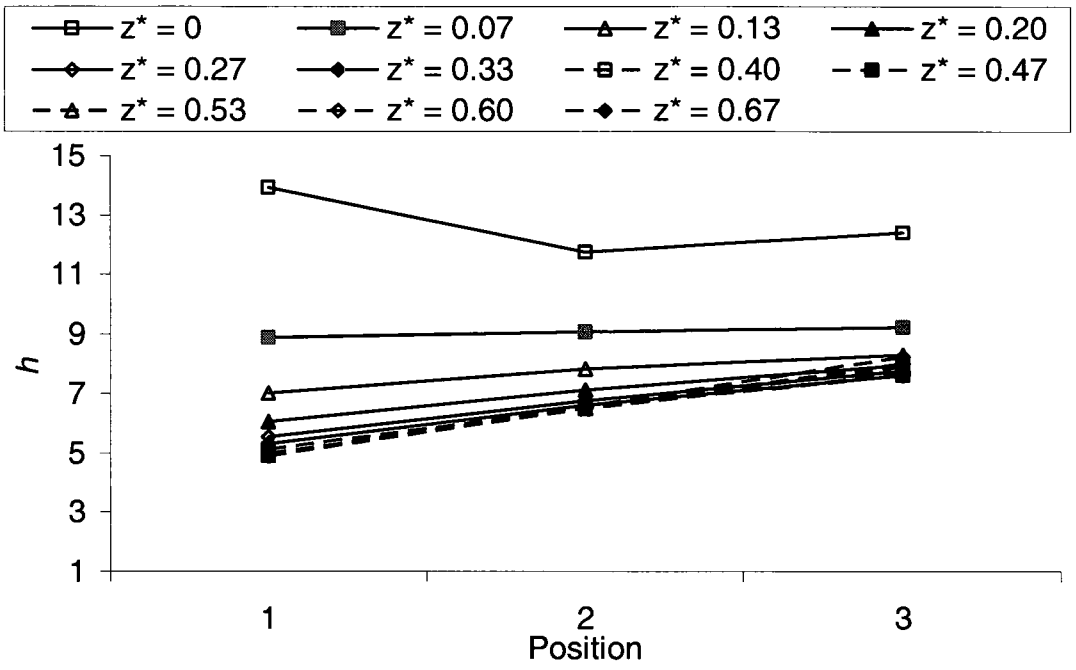

Figure 92 – Axial variation of the local heat flux coefficient for e = 0.5 and $q'' = 80$ W/m^2

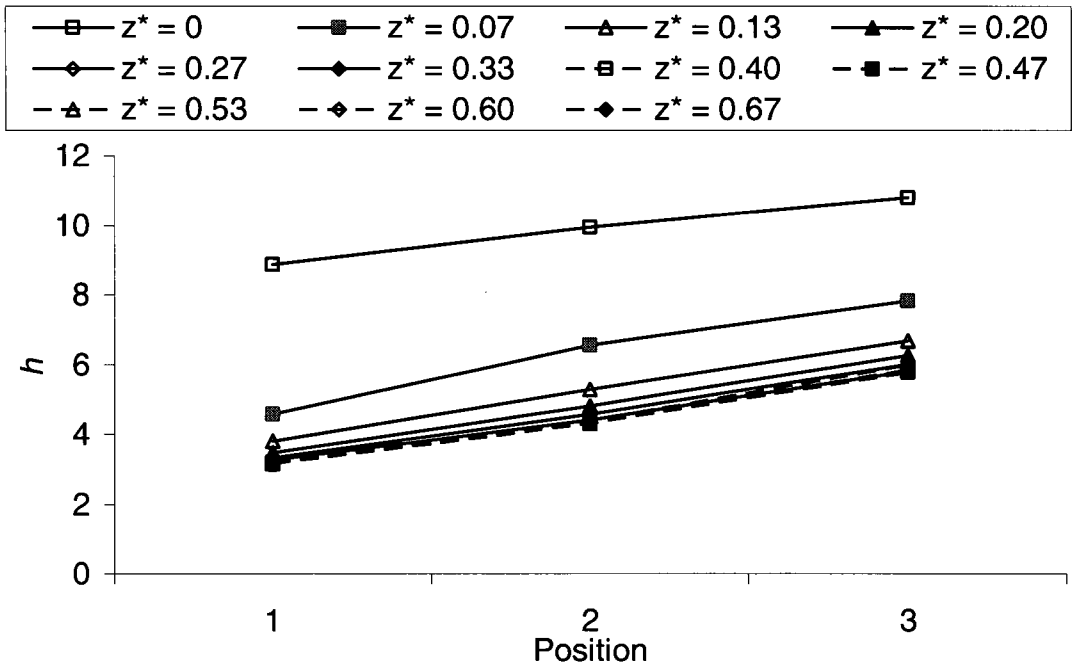

Figure 93 – Axial variation of the local heat flux coefficient for e = 0.9 and $q'' = 80$ W/m^2

The axial variation of the average convection heat transfer coefficient $\overline{h}$, shown in Figure 94 and 95, is consistent with the presence of a thermally fully developed flow in the approximate range $0.35 < z^* < 0.65$ for all eccentricities.

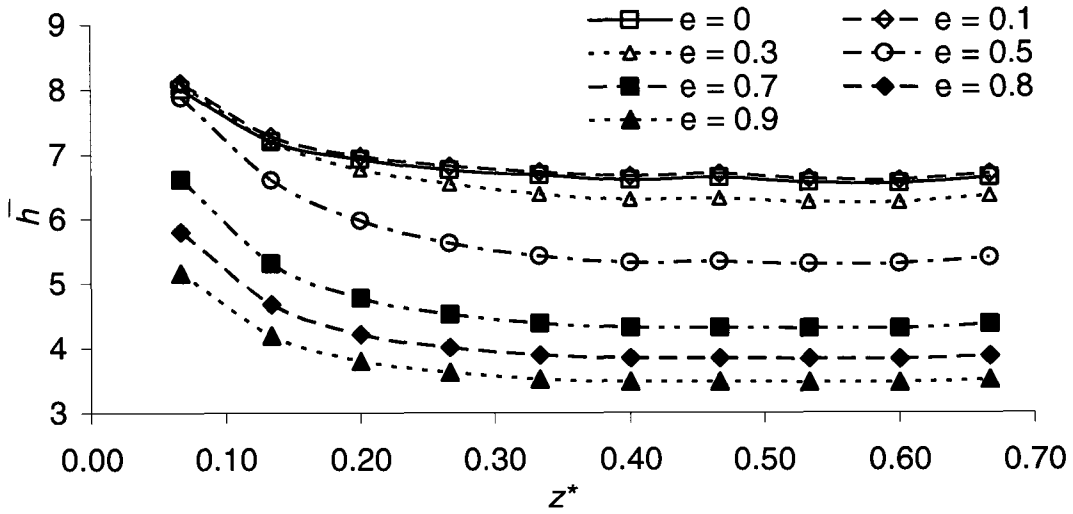

Figure 94 – Axial variation of $\overline{h}$ for $q'' = 30$ W/m^2

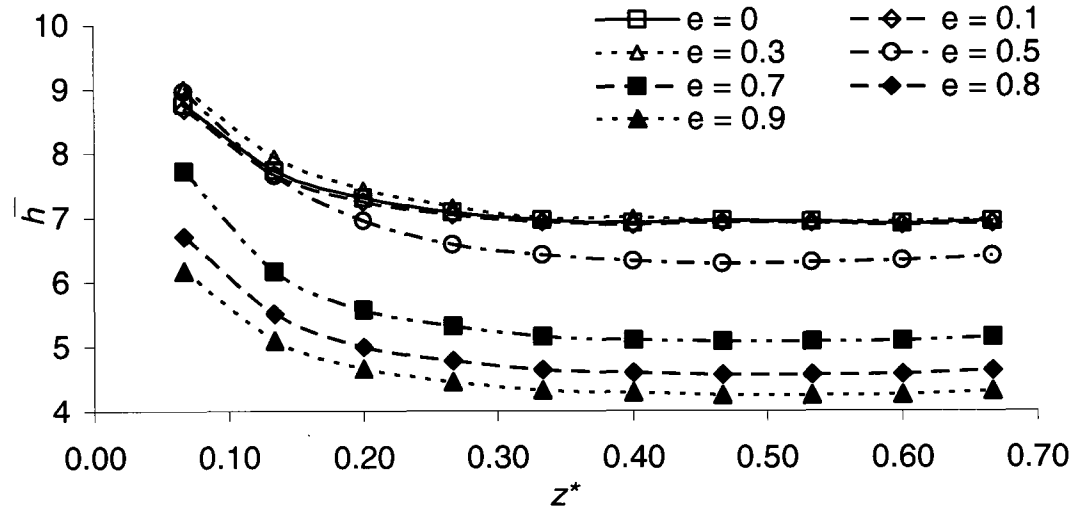

Figure 95 – Axial variation of $\overline{h}$ for $q'' = 80$ W/m^2

8.3 Effect of heat flux on dimensionless groups

In our experiment, the heat flux is the driving force for the fluid motion and its magnitude should have a direct effect on the flow. Two heat flux values were considered in the present work. A dimensionless heat flux definition that is independent of the eccentricity and other variables as well as independent of changes of properties along and around the annulus is

$$q''^{*} = q'' \frac{D_h}{k_{in} T_{in}} \tag{70}$$

Figure 96 shows the effects of dimensionless heat flux on the Nusselt number for different eccentricities. For the lowest eccentricities of 0 and 0.1, the Nusselt number seems to be insensitive to the heat flux within the examined range, however, at higher eccentricities, the Nusselt number increases with heat flux at a rate that increases with eccentricity. Even so, the effect is relatively weak.

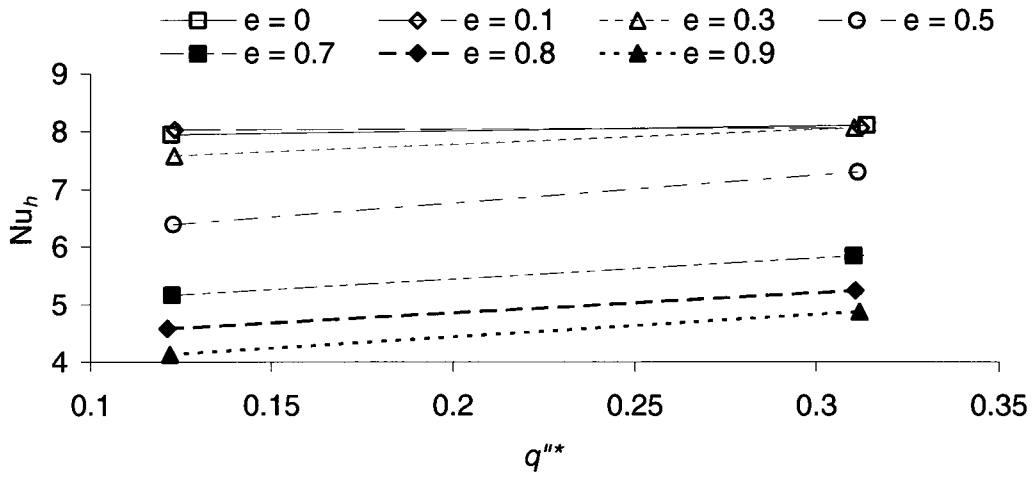

Figure 96 – Nusselt number versus dimensionless heat flux

Figure 97 shows the effect of the dimensionless heat flux on the Grashof number. For all eccentricities, an increase in the heat flux increases significantly the Grashof number. This was to be expected, considering that the relative importance of buoyancy forces with respect to viscous forces increases with increasing heat flux. However, the dependence is not proportional, as an increase in heat flux by a factor of 2.7 resulted in Grashof number increases between 2.2 for $e = 0$ and 1.9 for $e = 0.8$.

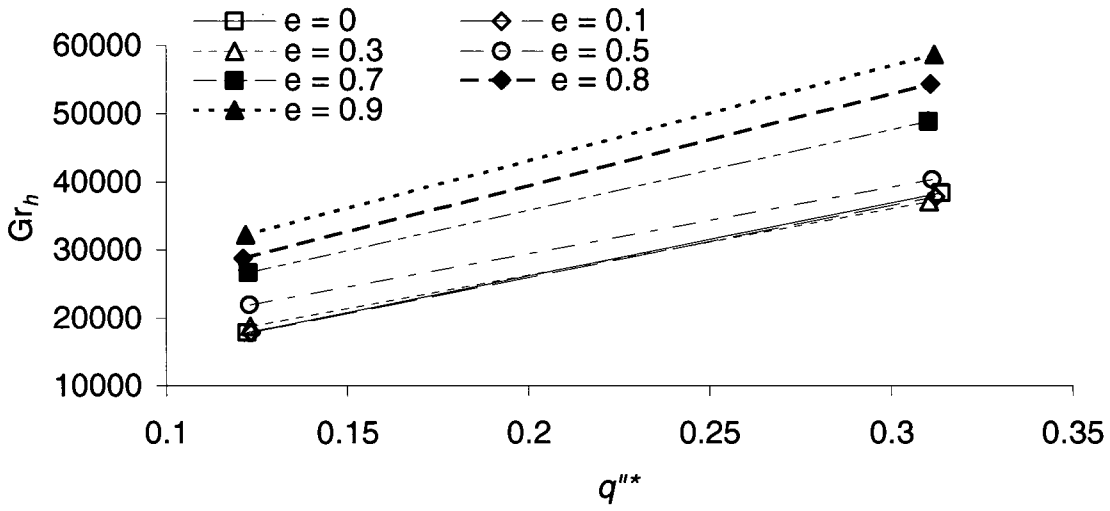

Figure 97 – Grashof number versus dimensionless heat flux

Figure 98 presents the effect of heat flux on the Rayleigh number. It shows that the dependence of the Rayleigh number on heat flux is similar to that of the Grashof number.

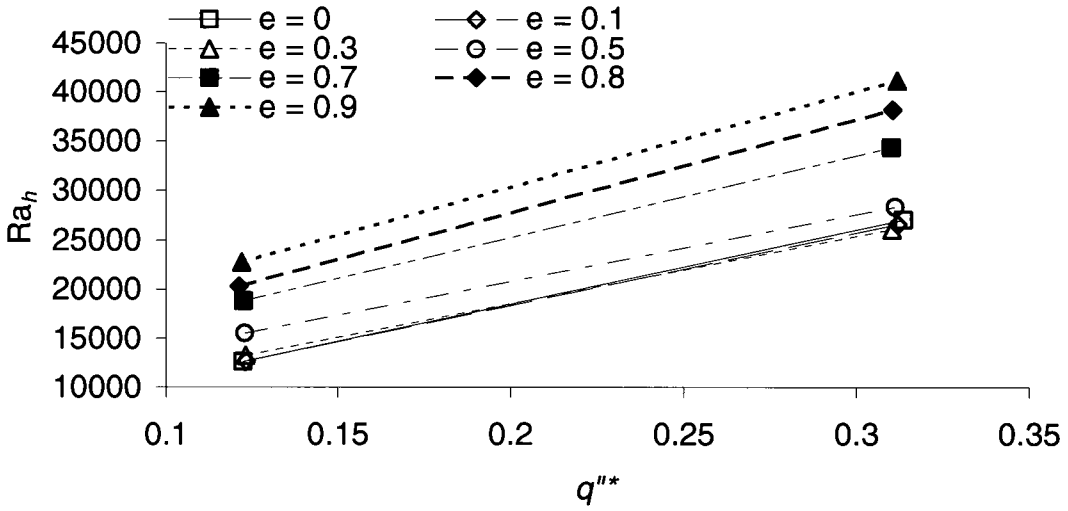

Figure 98 – Rayleigh number versus dimensionless heat flux

A different method of non-dimensionalizing the heat flux is to use properties that depend on the flow and heat transfer taking place. One way is to use the mass flow rate, the specific heat capacitance and the average wall temperature difference in the central part of the annulus as follows

$$q''** = q''\frac{D_h^2}{\dot{m}c_p(T_w - T_m)} \tag{71}$$

In Figure 99 we plotted the two dimensionless heat fluxes against one another for different eccentricities. In this figure we see that at the lower heat flux, for small eccentricities, the effect is more significant than that at higher eccentricities. At higher eccentricities, the effect introduced by varying the heat flux decreases. This is the opposite of what was observed in the heat flux coefficient and Nusselt number, on which at low eccentricities the heat flux had a lesser effect.

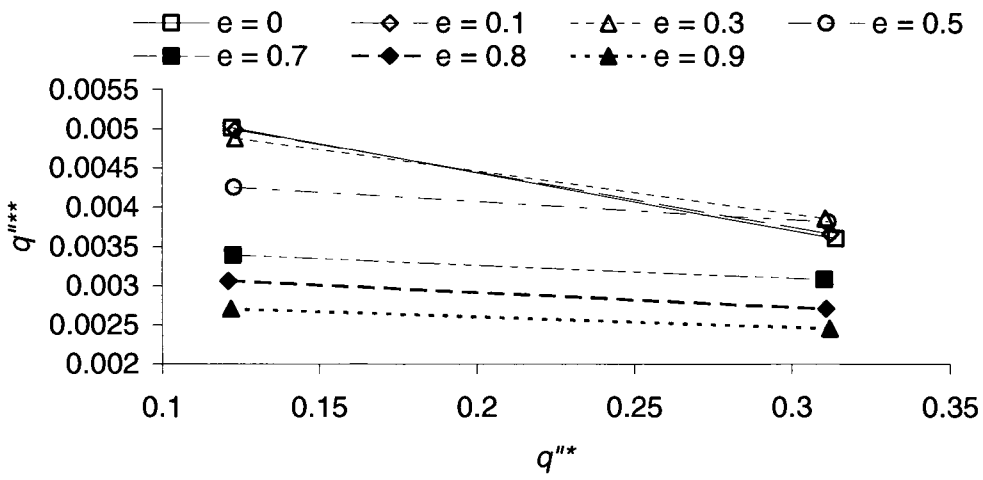

Figure 99 – Two dimensionless heat fluxes plotted against one another

The effect of varying the heat flux on the mass flow rate is presented in Figure 100. It is clear that a higher wall heat flux leads to a higher mass flow rate. The results also indicate that the mass flow rate generally decreases with increasing eccentricity, although there is considerable scatter and this effect is relatively mild.

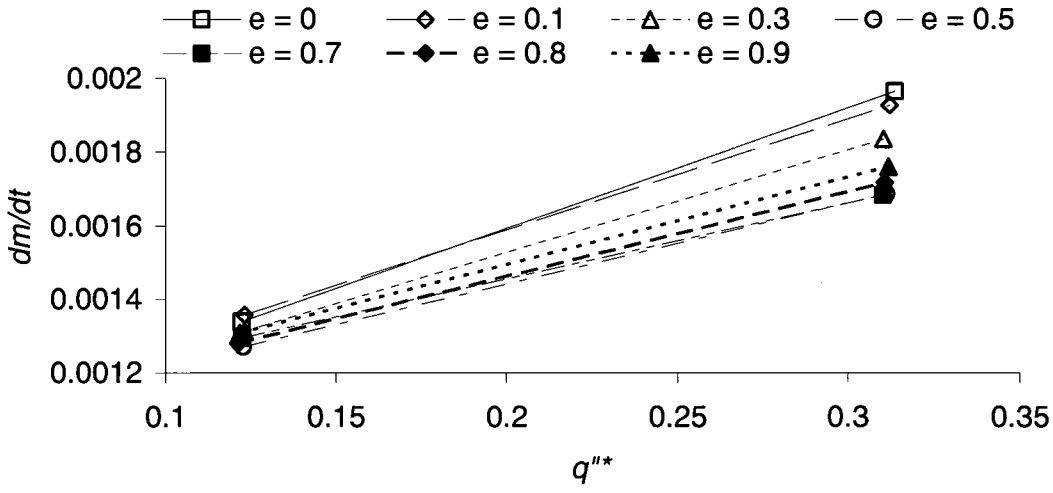

Figure 100 – Variation of the mass flow rate with dimensionless heat flux for different eccentricities

The mass flow rate is proportional to the Reynolds number, which may be defined as

$$\mathrm{Re} = \frac{\dot{m}}{D_h \mu} \tag{72}$$

This expression shows that the Reynolds number would decrease slowly with height along the annulus, due to the corresponding increase in the viscosity of air. The Reynolds number at the inlet of the annulus has been plotted vs. the dimensionless wall heat flux in Figure 101. It increases with increasing heat flux and generally decreases with increasing eccentricity. Its values are between 2900 and 4600, which overlaps with the transitional range of flows through pipes. Although we have no direct evidence to support this claim, it seems that the flow in the concentric annulus and at low eccentricities could be transitional at the lower heat flux and turbulent at the higher heat flux. At high eccentricities, it is possible that the flow in the narrow gap could even be laminar, whereas in the wide gap the probability of turbulence would increase compared to the concentric case. This is consistent with the observations by Gosset and Tavoularis (2006); moreover, simulations by Ninokata at al. (2009) for an eccentric annulus with a diameter ratio of 0.5, e = 0.5 and Re = 3,200 showed that transition to turbulence was delayed in the narrow region.

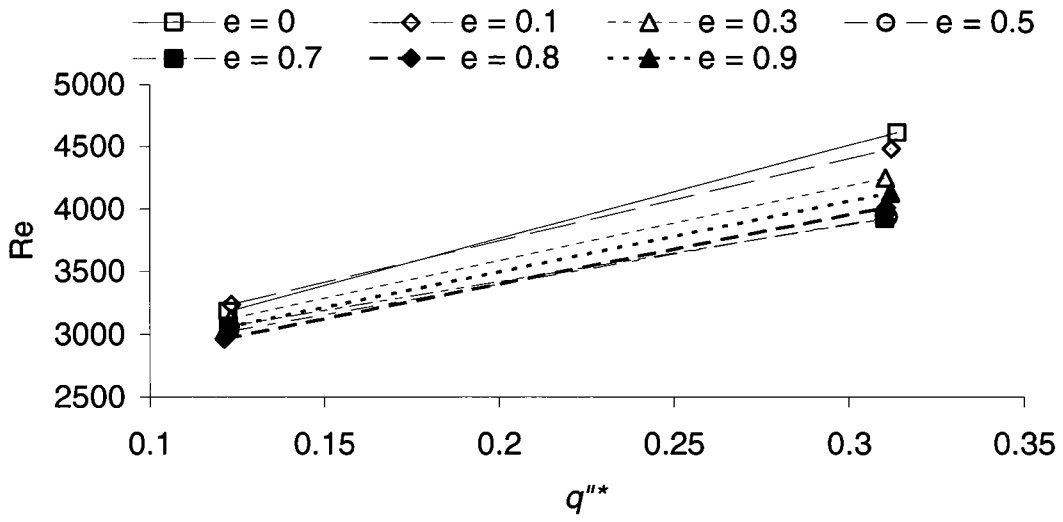

Figure 101 – Variation of Re at the inlet with dimensionless wall heat flux for different eccentricities

8.4 Effect of eccentricity on dimensionless groups

Figure 102 shows the variation of Nusselt number with eccentricity. This graph clearly illustrates that natural convection is weakened monotonically by increasing eccentricity, although, for very low eccentricities, the sensitivity of the Nusselt number to eccentricity seems to be negligible. As with the convection heat transfer coefficient, increasing the heat flux appears to extend the range of insensitivity to eccentricity for the overall Nusselt number.

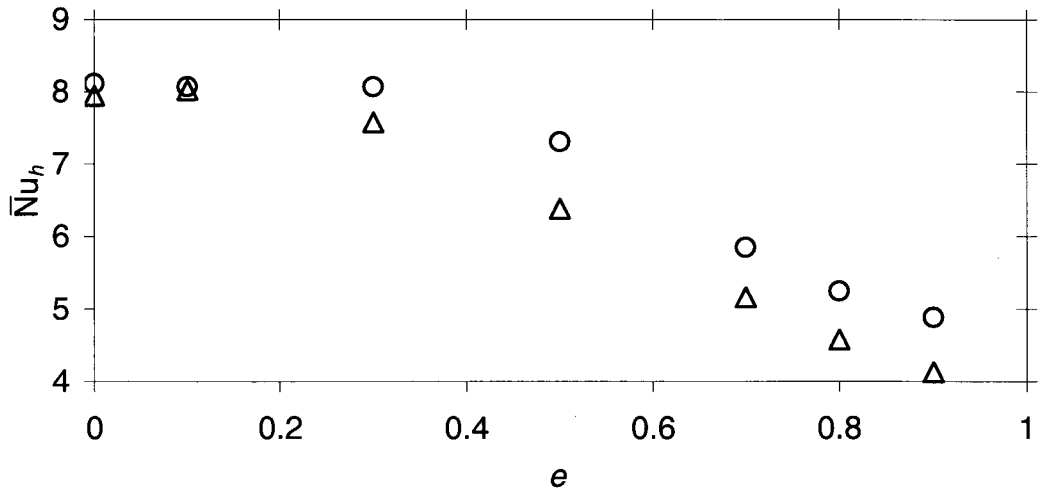

Figure 102 – Average Nusselt number vs. e for $q'' = 30$ W/m^2 (△) and $q'' = 80$ W/m^2 (○)

Figure 103 and 104 present azimuthal variations of the Nusselt number for different eccentricities at a height of $z^* = 0.5$. The Nusselt number variation is very similar to that of the convection heat transfer coefficient, which was discussed in a previous section. The numerical value of this Nusselt number is not of particular significance, because it depends on the choice of length scale; for example, if the hydraulic radius of the annulus were chosen instead of the hydraulic diameter, this value would have been four times smaller.

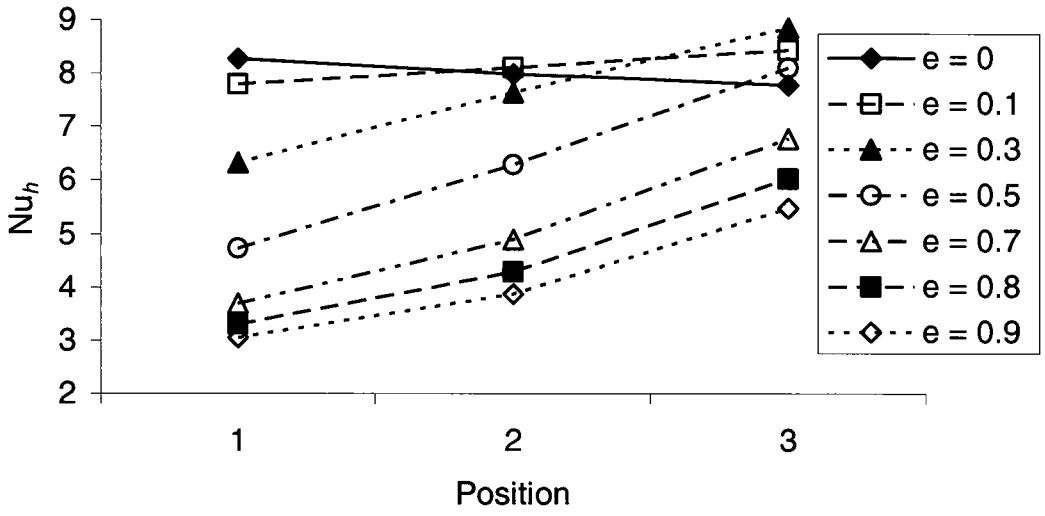

Figure 103 – Azimuthal variation of the Nusselt number for $q'' = 30$ W/m^2

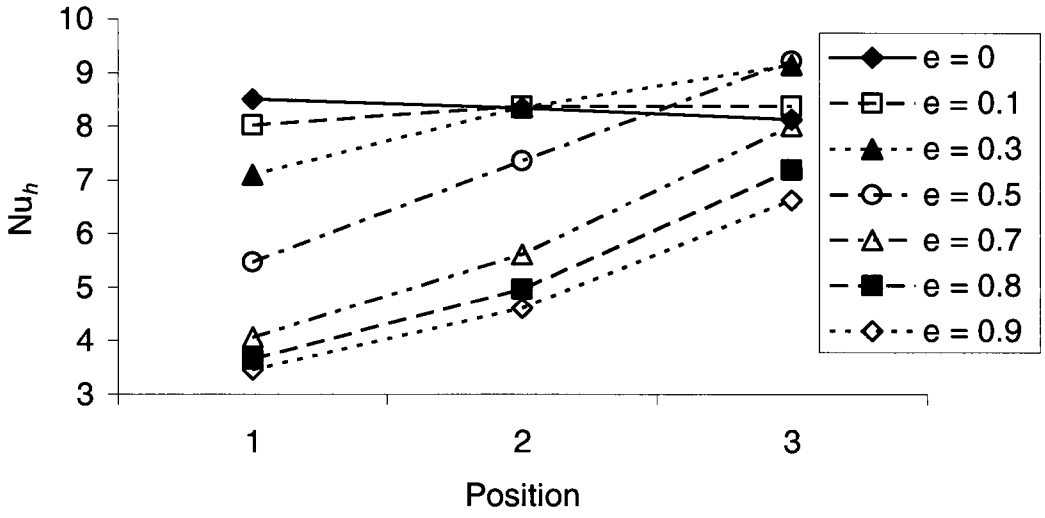

Figure 104 – Azimuthal variation of the Nusselt number for $q'' = 80$ W/m^2

In the previous plots for the local Nusselt number, the hydraulic diameter was used as the scale for all three azimuthal positions. A more appropriate definition of the local Nusselt number can be based on the local distance between the two cylinders, as

$$\mathrm{Nu}_d = \frac{hd}{k} \tag{73}$$

for which d is the local distance between the two cylinders at each of the three azimuthal positions as seen in Figure 105. The variation of d for different azimuthal positions and eccentricities is presented in Table 15.

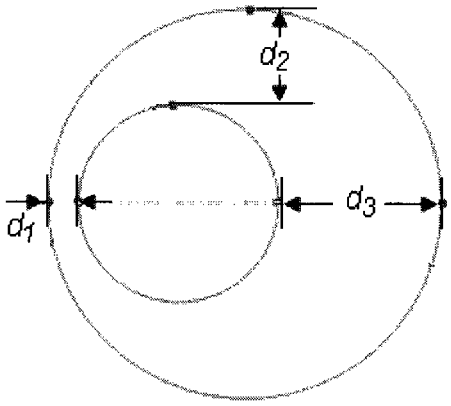

Figure 105 – Distance d used in the calculation of local dimensionless groups

Table 15 – Variation of d with eccentricity for different azimuthal positions

	d [m]		
	Position		
e	**1**	**2**	**3**
0	0.0160	0.0160	0.0160
0.1	0.0144	0.0160	0.0176
0.3	0.0112	0.0160	0.0208
0.5	0.0080	0.0160	0.0240
0.7	0.0048	0.0160	0.0272
0.8	0.0032	0.0160	0.0288
0.9	0.0016	0.0160	0.0304

Using this new scaling, the azimuthal variation of the Nusselt number for different eccentricities at a height of $z^* = 0.5$ is presented in Figure 106 and 107. These figures show that using the local length amplifies the effect of eccentricity on the Nusselt number. While at position 1 increasing eccentricity consistently weakens the local Nusselt number, at position 3 it consistently strengthens the Nusselt number. At high eccentricity, conduction plays a more significant role in the narrow gap and convection plays a more significant role in the wide gap.

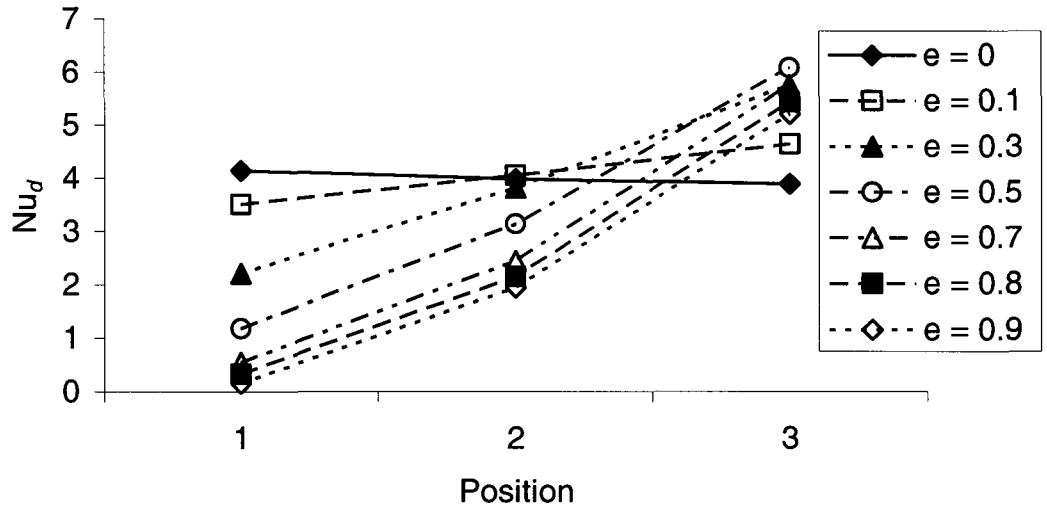

Figure 106 – Azimuthal variation of Nu_d for $q'' = 30$ W/m^2

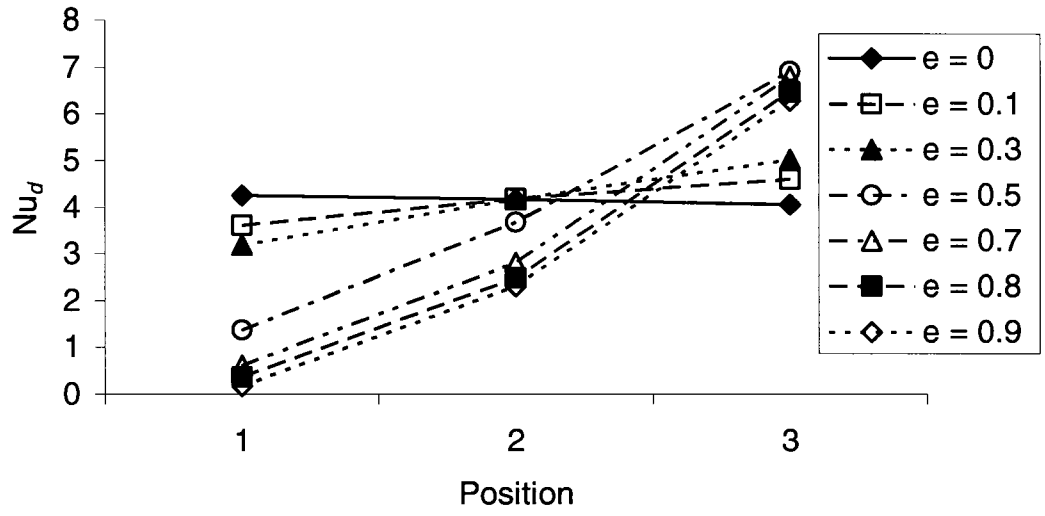

Figure 107 – Azimuthal variation of Nu_d for $q'' = 80$ W/m^2

Figure 108 and 109 present the axial variations of the Nusselt number for different eccentricities and wall heat fluxes of 30 W/m^2 and 80 W/m^2, respectively. In these figures we see that, like the convection heat transfer coefficient, the Nusselt number decreases downstream until it reaches a location where the flow becomes thermally fully developed, beyond which the Nusselt number stays constant. The Nusselt number is seen to remain roughly constant at low eccentricities and to decrease as eccentricity is further increased. As well, we notice that at the entrance of the annulus, for eccentricities less than 0.5, the Nusselt number is roughly the same; however, at higher eccentricities this is no longer the case.

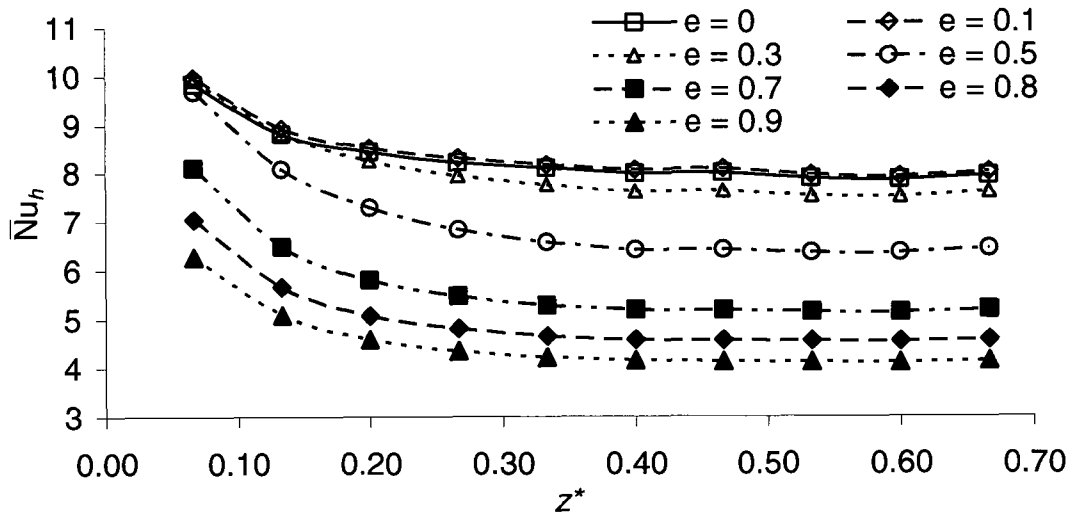

Figure 108 – Axial variation of Nu_h for $q'' = 30$ W/m^2

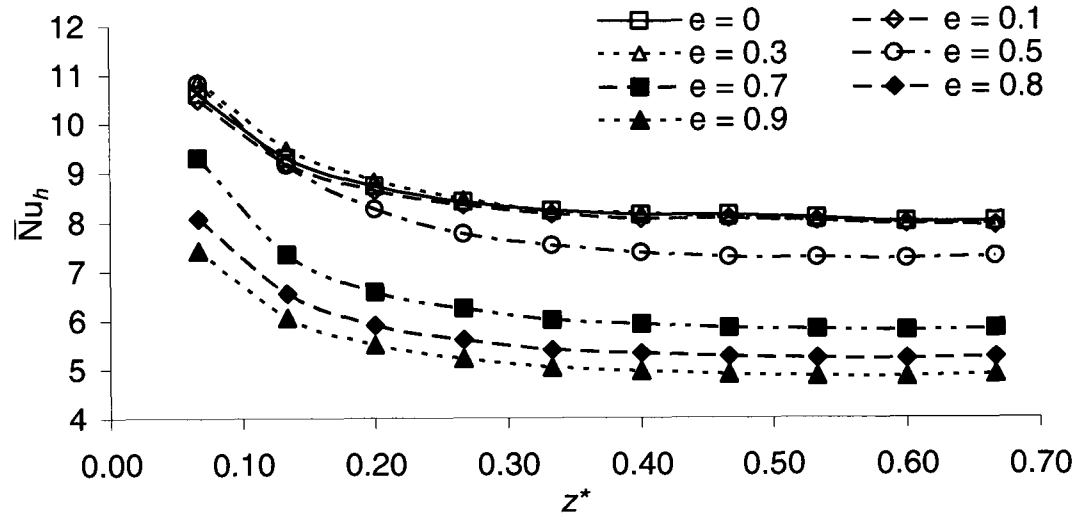

Figure 109 – Axial variation of Nu_h for $q'' = 80$ W/m^2

Figure 110 and 111 show, respectively, the variations of the Grashof and modified Grashof numbers with eccentricity. The Grashof number, which is a measure of the ratio of

buoyancy forces to viscous forces, increases with eccentricity. In contrast, the modified Grashof number, which is the product of the Grashof number and the Nusselt number, appears to be relatively insensitive to eccentricity, in fact showing a weak tendency to decrease as eccentricity increases. Both the Grashof and modified Grashof numbers for the higher heat flux are substantially higher than the corresponding numbers for the lower heat flux.

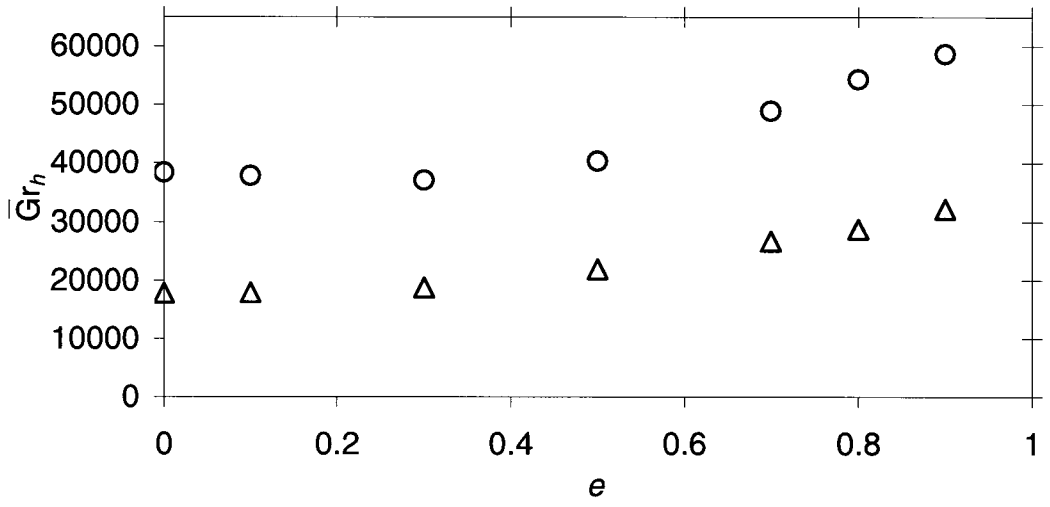

Figure 110 – Dependence of the Gr_h on eccentricity for $q'' = 30$ W/m^2 (△) $q'' = 80$ W/m^2 (○)

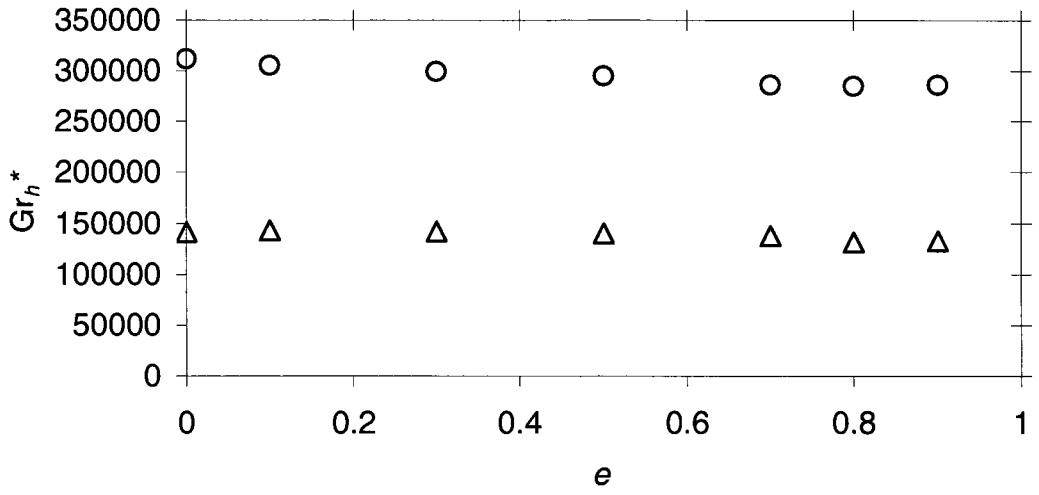

Figure 111 – Dependence of Gr_h^* on eccentricity for $q'' = 30$ W/m^2 (△) $q'' = 80$ W/m^2 (○)

Figure 112 and 113 present the azimuthal variations of the local Grashof number for $q'' = 30$ W/m^2 and $q'' = 80$ W/m^2, respectively. Overall we see an increase in the Grashof number with eccentricity, however, the increase is more pronounced at position 1. At low eccentricities, similar to the heat transfer coefficient and the Nusselt number, we see that an increase in the Grashof number at position 1 is initially balanced by a decrease at position 2.

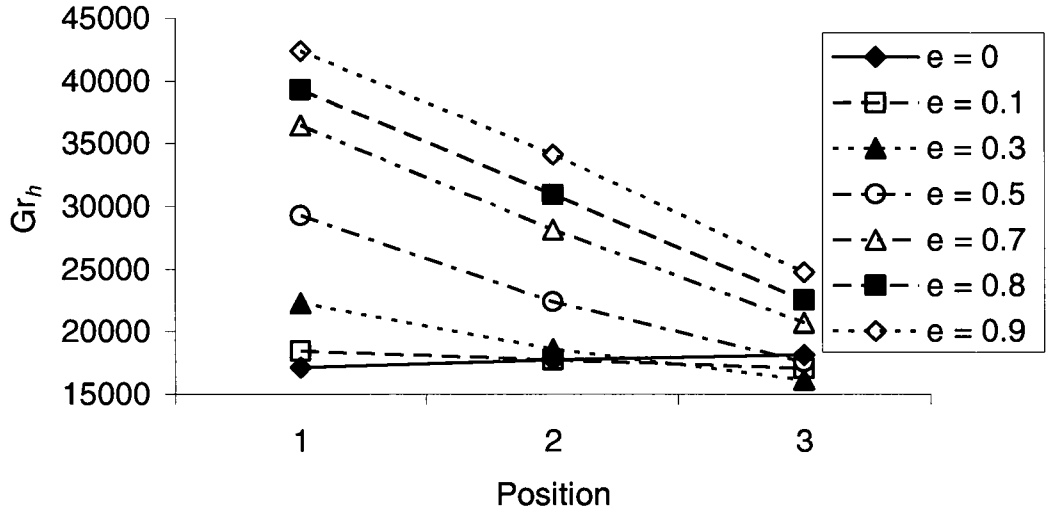

Figure 112 – Azimuthal variation of Gr_h for $q'' = 30$ W/m^2

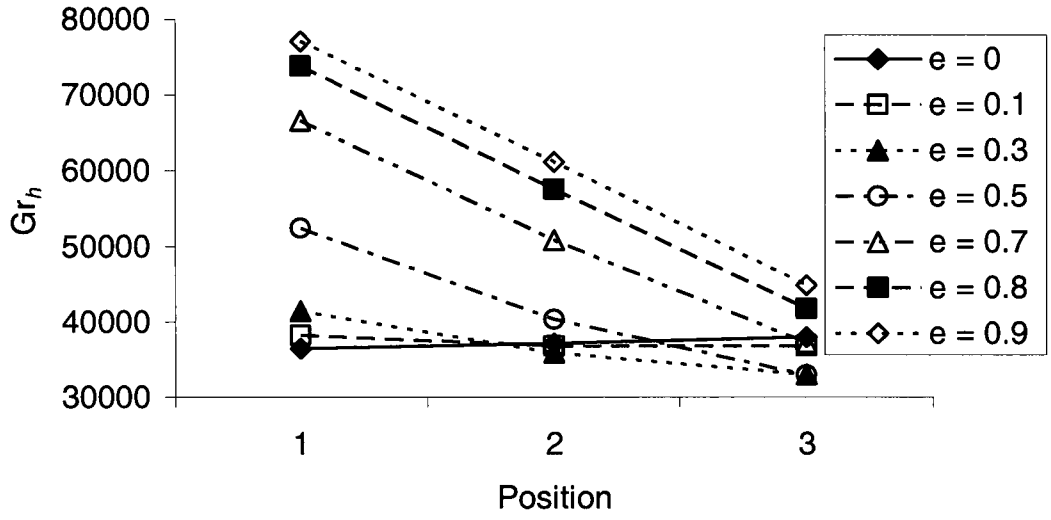

Figure 113 – Azimuthal variation of Gr_h for $q'' = 80$ W/m^2

In Figure 114 and 115 we have plotted the variation of the local Grashof number taking into account the local spacing as we had done previously for the Nusselt number. In these figures, we can see that at position 1 the Grashof number decreases with eccentricity as

the spacing between the two cylinders decreases. In contrast, at position 3 the Grashof number increases dramatically with eccentricity. The Grashof number is highly dependent on wall spacing and this is evident in these figures.

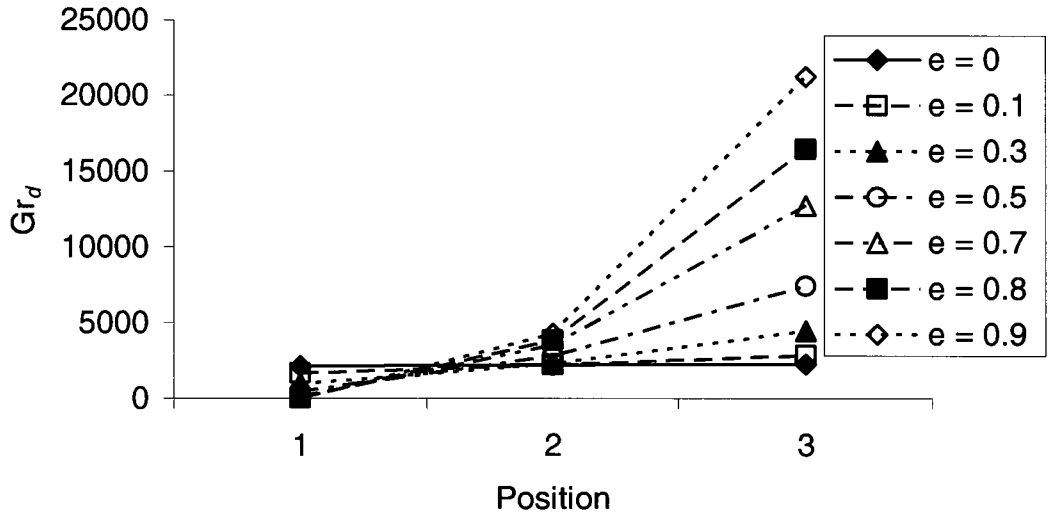

Figure 114 – Azimuthal variation of Gr_d for $q'' = 30$ W/m^2

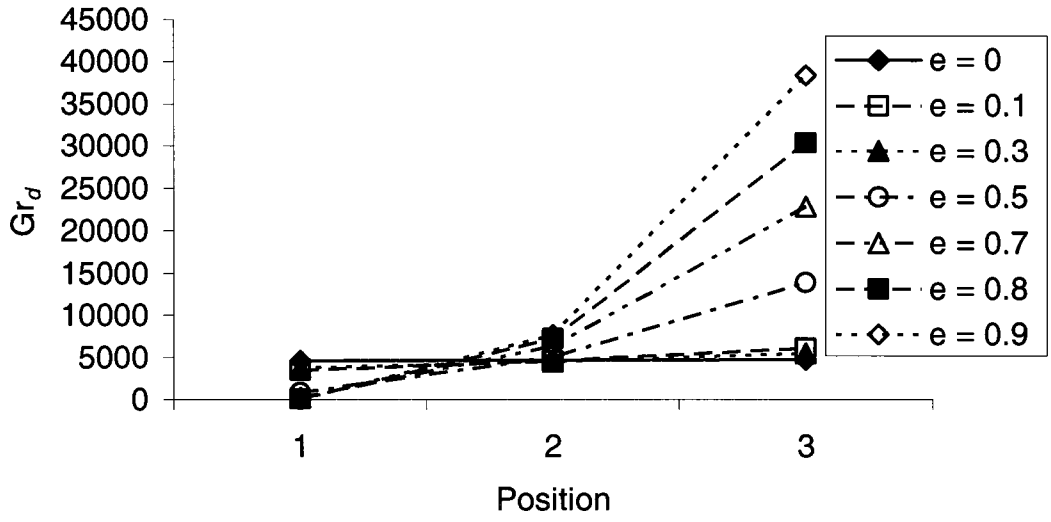

Figure 115 – Azimuthal variation of Gr_d for $q'' = 80$ W/m^2

The axial variation of the Grashof number is seen in Figure 116 and 117. We can observe that near the inlet the Grashof number increases and reaches a maximum which varies in axial location between $z^* = 0.27$ and $z^* = 0.40$ depending on eccentricity and wall heat flux. Following this, the Grashof number begins to decrease at a constant rate. The reason for this is that initially the increase in the difference between the mean fluid temperature and the wall temperature leads to an increase in the buoyancy forces, which in turn increases the Grashof number. However, as the fluid temperature increases and the fluid moves faster, the viscous forces also increase. Eventually, when the difference between the wall and mean fluid temperature becomes constant, we start seeing the effects of increased viscous forces. The decrease in the volumetric thermal expansion coefficient with temperature also plays a minor role in decreasing the Grashof number as the fluid temperature increases, however the dominating factor in the decrease remains the kinematic viscosity.

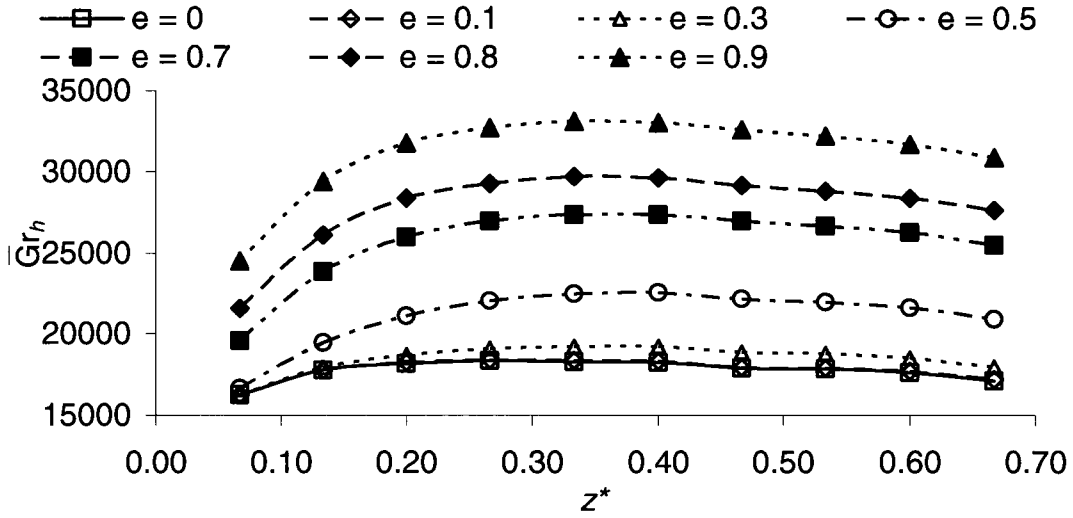

Figure 116 – Axial variation of $\overline{Gr}_h$ for $q'' = 30$ W/m^2

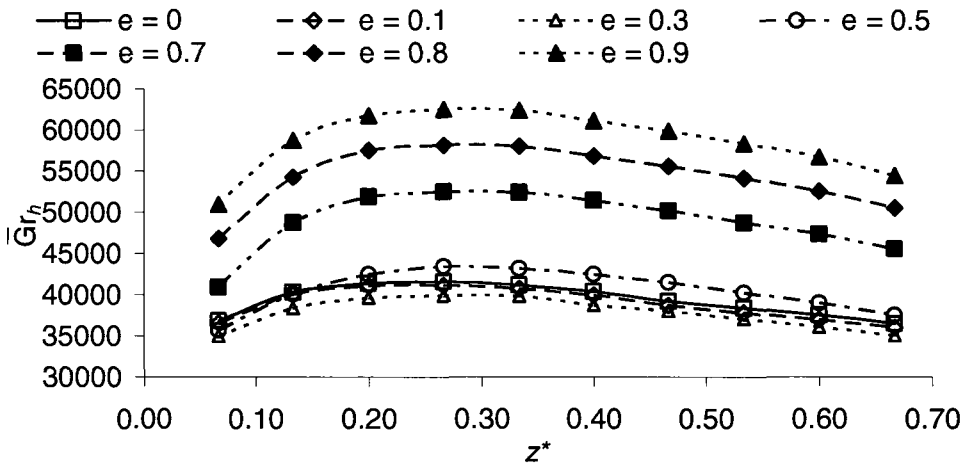

Figure 117 – Axial variation of $\overline{Gr}_h$ for $q'' = 80$ W/m^2

Figure 118 and 119 show, respectively, the variations of the Rayleigh and modified Rayleigh numbers with eccentricity. The trends are correspondingly the same as those observed for the Grashof and modified Grashof numbers, respectively. This was expected, because the Rayleigh number is the product of the Grashof number and the Prandtl number, which had very small variation in the present experiments.

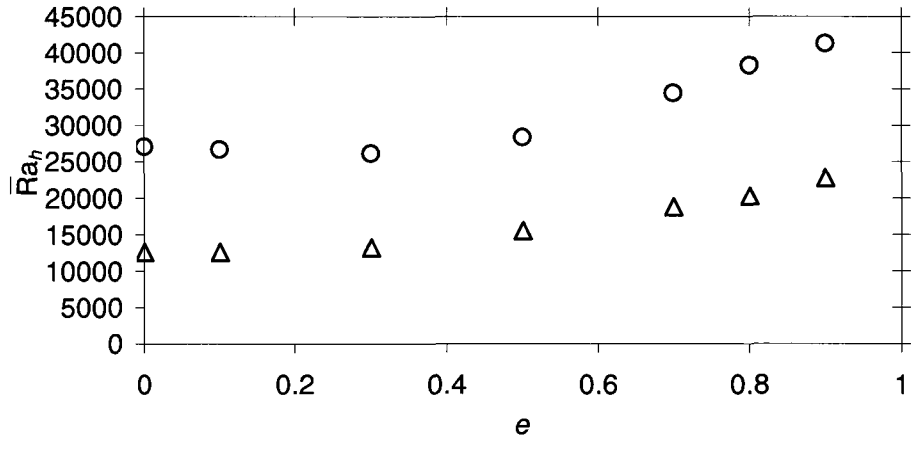

Figure 118 – Dependence of $\overline{Ra}_h$ on eccentricity for $q'' = 30$ W/m^2 (△) $q'' = 80$ W/m^2 (○)

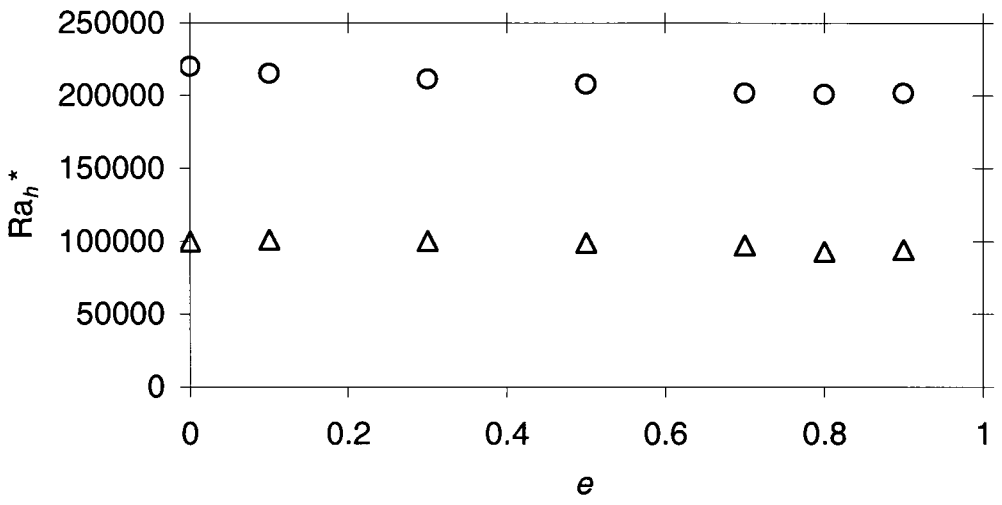

Figure 119 – Dependence Ra_h^* on eccentricity for $q'' = 30$ W/m^2 (△) $q'' = 80$ W/m^2 (○)

Looking at Figure 111 and 119 we realize that the modified dimensionless groups represented in these graphs appear to be following a general trend with their magnitude depending on wall heat flux. Dividing the values of the modified Rayleigh and Grashof numbers for a wall heat flux of 80 W/m^2 by that for their respective values for a wall heat flux of 30 W/m^2 we get Gr** and Ra**. After plotting versus eccentricity, Gr** and Ra** are found to have an approximately linear relationship over the range of eccentricities as seen in Figure 120. Gr** and Ra** are both approximately equal to 2.15, while the heat flux ratio is equal to 2.67. This means that the plots for the modified Rayleigh and Grashof numbers versus eccentricity for different wall heat fluxes, if scaled by the proper non-dimensional variant of the heat flux could potentially collapse onto a single curve; further investigation of this is recommended for future studies.

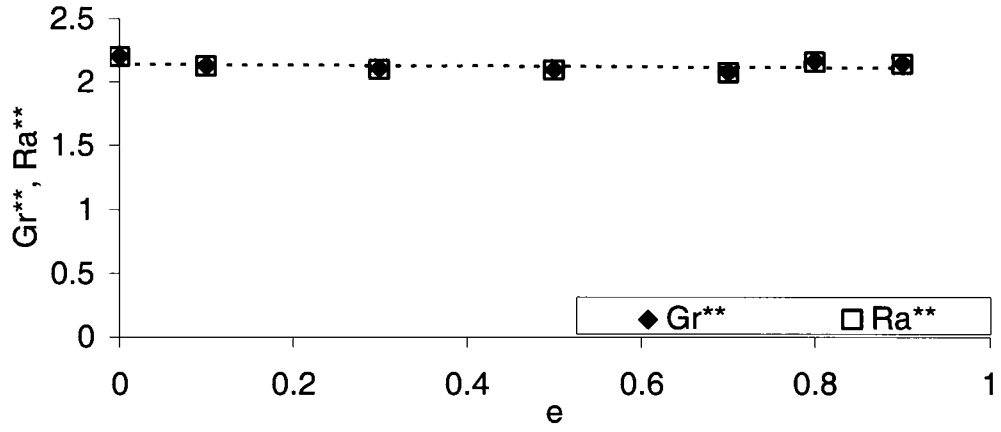

Figure 120 – Ratio of modified Grashof number and Rayleigh number for wall heat fluxes of 30 W/m^2 (△) and 80 W/m^2 (○)

Because the Prandtl number in our experiments did not vary significantly one would expect that the observations made for the local variation of the Grashof number would also apply to the local variation of the Rayleigh number. For completeness, we presented the azimuthal variation of the Rayleigh number in Figure 121, 122, 123 and 124 as well as the axial variation of the Rayleigh number in Figure 125 and 126 for the different wall heat fluxes. Apart from the difference in magnitudes, no additional observations can be made for these figures which have not already been done for the Grashof number.

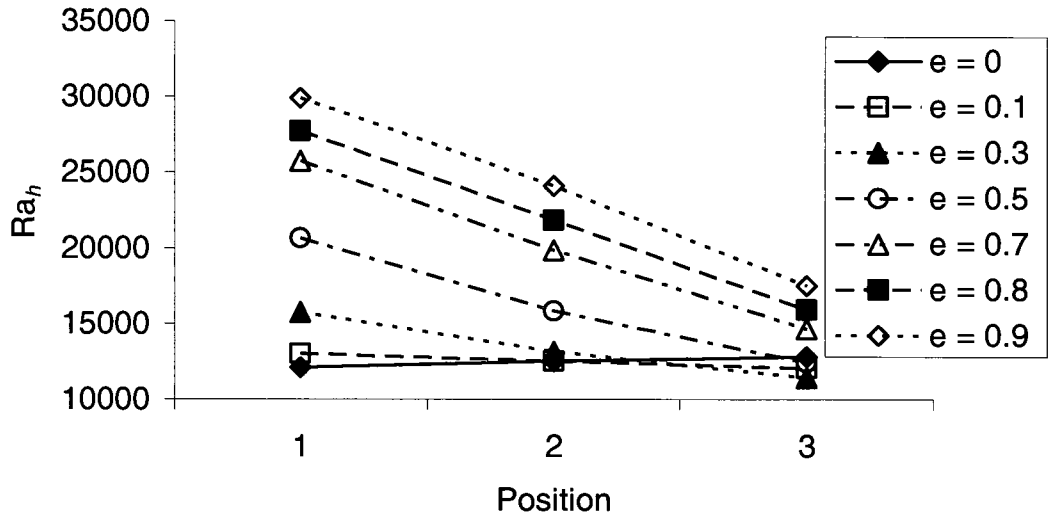

Figure 121 – Azimuthal variation of Ra_h for $q'' = 30$ W/m^2

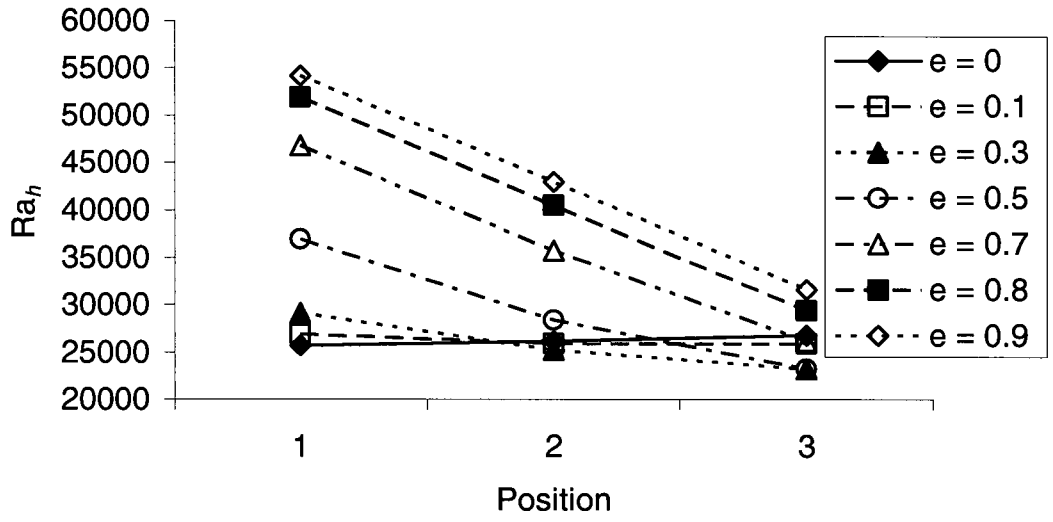

Figure 122 – Azimuthal variation of Ra_h for $q'' = 80$ W/m^2

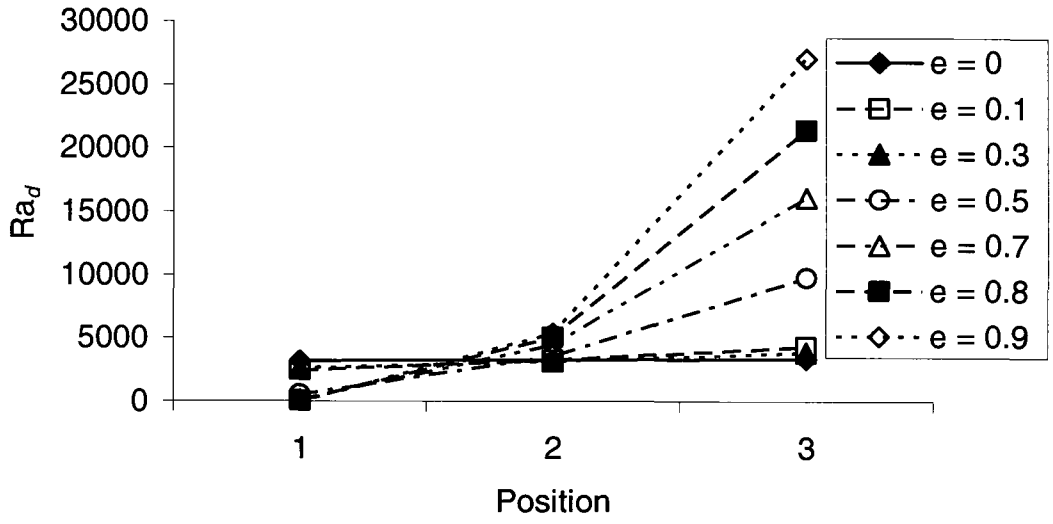

Figure 123 – Azimuthal variation of Ra_d for $q'' = 30$ W/m^2

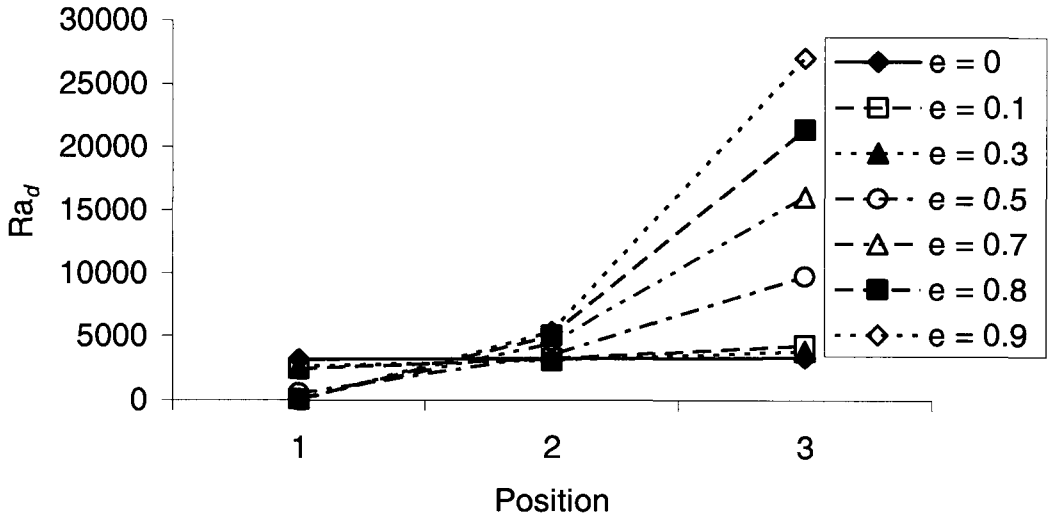

Figure 124 – Azimuthal variation of Ra_d for $q'' = 80$ W/m^2

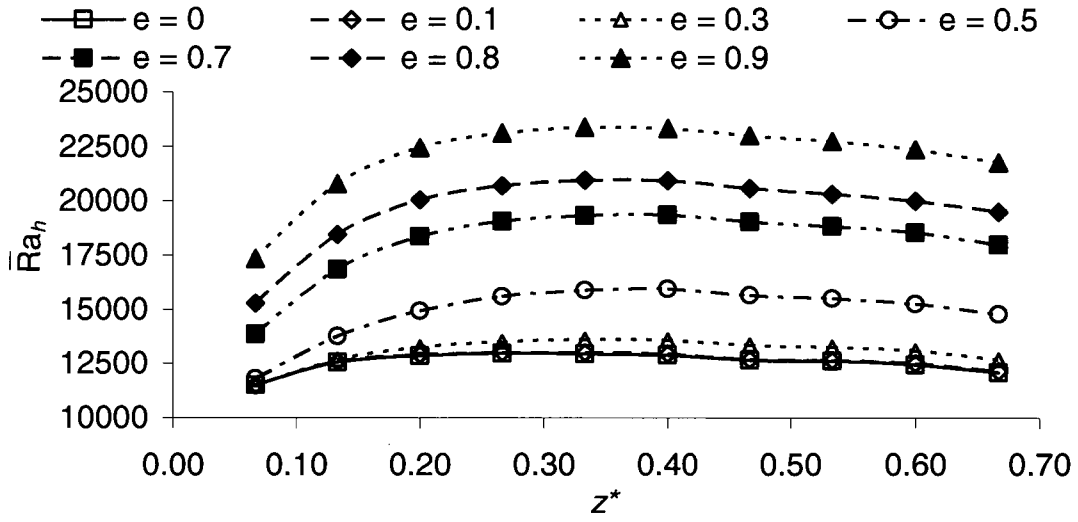

Figure 125 – Axial variation of $\overline{Ra}_h$ for $q'' = 30$ W/m^2

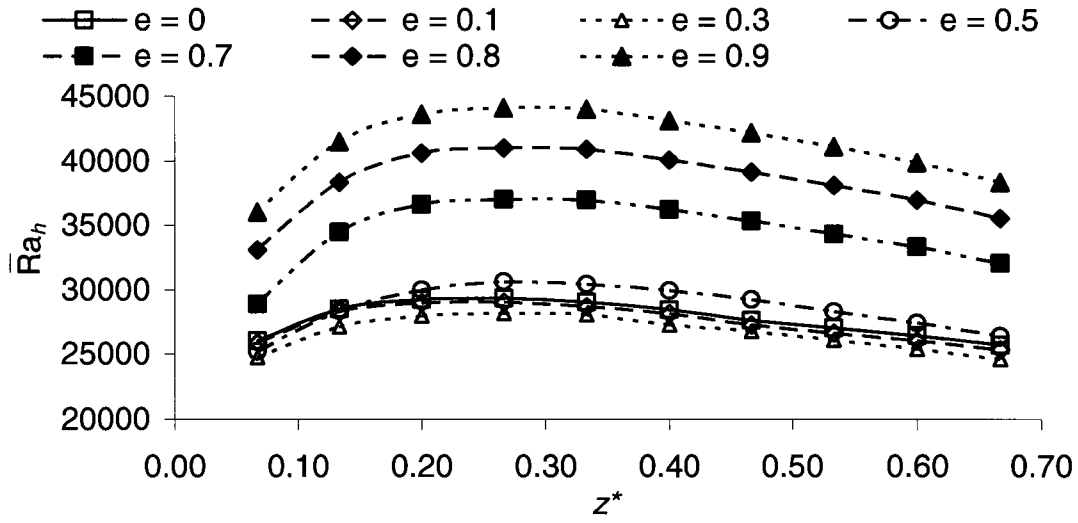

Figure 126 – Axial variation of $\overline{Ra}_h$ for $q'' = 80$ W/m^2

In Figure 127 we have plotted the Grashof number versus the Nusselt number for different eccentricities and wall heat fluxes. For each eccentricity, the higher values of the

Grashof number are for q'' = 80 W/m^2, while the lower values are for q'' = 30 W/m^2. Although additional experiments at higher heat fluxes would allow us to form a more concrete understanding of the relationship between the Nusselt and Grashof number, we can still make some general observations. In general, increasing the heat flux increases both the Grashof number and the Nusselt number. However, at very low eccentricities, the increase in the Nusselt number is very small, if any at all, whereas the Grashof number increases measurably.

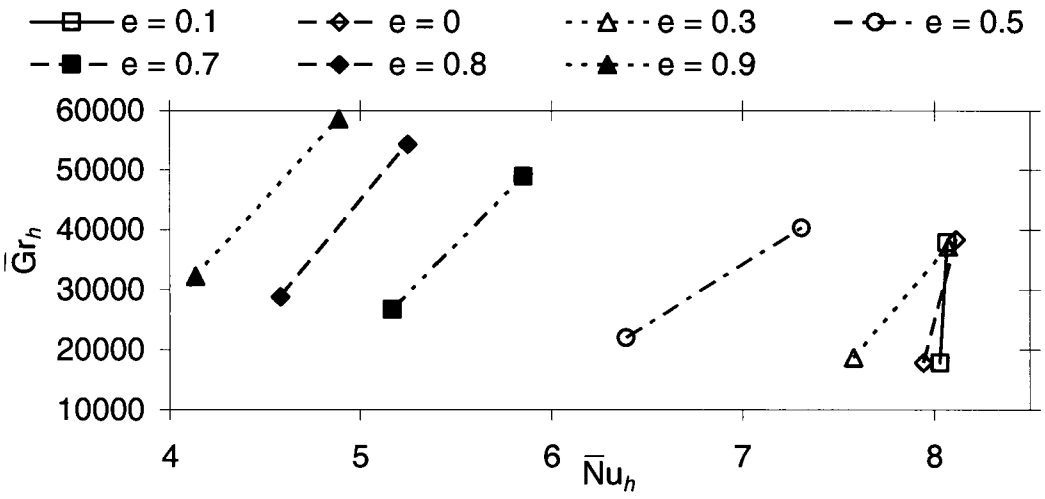

Figure 127 – The Grashof number versus the Nusselt number for different eccentricities and wall heat fluxes; higher values are for q'' = 80 W/m^2 and lower values are for q'' = 30 W/m^2

Figure 128 shows the Rayleigh number versus the Nusselt number. Once more, to avoid repetition, the observations in this figure are the same as was done for the Grashof number versus the Nusselt number.

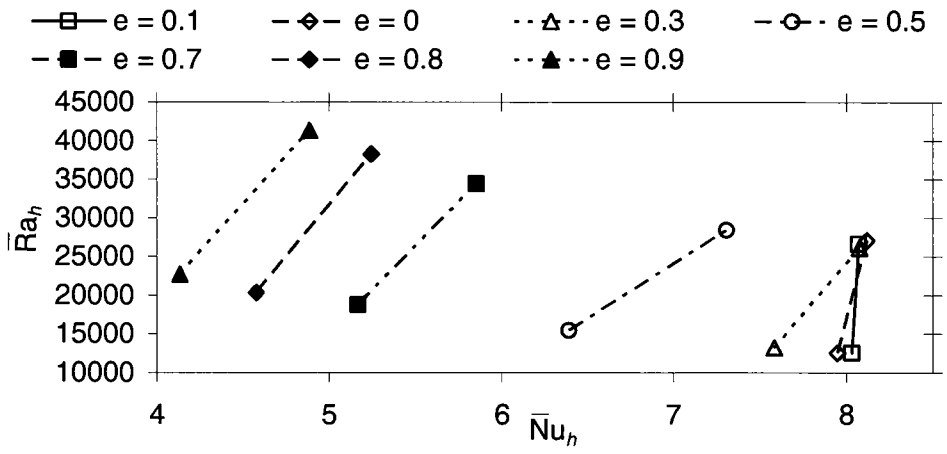

Figure 128 – The Rayleigh number versus the Nusselt number for different eccentricities and wall heat fluxes

The axial variation of the bulk Reynolds number for $q'' = 30$ W/m^2 and $q'' = 30$ W/m^2 can be seen in Figure 129 and 130, respectively. With the exception of the outlet region, the Reynolds number generally decreases slowly with height along the annulus, due to the increase in the viscosity with temperature.

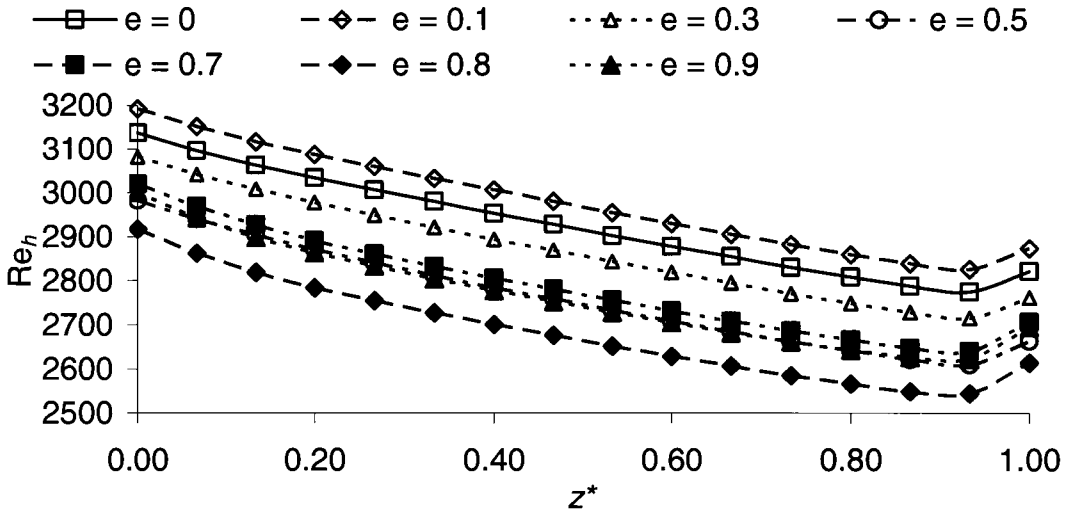

Figure 129 – Axial variation of the Reynolds number for $q'' = 30$ W/m^2

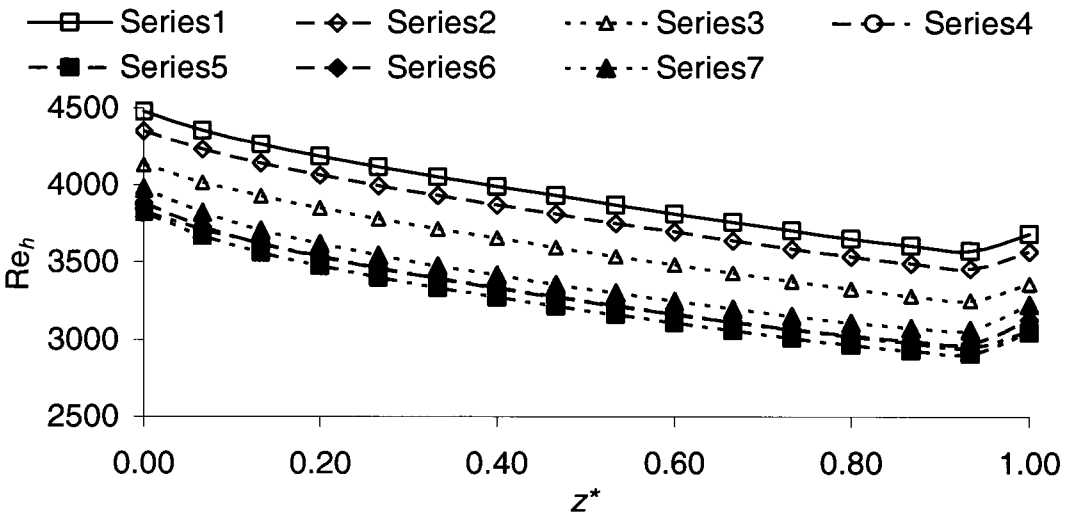

Figure 130 – Axial variation of the Reynolds number for $q'' = 80$ W/m^2

Chapter 9 Conclusions and Recommendations

9.1 Conclusions

The main objective of this study was to find the effect of eccentricity e on the natural convection heat transfer in an open-ended vertical cylindrical annulus. It was assessed that the flow became thermally fully developed at a distance from the entrance that was about 40% of the channel height, as, beyond this point, the azimuthally averaged heat transfer coefficient $\overline{h}$ was essentially independent of axial position. To avoid entrance effects at the inlet and radiation effects at the outlet, the study was focused on the central region of the annulus.

It was found that, at low eccentricities, there was very little effect of eccentricity on the average convection heat transfer from the annulus. The reason for this was made clear after examining the local azimuthal variation of the convection heat transfer coefficient and Nusselt number Nu. It was observed that at low eccentricities a decrease in the heat transfer experienced in the region where the two cylindrical surfaces of the annulus were closer together was compensated for by an enhancement of heat transfer on the opposing side of the cylinders. For the higher of the two wall heat fluxes considered, the insensitivity of $\overline{h}$ and Nu to eccentricity was extended to a higher range of e. Beyond this initial insensitive region,

as e was increased, the heat transfer diminished monotonically for both wall heat fluxes examined.

The Grashof and Rayleigh numbers showed an increasing trend with increasing eccentricity, which implies that the buoyancy force becomes more significant with respect to the viscous force. The mass flow rate through the annulus increased with increasing wall heat flux and generally decreased somewhat with increasing eccentricity. The Reynolds number exhibited the same trends.

The axial variations of the Grashof and Rayleigh numbers showed initial increases followed by steady decreases, indicating that viscous forces overcame the buoyancy forces at some location in the upstream half of the apparatus. The Reynolds number steadily decreased for the entire length of the annulus except near the outlet, where end effects were present.

9.2 Recommendations for future work

For future work, using the same apparatus, it would be recommended to use a hot-wire anemometer or other fast-response velocity or temperature sensor to detect the presence of possible flow pulsations near the narrow gap at high eccentricities. A wider range of wall heat fluxes would be desirable as it would provide more insight on how eccentricity effects vary for different Rayleigh and Grashof numbers. We had noticed that at higher heat fluxes, the effect of eccentricity on the overall heat transfer was delayed, so perhaps this might be an area of focus for future work.

Similar experiments could also be done for both forced and mixed convection. Such experiments can be easily made by connecting the outlet of the annulus to the suction side of a blower. Additional experiments for natural, mixed and forced convection would be useful by replacing the current core by similar ones with different diameters, so that the effect of diameter ratio of the annulus can be examined. The construction of the present apparatus required a lot of time and skill, because of the large number of thermocouples embedded into the test section and other challenges in fabricating the various components. Nevertheless, we found while measuring the dependence of wall resistance on temperature that one could estimate the average wall temperature in the annulus by monitoring the voltage variation if current is held constant or vice versa. Therefore, if one is to perform similar experiments with different diameter ratios, a much simpler test section could be constructed, using much fewer thermocouples.

One of the limiting factors of our setup was the maximum temperature it could handle. Many of the construction materials, for example, the adhesive film of the stainless steel foil, had a maximum recommended temperature that was lower than 100 °C. We expect that different phenomena would occur at higher temperatures. Therefore, it is recommended, if one wishes to build a similar apparatus or test section, that materials with higher tolerances to temperature be used.

The aspect ratio we had used was limited by the material used for the core section of the annulus. For the diameter ratio we had chosen, the aspect ratio was barely sufficient to give us a region far away from the ends that it would not be affected by radiation losses. If one wishes to avoid radiation effects, it is recommended that an annulus with a higher aspect ratio be used, especially if it has a large diameter ratio.

References

Al-Arabi, M., El-Shaarawi, M. A. I., and Khamis, M. (1987). "Natural convection in uniformly heated vertical annuli." *International Journal of Heat and Mass Transfer*, 30(7), 1381-1389.

Bar-Cohen, A., and Rohsenow, W. M. (1984). "Thermally optimum spacing of Vertical Natural Convection Cooled parallel plates." *ASME Journal of Heat Transfer*, 106, 116-123.

Bejan, A. (2004). "Convection Heat Transfer." John Wiley & Sons Inc., Hoboken, New Jersey, USA.

Bhandari, B. (2003). "Experimental Study of Natural Convection Heat Transfer in Vertical Concentric and Eccentric Annuli." M.Eng Report, Department of Mechanical Engineering, University of Ottawa, Ottawa, Canada.

Brodkey, R. S., and Hershey, H. C. (2003). "Transport Phenomena: A Unified Approach." Brodkey Publishing, Columbus, Ohio, USA.

Brush, S. G. (1973). "The development of the kinetic theory of gases." *Archive for History of Exact Sciences*, 11(1), 38-96.

Carleton, F. J., and Agalloco, J. P. (1998). "Validation of pharmaceutical processes: sterile products." 2nd Edition, Informa Healthcare, New York, USA.

Chang, D., and Tavoularis, S. (2006). "Convective Heat Transfer in Turbulent Flow Near a Gap." *Journal of Heat Transfer*, 128, 701-708.

Chen, K. C., and Hwang, G.-J. (1968). "Laminar forced convection in eccentric annuli." *AlChE Journal*, 14(3), 510-512.

Churchill, S. W., and Chu, H. S. (1975). "Correlation equations for laminar and turbulent free convection from a vertical plate." *International Journal of Heat and Mass Transfer*, 18(11), 1323-1329.

Cussler, E. L. (1997). "Diffusion: Mass Transfer in Fluid Systems." Cambridge University Press, Cambridge, UK.

Das, S. K. (2005). "Process Heat Transfer." Alpha Science International.

Davidson, J., and Liu, W. (1999). "Comparison of Natural convection heat exchangers for solar water heating systems." Portland, Maine, USA.

Dimmick, G. R., Chatoorgoon, V., Khartabil, H. F., and Duffey, R. B. (2002). "Natural-convection studies for advanced CANDU reactor concepts." *Nuclear Engineering and Design*, 215(1-2), 27-38.

Dotson, J. P. (1954). "Heat Transfer From a Vertical Plate by Free Convection." Masters Thesis, Purdue University, West Lafayette, Indiana, USA.

Dyer, J. R. (1975). "The development of laminar natural-convective flow in a vertical uniform heat flux duct." *International Journal of Heat and Mass Transfer*, 18, 1455-1465.

Elenbaas, W. (1942a). "Heat Dissipation of Parallel Plates by Free Convection." *Physica*, 9(1), 1-28.

Elenbaas, W. (1942b). "The dissipation of heat by free convection: The inner surface of vertical tubes of different shapes of cross-section." *Physica*, 9(8), 865-874.

Feingold, A., and Gupta, K. G. (1970). "New analytical approach to the evaluation of configuration factors in radiation from spheres and infinitely long cylinders." *Journal of Heat Transfer*, 92(1), 69-76.

Fox, R. W., McDonal, d. A. T., and Pritchard, P. J. (2003). "Introduction to Fluid Mechanics." John Wiley & Sons, Inc., Hoboken, New Jersey, USA.

Gosset, A., and Tavoularis, S. (2006). "Laminar Flow Instability in a Rectangular Channel with a Cylindrical Core." *Physics of Fluids*, 18(4), 044108.1-044108.8.

Guellouz, M. S., and Tavoularis, S. (2000a). "The Structure of Turbulent Flow in a Rectangular Channel Containing a Cylindrical Rod - Part 1: Reynolds-Averaged Measurements." *Experimental Thermal and Fluid Science*, 23, 59-73.

Guellouz, M. S., and Tavoularis, S. (2000b). "The Structure of Turbulent Flow in a Rectangular Channel Containing a Cylindrical Rod - Part 2: Phase-Averaged Measurements." *Experimental Thermal and Fluid Science*, 23, 75-91.

Heldman, D. R. (2003). "Encyclopedia of Agricultural, Food, and Biological Engineering." CRC Press, Baton Rouge, USA.

Hosseini, R., Heyrani-Nobari, M. R., and Hatam, M. (2005). "An experimental study of heat transfer in an open-ended vertical eccentric annulus with insulated and constant heat flux boundaries." *Applied Thermal Engineering*, 25(8-9), 1247-1257.

Incropera, F. P., and DeWitt, D. P. (2002). "Fundamentals of Heat and Mass Transfer." John Wiley & Sons Inc., Hoboken, New Jersey, USA.

Jarall, S., and Campo, A. (2005). "Experimental study of natural convection from electrically heated vertical cylinders immersed in air." *Experimental Heat Transfer*, 18(3), 127-134.

Khatak, H. S., and Raj, B. (2002). "Corrosion of Austenitic Stainless Steel." Woodhead Publishing, Abington, Cambridge, UK.

Kuehn, T. H., and Goldstein, R. J. (1978). "An experimental study of natural convection heat transfer in concentric and eccentric horizontal cylindrical annuli." *ASME Journal of Heat Transfer*, 100, 635-640.

Martynenko, O. G., and Khramtsov, P. P. (2005) "Free-Convective Heat Transfer: With Many Photographs of Flows and Heat Exchange." Springer, Berlin, Germany.

Modest, M. F. (2003). "Radiative Heat Transfer." 2nd edition, Academic Press, Boston, Massachusetts, USA.

Narasimhan, A. (1999). "Rayleigh-Benard Convection: Physics of a Widespread Phenomenon." Resonance: Journal of Science Education, 4(6), 82-90.

Ninokata, H., Merzari, E. and Khakim, A. (2009) "Analysis of Low Reynolds Number Turbulent Flow Phenomena in Nuclear Fuel Pin Subassemblies of Tight Lattice Configuration," *Nuclear Engineering and Design*, 239, 855-866.

Prout, W. (1835). "Chemistry, Meteorology, and the Function of Digestion: Considered with Reference to Natural Theology." William Pickering, London, UK.

Sonntag, R. E., Borgnakke, C., and Van Wylen, G. J. (1998). "Fundamentals of Thermodynamics." John Wiley & Sons Inc., New York, USA.

Sparrow, E. M., and Charmchi, M. (1983). "Natural convection experiments in an enclosure between eccentric or concentric vertical cylinders of different height and diameter." International Journal of Heat and Mass Transfer, 26, 133-143.

Sparrow, E. M., Chrysler, G. M., and Azevedo, L. F. (1984). "Observed Flow Reversals and Measured-Predicted Nusselt Numbers for Natural Convection in a One-Sided Heated Vertical Chanel." Journal of Heat Transfer, 106, 325-332.

Sparrow, E. M., and Gregg, J. L. (1956a). "Laminar free convection from a vertical plate with uniform surface heat flux." Transactions of the ASME, 78, 435-440.

Sparrow, E. M., and Gregg, J. L. (1956b). "Laminar Free Convection Heat Transfer From the Outer Surface of a Vertical Circular Cylinder." Transactions of the ASME, 78, 1823-1829.

Tavoularis, S. (2005). "Measurement in Fluid Mechanics." Cambridge University Press, Cambridge, UK.

Wilson, J. S., Kester, W., Ball, S., Huddleston, C., Ibrahim, D., De Silva, G. M. S., Ramsden, E., and James, K. (2008). "Test and Measurement: Know It All." Newnes, Burlington, Massachusetts, USA.

Wirtz, R. A., and Stutzman, R. J. (1982). "Experiments of free convection between vertical plates with symmetric heating." *Journal of Heat Transfer*, 104, 501-507.

Appendix A Power supply monitoring and control LabVIEW block diagram

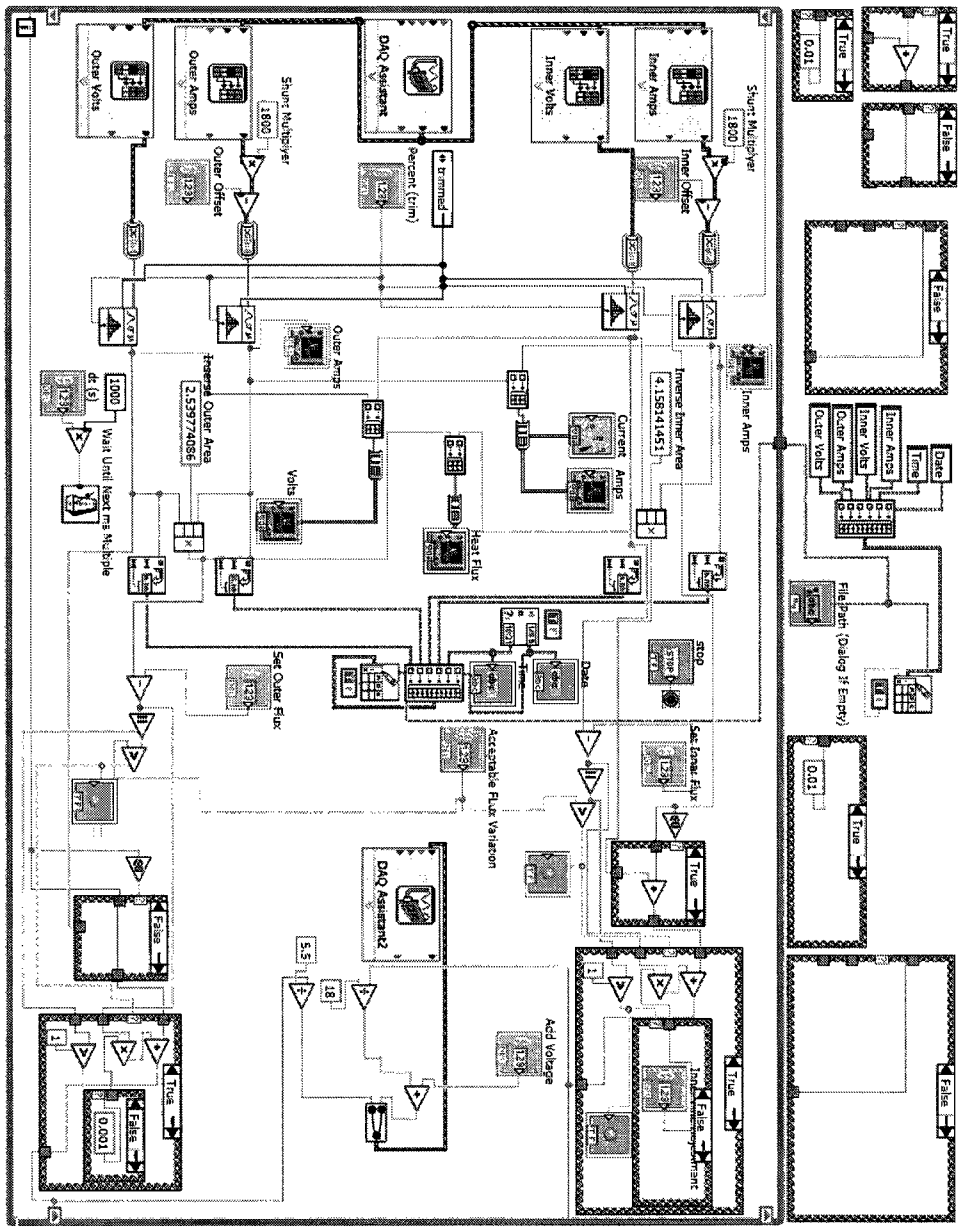

Figure 1 – LabVIEW block diagram

Appendix B Temperature data acquisition software additional description

The temperature data acquisition software was written not only as a temperature monitoring tool but also as an analysis tool. This appendix will go through some of the program features which were not covered in the body of the thesis.

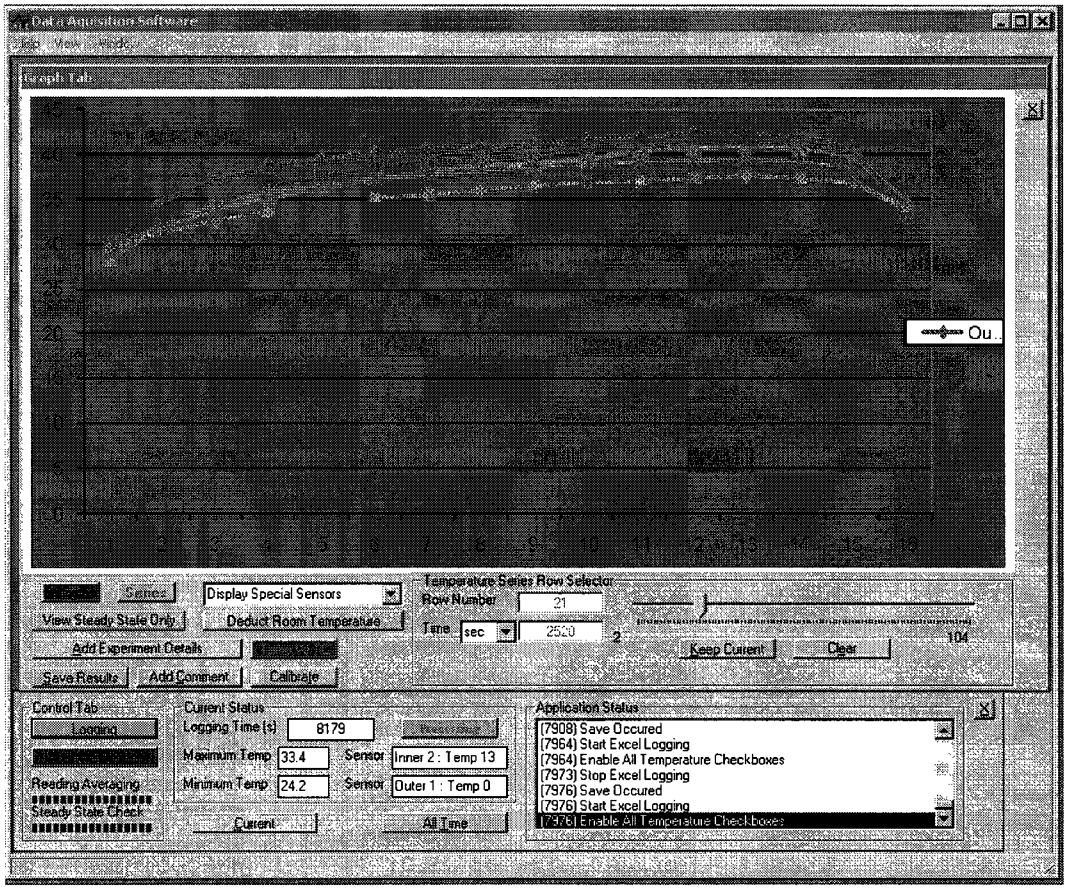

Figure 1 – Overall program view

The figure above shows what the overall running program would look like. In this case, the graph tab is showing, and the control tab at the bottom is usually always present. The control tab seen in the figure below has two main buttons, which are the *Logging* button and the *Acquisition* button. The *Acquisition* button tells the program to accept additional readings from the thermocouples, while the *Logging* button tells the program to log the results to an excel file after a certain number of acquisitions and data averaging.

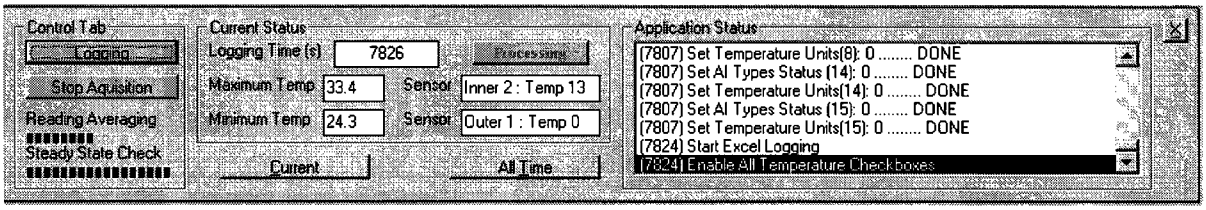

Figure 2 – Control Tab

The control tab also allows us to view the current and the all time maximum and minimum temperatures, as well as the overall time that the program has been running for. A status box on the right also displays events which might be important for the user.

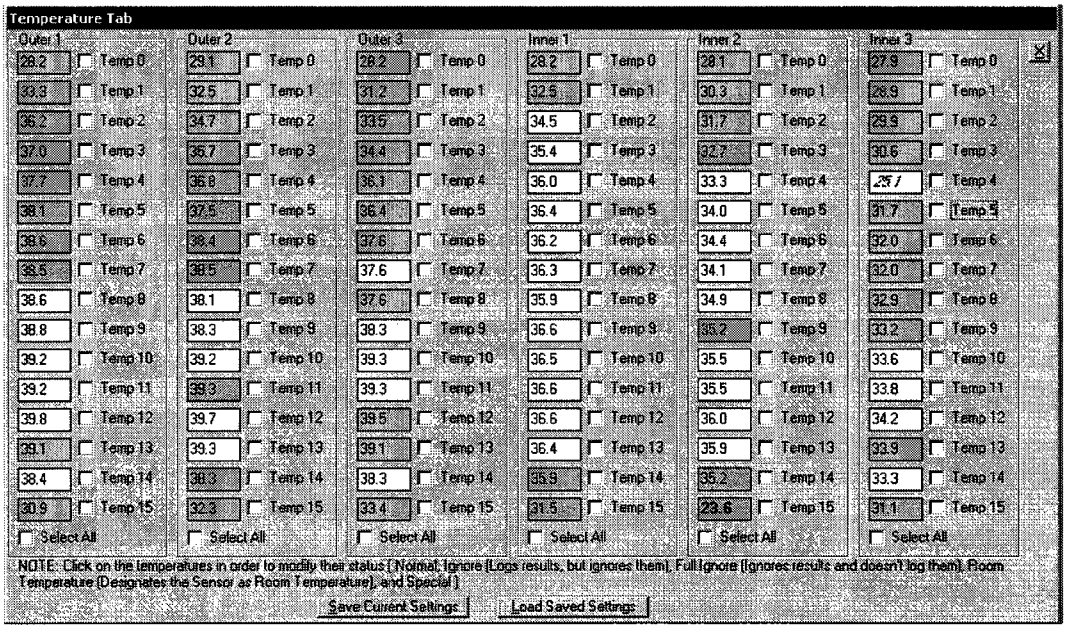

Figure 3 – Temperature tab

The temperature tab seen above displays the temperature readings for all 96 thermocouples. The two different colors are indicators of when the program considers a certain thermocouple has been at roughly the same temperature for an extended period of time, in this case, the color would turn to green, and otherwise it would remain yellow. The setting for how long a "long time" is considered to be, and how much a very small temperature change is, can be modified in the configuration panel. This tab also allows users to select certain thermocouple which they wish to view in the graph tab. The user can also identify which sensors the program should ignore, or which refer to a room temperature, or even a special temperature sensor which the user could designate.

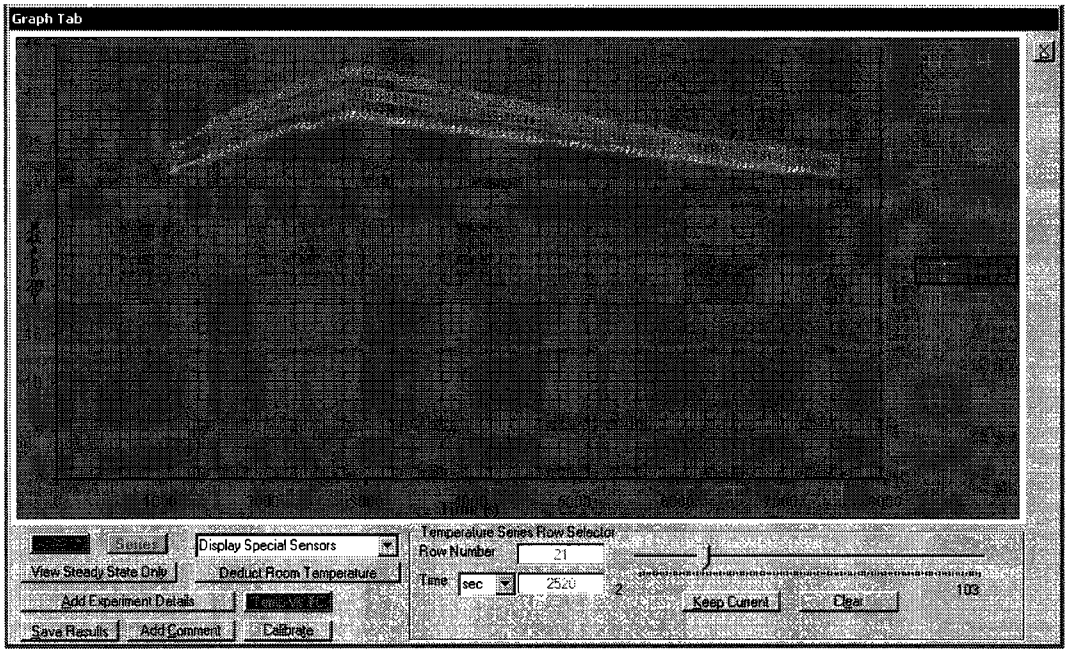

Figure 4 – Graph tab

The graph tab seen above displays graphically the variation of temperature of a single or multiple thermocouples. One could look at the variation of each temperature sensor or a snapshot of all the thermocouples at a fixed time. The user can also choose to only look at steady state results, or even un-calibrated results. There are also shortcuts here which allow

the user to add comments at a certain time, or modify experimental details such as heat flux and eccentricity.

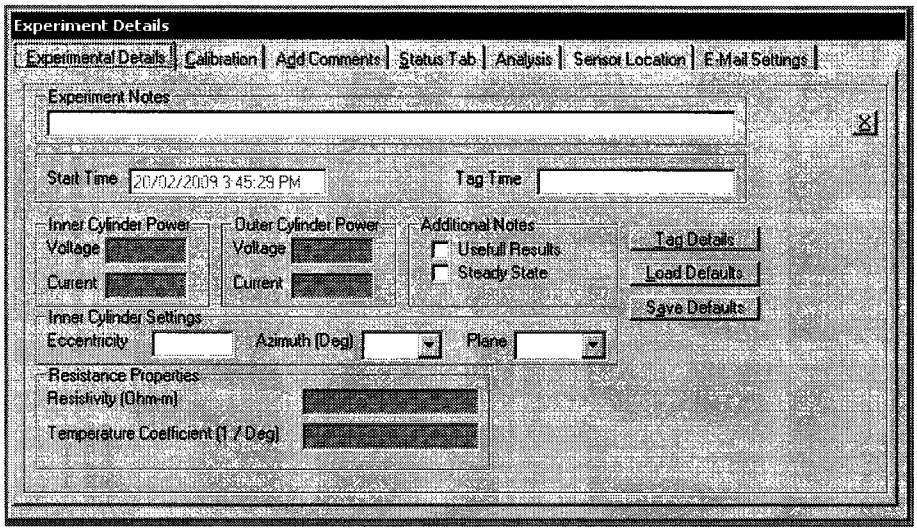

Figure 5 – Experimental Details

The experimental details tab seen above allows the user to add experiment related notes, as well as manually input the voltage and current read from the power supply, input the eccentricity and add other details such as resistivity. Default values can be either loaded automatically or saved in a configuration file for future use.

The calibration tab seen below allows the user to input the temperature at the inlet and at the outlet when the annulus is at room temperature and generate a calibration file which contains offset details for each thermocouple. This technique assumes that the temperature rise in the annulus is linear and equal to that of the stratified room temperature.

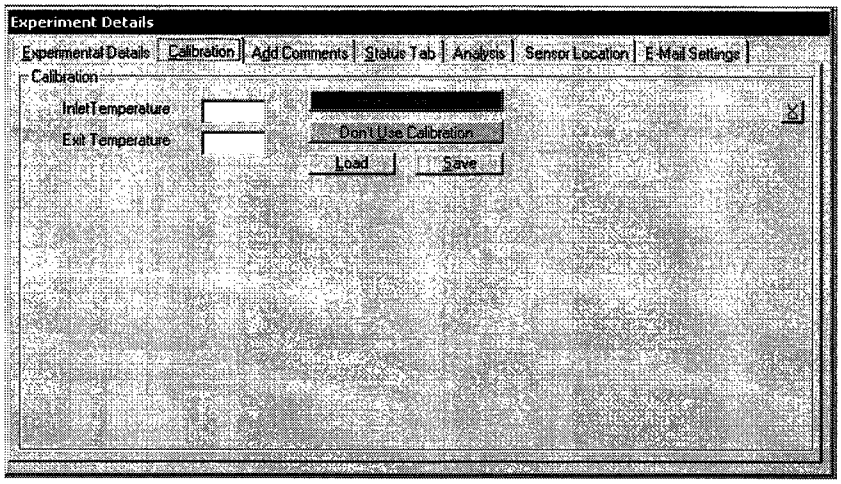

Figure 6 – Calibration Tab

The user can choose to add comments at any time while running the program and the comment will appear next to the results row at the time which the comment was made. This allows the user to add notes about the experiment which might explain certain abnormalities in the results or even things such as a change of eccentricity without stopping the program. The comments tab seen below also allows the user to modify a previous comment or to add a comment at any line in the acquired data set.

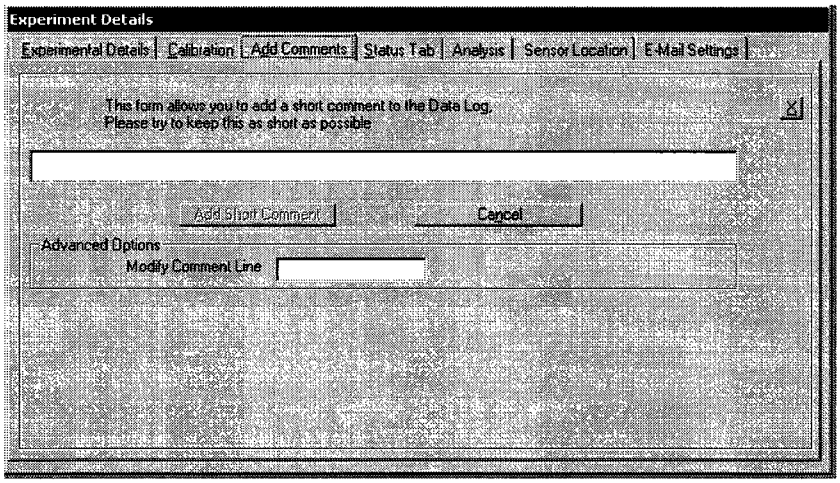

Figure 7 – Comments Tab

The status tab seen below allows the user to monitor the connections to the main module and keep track of any errors which occurred during the program run.

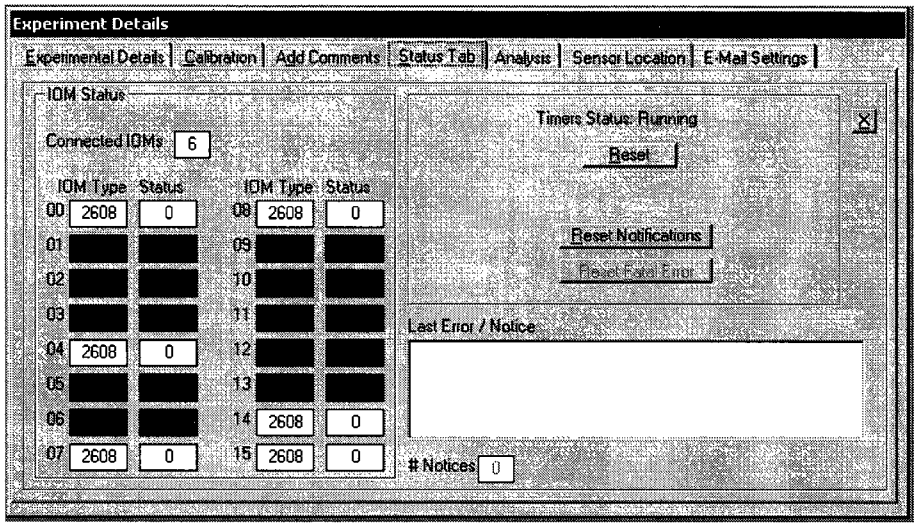

Figure 8 – Status tab

The analysis tab allows the user to take an output file and perform a series of averages and tasks to produce usable graphs and data such as the Nusselt number versus eccentricity or other useful plots.

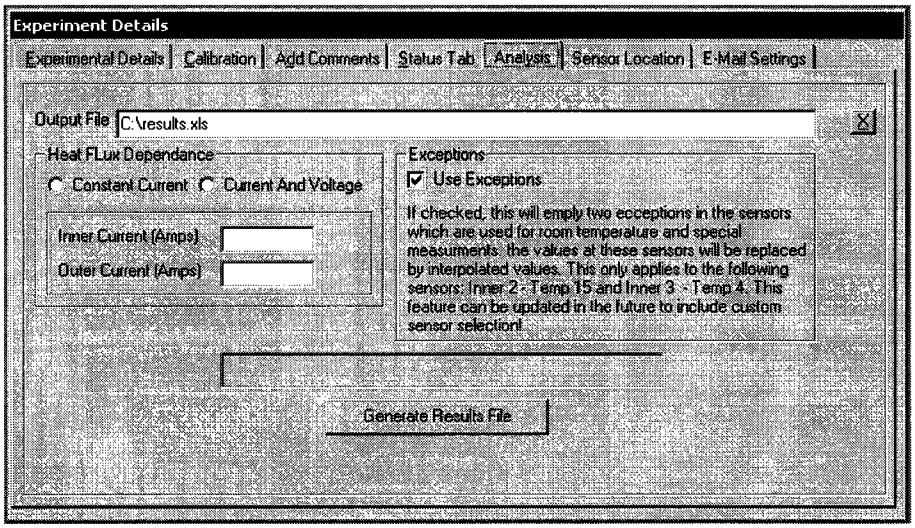

Figure 9 – Analysis tab

The sensor location tab seen below allows the user to assign different sensors to different locations within the annulus. This generally has to be done only once; however, special modifications can be made in case additional modules are required in the future.

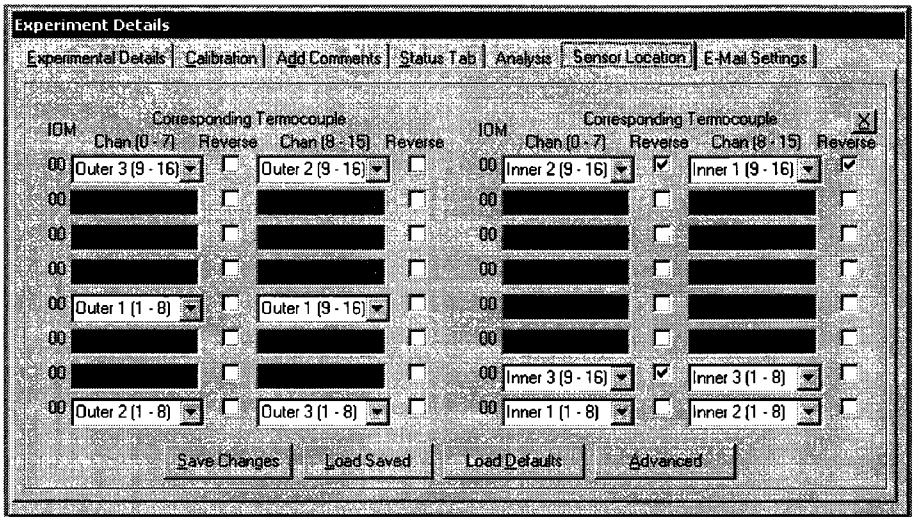

Figure 10 – Sensor location tab

The E-mail Settings tab seen below allows the user to input e-mail information which the program uses to contact the user in the event of an error, or a major event change.

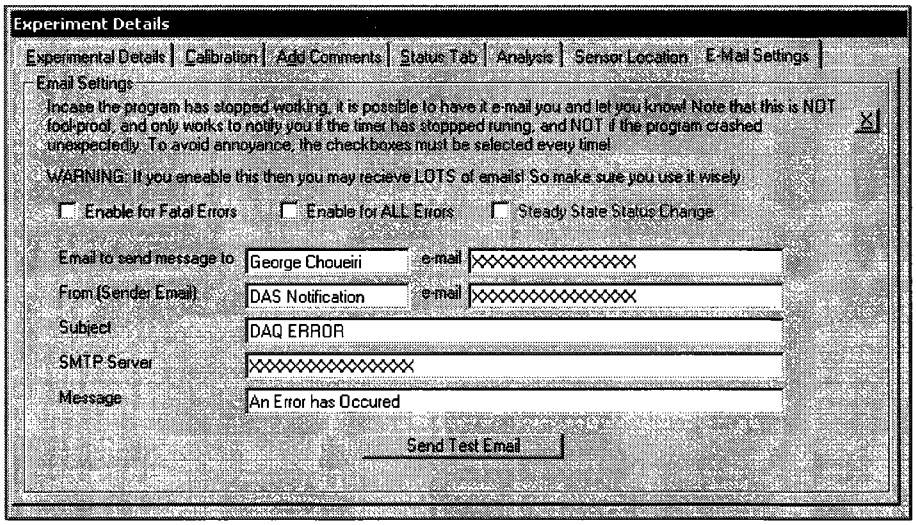

Figure 11 – Error or event e-mail tab